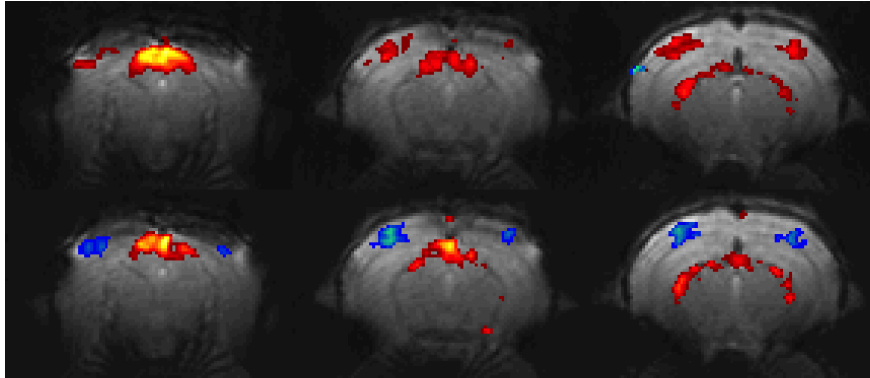




TÉCNICO
LISBOA



Investigation of the mouse visual pathway via high-field functional MRI

Validation and optimization of a novel anaesthetic protocol and development of a visual stimulation setup for functional studies

Francisca Faria Fernandes

Thesis to obtain the Master of Science Degree in

Biomedical Engineering

Supervisor: Dr. Noam Shemesh

Co-Supervisor: Prof. Patrícia Margarida Piedade Figueiredo

Examination Committee

Chairperson: Prof. João Pedro Estrela Rodrigues Conde

Supervisor: Dr. Noam Shemesh

Member of the Committee: Prof. Arlindo Manuel Limede de Oliveira

November 2017

Acknowledgments

At first, I would like to deeply thank my supervisor, Noam Shemesh, for believing in me since day one, for transmitting confidence whenever the stress was taking the best out of me, for his guidance and teaching throughout the whole project and for making me get out of my comfort zone and grow both personally and professionally. Besides giving me the unique opportunity to learn a huge amount of cool stuff related to MRI and improve my skills on those areas, he made my natural thirst for knowledge to grow even more, so I could not feel more blessed or grateful for that. My Master's Degree could not finish in a better possible way.

Right after my supervisor come all of my colleagues from the lab, for always being so helpful, comprehensive and full of fun. This project would have not been possible without their constant support and teaching in each and every step of the way. I also acknowledge all Champalimaud Foundation members that helped me, directly or not, during the last months, especially the Hardware Platform fellows that helped me setting up the visual stimulation system and gave me good advice on 3D modelling.

I would also like to thank my loving mother, Marta Faria, for having the patience to listen me talking about how my project was going in a daily basis and for manifesting true curiosity to also learn about it, and to each one of my family members, for being so supportive and caring even if 970 km lie between us.

Special thanks go to my amazing dear boyfriend, Carlos Martins, for his incessant encouragement words, for his useful advices and for being extremely patient whenever I could not spend much time with him to focus on my projects, and to his family, for always having their door opened and treating me as one of them.

Last, but not least, I would like to thank everyone I met during my student journey, i.e. teachers, professors, colleagues and friends, for contributing to the knowledge I have and to the person I am today.

Abstract

The visual system is highly complex and distributed throughout the brain. Many methods, such as electrophysiological recordings and EEG, have provided immense insight into the visual pathway's underpinnings; however, capturing the entire distributed pathway in rodents – and in particular in the versatile mouse models vis-à-vis transgenesis and optogenetics – would represent a major step forward. Functional MRI (fMRI) can non-invasively investigate the underpinnings of the visual system, but most studies in mice to date relied on presentation of simple flickering stimuli. Moreover, current anaesthesia approaches aimed at avoiding animal motion are ineffective in some strains of mice and incompatible with long scanning times required for delivery of more complex stimuli. Here, we present the development of a visual stimulation system capable of delivering diversely shaped polychromatic stimuli through a 96x64 matrix in the scanner. We further developed a novel anaesthetic protocol based on subcutaneous infusion of etomidate – a sedative allowing much more stable anaesthesia while preserving Blood-Oxygenation-Level-Dependent (BOLD) contrasts – and tested it for the first time in rodent fMRI through three complementary experiments. Significant BOLD responses were recorded along the visual pathway following binocular stimulation. A clear dependence on the frequency and intensity of flashing lights was demonstrated. The suitability of this anaesthetics for future functional studies has been confirmed, and bench tests suggested that significantly smaller doses can be used in the future, thereby providing further experimental stability and flexibility. All these facilitate the study of complex visual stimuli with BOLD fMRI.

Keywords

fMRI, Visual stimulation, Etomidate, Mouse model

Resumo

O sistema visual é altamente complexo e distribuído por todo o cérebro. Muitos métodos, como registros eletrofisiológicos e EEG, forneceram uma visão vasta sobre os fundamentos deste sistema; no entanto, capturar toda a sua distribuição em roedores – em particular nos modelos versáteis de ratinho em relação à transgênese e optogenética – representaria um grande avanço. A ressonância magnética funcional (fMRI) pode investigar de forma não invasiva os fundamentos deste sistema; contudo, a maioria dos estudos em ratinhos até hoje baseou-se na apresentação de estímulos de luz tremeluzente simples. Além disso, as abordagens atuais de anestesia para evitar o movimento animal são ineficazes em algumas estirpes de ratinho e incompatíveis com longos tempos de aquisição necessários para a execução de estímulos mais complexos. Aqui, apresentamos o desenvolvimento de um sistema de estimulação visual capaz de fornecer estímulos policromáticos com diversas formas através de uma matriz 96x64 no scanner. Ainda desenvolvemos um novo protocolo anestésico baseado na infusão subcutânea de etomidato – um sedativo que permite uma anestesia mais estável preservando o contraste BOLD – e testámo-lo pela primeira vez em fMRI de roedores através de três experiências complementares. Foram registadas respostas BOLD significativas ao longo do sistema visual após estimulação binocular e demonstrada uma clara dependência da frequência e intensidade das luzes intermitentes. A aptidão desta anestesia para futuros estudos funcionais foi confirmada, e testes de bancada sugeriram que doses menores podem ser utilizadas no futuro, providenciando maior estabilidade e flexibilidade experimental. Todos estes facilitam o estudo de estímulos visuais complexos em BOLD fMRI.

Palavras Chave

fMRI, Estimulação visual, Etomidato, Modelo de ratinho

Table of Contents

Acknowledgments	iii
Abstract	v
Resumo	vii
Table of Contents	ix
List of Figures	xi
List of Tables	xv
List of Acronyms	xvii
1. Introduction	1
1.1. Motivation	2
1.2. Magnetic Resonance Imaging	3
1.2.1. Magnetic Resonance Physics	3
1.2.1.A. Spins in an External Magnetic Field	4
1.2.1.B. Excitation of a Spin System	5
1.2.1.C. Relaxation of a Spin System and Signal Reception	7
1.2.2. Magnetic Resonance Imaging	8
1.2.2.A. Slice Selection	9
1.2.2.B. Phase and Frequency Encoding	10
1.2.2.C. Contrast Generation and Common Pulse Sequences	11
1.3. Functional Magnetic Resonance Imaging	12
1.3.1. The Blood Oxygenation Level Dependent Contrast	12
1.3.1.A. Neuronal Activity and its Hemodynamic Effects	12
1.3.1.B. The BOLD signal	15
1.3.2. Imaging the BOLD Signal	16
1.3.2.A. Ultrafast Imaging	17
1.3.2.B. Pulse sequence considerations vis-à-vis BOLD	18
1.3.2.C. Spatial and Temporal Resolution	18
1.3.3. Experimental Design	18
1.3.4. Analysis of fMRI data	19
1.3.4.A. Preprocessing	20
1.3.4.B. Postprocessing	21
1.4. Mouse Visual Pathway	23
1.5. Anaesthesia in Rodent fMRI Experiments	27

1.6.	State of the Art of Rodent Visual fMRI.....	29
1.7.	Thesis Outline.....	30
2.	Materials and Methods	33
2.1.	Visual Stimulation fMRI Experiments	34
2.1.1.	Setup for Delivery of Stationary Visual Stimuli	34
2.1.2.	Animal Preparation	35
2.1.3.	MRI Protocol	36
2.1.4.	Visual Stimulation	38
2.1.5.	Data Analysis	39
2.2.	Optimization of Etomidate Dosage	41
2.3.	Setup for Delivery of Complex Visual Stimuli	42
2.3.1.	Equipment.....	42
2.3.2.	Preparation of the setup for monocular visual stimuli delivery	45
3.	Results	47
3.1.	Visual Stimulation fMRI Experiments	48
3.1.1.	Quality control and representative fMRI results	48
3.1.2.	Experiment 1: BOLD responses to different light intensities under etomidate	55
3.1.3.	Experiment 2: BOLD responses to different frequencies under etomidate	59
3.1.4.	Experiment 3: BOLD responses under medetomidine	63
3.2.	Optimization of Etomidate Dosage	65
4.	Discussion.....	67
4.1.	Visual Stimulation fMRI Experiments	68
4.1.1.	Light intensity and frequency tuning under etomidate	70
4.1.2.	Comparison between etomidate and medetomidine	71
4.2.	Optimization of Etomidate Dosage	73
4.3.	Setup for Delivery of Complex Visual Stimuli	74
5.	Conclusions and Future Work.....	75
	References	77
	Annex A	89
	Annex B	91

List of Figures

Figure 1.1 – Spins orientation before and after application of an external magnetic field..	4
Figure 1.2 – Proton’s movement and net magnetization after application of an external magnetic field.	5
Figure 1.3 – Laboratory and rotating frames.	6
Figure 1.4 – Elements of a pulse sequence necessary for image formation.	9
Figure 1.5 – Pulse sequence and the pattern it traverses in k-space.	11
Figure 1.6 – Common pulse sequences used in MRI.	11
Figure 1.7 – The neuron.	13
Figure 1.8 – Ion channels and pumps.	14
Figure 1.9 – Main arteries and veins that allow adequate supply and drainage of blood to and from the brain.	14
Figure 1.10 – Schematic illustration of cortical vasculature.	15
Figure 1.11 – Typical BOLD HRF.	16
Figure 1.12 – A typical EPI pulse sequence and its k-space trajectory.	17
Figure 1.13 – Brain map of significant activation during a fMRI visual task.	23
Figure 1.14 – Schematic of the human and mouse eye.	24
Figure 1.15 – Schematics of the mouse visual system.	25
Figure 1.16 – Schematic of the rodent and human visual geniculate pathways.	26
Figure 2.1 – LED and LED driver employed for accurate delivery of stationary visual stimuli.	34
Figure 2.2 – Visual stimulation setup used for delivery of stationary flickering stimuli inside the scanner.	35
Figure 2.3 – Definition of the position of the slices for the structural and functional scans.	37
Figure 2.4 – Block paradigm used for all fMRI experiments.	38
Figure 2.5 – Brain alignment after coregistration and normalization.	40

Figure 2.6 – Models of HRFs that were tested.	41
Figure 2.7 – Timeline showing the variations in isoflurane (ISO) and etomidate (ETOM) after bolus of etomidate.	42
Figure 2.8 – 3-D models of the bed, resonator, eyes and piece designed for accurate positioning of the OLED display across experiments.	44
Figure 2.9 – Experimental setup for visual pathway mapping in the mouse, with all the elements that are essential for the delivery of complex visual stimuli.	44
Figure 2.10 – Mouse viewing a moving bar stimulus.	45
Figure 3.1 – Raw anatomical images from one representative mouse.	48
Figure 3.2 – Raw functional images (from one frame on a single run) from one representative mouse.	49
Figure 3.3 – Raw signal timecourses in one brain slice before corrections.	50
Figure 3.4 – Idem to Figure 3.3, but for corrected timecourses.	50
Figure 3.5 – Brain maps of significant ($p < 0.02$, minimum cluster size = 8) BOLD activation to binocular visual stimulation with 2 Hz flashing frequency and $8.1 \times 10^{-1} \text{ W/m}^2$ of light intensity in consecutive coronal slices from a single run of a representative mouse, without performing corrections at the slice level and after interpolating some frames of each slices for correction of outliers	51
Figure 3.6 – Uncorrected BOLD signals in the SC, LGN and V1 of a single mouse in response to binocular visual stimulation with 2 Hz flashing frequency and $9.2 \times 10^{-2} \text{ W/m}^2$ of light intensity.	52
Figure 3.7 – Idem to Figure 3.6, only now the plots are averaged over 3 animals ($n = 6$ runs).	53
Figure 3.8 – Brain map of significant ($p < 0.02$, minimum cluster size = 8) BOLD activation to binocular visual stimulation with 2 Hz flashing frequency and $9.2 \times 10^{-2} \text{ W/m}^2$ of light intensity in consecutive coronal slices from a representative mouse ($n = 2$ runs).	54
Figure 3.9 – Brain map of significant ($p < 0.001$, minimum cluster size = 8) BOLD activation to binocular visual stimulation with 2 Hz flashing frequency and $9.2 \times 10^{-2} \text{ W/m}^2$ of light intensity in consecutive coronal slices from an average of 3 mice ($n = 6$ runs).	54
Figure 3.10 – Respiration rate (in respirations per minute) and temperature (in $^{\circ}\text{C}$) plots for all mice used in Experiment 1, from the time that functional acquisition started until the end of the session. ...	55
Figure 3.11 – Brain map of significant ($p < 0.02$, minimum cluster size = 8) BOLD activation to binocular visual stimulation with 2 Hz flashing frequency and $8.1 \times 10^{-1} \text{ W/m}^2$ of light intensity in consecutive coronal slices from the 3 rd mouse used in Experiment 1 ($n = 2$ runs).	56

Figure 3.12 – Average cycle of the BOLD response to binocular visual stimulation with 2 Hz flashing frequency and $8.1 \times 10^{-1} \text{ W/m}^2$ of light intensity in the SC, LGN and V1 of the 3rd mouse used in Experiment 1 (n = 2 runs). 56

Figure 3.13 – Brain maps of significant ($p < 0.001$, minimum cluster size = 8) BOLD activation to binocular visual stimulation with 2 Hz flashing frequency and $9.2 \times 10^{-3} \text{ W/m}^2$, $9.2 \times 10^{-2} \text{ W/m}^2$ or $8.1 \times 10^{-1} \text{ W/m}^2$ of light intensity in consecutive coronal slices from an average of 3 mice (n = 6 runs). 57

Figure 3.14 – Brain maps of significant ($p < 0.001$, minimum cluster size = 8) BOLD activation to binocular visual stimulation with 10 Hz flashing frequency and $9.2 \times 10^{-3} \text{ W/m}^2$, $9.2 \times 10^{-2} \text{ W/m}^2$ or $8.1 \times 10^{-1} \text{ W/m}^2$ of light intensity in consecutive coronal slices from an average of 3 mice (n = 6 runs). 58

Figure 3.15 – Maximum BOLD percent signal change values in the SC, LGN and V1 for flickering stimuli at 2 Hz or 10 Hz and low ($9.2 \times 10^{-3} \text{ W/m}^2$), medium ($9.2 \times 10^{-2} \text{ W/m}^2$) or high ($8.1 \times 10^{-1} \text{ W/m}^2$) intensities. 59

Figure 3.16 – Idem to Figure 3.10, but now for Experiment 2. 60

Figure 3.17 – Brain map of significant ($p < 0.02$, minimum cluster size = 8) BOLD activation to binocular visual stimulation with 2 Hz flashing frequency in consecutive coronal slices from one single run of the 2nd mouse used in Experiment 2. 60

Figure 3.18 – Average cycle of the BOLD response to binocular visual stimulation with 2 Hz flashing frequency in the SC, LGN and V1 of the 2nd mouse used in Experiment 2 (n = 2 runs). 61

Figure 3.19 – Brain map of significant ($p < 0.001$, minimum cluster size = 8) BOLD activation to binocular visual stimulation with 2 Hz flashing frequency in consecutive coronal slices from an average of 3 mice (n = 6 runs). 61

Figure 3.20 – Brain map of significant ($p < 0.001$, minimum cluster size = 8) BOLD activation to binocular visual stimulation with 5 Hz flashing frequency in consecutive coronal slices from an average of 3 mice (n = 6 runs). 62

Figure 3.21 – Brain map of significant ($p < 0.001$, minimum cluster size = 8) BOLD activation to binocular visual stimulation with 10 Hz flashing frequency in consecutive coronal slices from an average of 3 mice (n = 6 runs). 62

Figure 3.22 – Brain map of significant ($p < 0.001$, minimum cluster size = 8) BOLD activation to binocular visual stimulation with 20 Hz flashing frequency in consecutive coronal slices from an average of 3 mice (n = 6 runs). 62

Figure 3.23 – Maximum BOLD percent signal change values in the SC, LGN and V1 for flickering stimuli at 2 Hz, 5 Hz, 10 Hz or 20 Hz. 63

Figure 3.24 – Respiration rate (in respirations per minute) and temperature (in °C) plots for all mice used in Experiment 3, from the time that functional acquisition started until the moment the animal started to move. 64

Figure 3.25 – Brain map of significant ($p < 0.001$, minimum cluster size = 8) BOLD activation to binocular visual stimulation with 2 Hz flashing frequency in consecutive coronal slices from an average of 3 mice ($n = 6$ runs) anaesthetized with medetomidine..... 64

Figure 3.26 – Cycle of the BOLD response to binocular visual stimulation with 2 Hz flashing frequency in the SC, LGN and V1 of mice anaesthetized with medetomidine and etomidate..... 65

Figure B.1 – Spherical coordinates of the FOV of the flat screen..... 91

List of Tables

Table 3.1 – Age, weight and physiological parameters, indicated as mean \pm standard deviation, of mice that were subjected to one of the 3 different anaesthetic regimes. The values for the respiration rate and the temperature were averaged from the recordings obtained from the complete discontinuation of isoflurane until the end of the experiment. The symbol † indicates death.	66
Table A.1 – Parameters of the 9 double-gamma functions that were tested and the time instants in which they and their convolution with the paradigm peaked.....	89

List of Acronyms

2-D	Two-dimensional
3-D	Three-dimensional
ATP	Adenosine triphosphate
BOLD	Blood-Oxygenation-Level-Dependent
Ca²⁺	Calcium ion
CBF	Cerebral blood flow
CBV	Cerebral blood volume
Cl⁻	Chloride ion
CMRO₂	Cerebral metabolic rate for oxygen
DAQ	Data acquisition
dHb	Deoxygenated hemoglobin
EPI	Echo-planar imaging
FISP	Fast Imaging with Steady state Precession
FLASH	Fast Low Angle Shot
fMRI	Functional magnetic resonance imaging
FOV	Field of view
FWHM	Full width at half maximum
GE	Gradient-echo
GLM	General linear model
HASTE	Half-Fourier Acquisition Single-shot Turbo Spin Echo
Hb	Oxygenated hemoglobin
HRF	Hemodynamic response function
K⁺	Potassium ion
LED	Light emitting diode

LGN	Lateral geniculate nucleus
MR	Magnetic resonance
MRI	Magnetic resonance imaging
Na⁺	Sodium ion
OLED	Organic light emitting diode
pCO₂	Partial pressure of carbon dioxide
pO₂	Partial pressure of oxygen
RARE	Rapid Acquisition with Relaxation Enhancement
RF	Radiofrequency
RGC	Retinal ganglion cell
ROI	Region of interest
SC	Superior colliculus
SE	Spin-echo
SNR	Signal-to-noise ratio
SPEN	Spatiotemporal encoding
SPI	Serial peripheral interface
SPM	Statistical Parametric Mapping
TE	Echo time
TR	Repetition time
TTL	Transistor-transistor logic
V1	Primary visual cortex
V2	Secondary visual cortex

1

Introduction

The present chapter introduces the theme of this dissertation over a motivational and contextual perspective. It outlines the purpose of the project and provides the reader with the theoretical background required for its full comprehension.

1.1. Motivation

Many animals, and humans, rely on vision as their dominant sense to evaluate their surroundings and guide their behaviour. Understanding how the brain gives rise to the experience of sight has been the focus of much attention over the years, especially in Neuroscience, but also in many biomedical studies. Many efforts have been made to understand how the visual system converts light to neuronal signals, perceives depth, distinguishes different frequencies, colours, orientations or directions of movement, recognizes objects and faces, and adapts following injury [1].

Although mice have a lower visual acuity than humans, and they rely more on tactile, olfactory and auditory information to ensure its survival [2], the mouse visual system is becoming a predominant model for investigating disease mechanisms and experience-dependent plasticity in the visual pathway [3]. The strongest motivation for using mice is their extremely useful genetic flexibility, which enables unique experimental settings such as optogenetic control of specific neurons or models of disease [4].

The visual pathway is widespread in the brain. Most studies on the mouse visual system were conducted with invasive and small field of view (FOV) measurement techniques such as electrophysiological recordings [5][6][7] and two-photon microscopy [8][9]. However, a complementary approach involves methods capable of capturing activity along the entire pathway. Magnetic resonance imaging (MRI) presents a useful modality for identifying and investigating responsive brain regions involved in distributed networks with high spatial resolution and extensive brain coverage. In particular, functional magnetic resonance imaging (fMRI) based on the Blood-Oxygenation-Level-Dependent (BOLD) contrast provides information on response dynamics following stimulation [10]. Its non-invasive nature also makes it optimal for longitudinal experiments. In monkeys and humans, fMRI has been vastly employed to study the underpinnings of the visual system [11][12][13][14][15]; however, in rodents, visual stimuli are scarcely used in the context of fMRI, and setups for visual presentation are nearly always limited to simple flickering stimuli [16][17]. In mice, in particular, this might represent a missed opportunity, as the mouse's predominance in transgenic animal models could be used to investigate functional abnormalities associated with genetic models of human diseases [18] or to investigate functional consequences of activating specific cell populations via optogenetics [19].

Therefore, the need arises to develop a system that would enable more complex visual tasks and a sensitive investigation of the entire visual pathway of the mouse using fMRI.

A related issue with the paucity of mouse fMRI experiments is the proper choice of the anaesthetic regime. Anaesthetics commonly used for fMRI in mice, such as isoflurane and medetomidine, have been shown to have some drawbacks. Particularly, it was observed that isoflurane decreases cerebrovascular reserve capacity at doses required to maintain anaesthesia, which affects the neurovascular coupling on which the BOLD contrast relies. On the other hand, the action of medetomidine proved ineffective in numerous mouse lines, which represents a shortcoming in view of

the growing number of transgenic mouse models [20]. Additionally, the sedative effects of medetomidine often do not last for more than 1-2 hours, after which animal motion typically occurs. More complex fMRI experiments that require longer scanning periods are thus compromised.

To overcome the shortcomings of these agents, a novel anaesthesia regime for small animal imaging based on intravenous infusion of etomidate has been proposed and tested [20]. Etomidate provided long-term stable physiological conditions, preserved neurovascular coupling and afforded full recovery from anaesthesia in spontaneously breathing animals, lending itself as the anaesthetic of choice for longitudinal fMRI studies across a wide variety of mouse models. However, this protocol requires intravenous administration, which carries risks of fluid overload and pulmonary edema [21]. Although a protocol for its subcutaneous delivery has already been reported [22], which is simpler and has less probability of complications, its applicability for fMRI on the mouse remains to be verified. Finally, BOLD fMRI under etomidate sedation has only been carried out so far upon electrical stimulation of the hindpaw and etomidate's usefulness in visual system fMRI remains unexplored.

1.2. Magnetic Resonance Imaging

Magnetic resonance imaging is a non-invasive imaging technique with capability for high spatial resolution and excellent and varied soft-tissue contrast, which makes it highly versatile for the study of disorders and function [23]. Moreover, it allows one to obtain images in any plane through the body. It does not make use of ionising radiation and therefore does not induce any damage to tissues. The following subsections describe in a detailed manner the basic principles of magnetic resonance (MR) signal generation and image formation.

1.2.1. Magnetic Resonance Physics

A nucleus capable of exhibiting nuclear magnetic resonance effects, commonly referred to as a spin, has both an angular momentum J and a magnetic moment μ , which are respectively defined by:

$$|J| = \frac{h}{2\pi} \sqrt{I(I+1)} \quad (1.1)$$

and

$$\mu = \gamma J \quad (1.2)$$

where h is the Planck constant and I and γ are the spin quantum number and the gyromagnetic ratio of the nucleus, respectively. An odd number of protons or neutrons is required for a nonzero nuclear magnetic moment [24]. Due to their prevalence in water molecules, hydrogen nuclei (single protons) are extremely abundant in biological tissues and, consequently, the most commonly used nuclei in MRI [23]. Since the value of I for protons is 1/2, one can calculate from (1.1) and (1.2) the magnitude of the proton magnetic moment:

$$|\mu| = \gamma \frac{h}{4\pi} \sqrt{3} \quad (1.3)$$

1.2.1.A. Spins in an External Magnetic Field

The net magnetization \mathbf{M} is defined as the vector sum of all magnetic moments of all spins within a spin system. In the absence of an external magnetic field, spins are randomly oriented and tend to cancel each other out, resulting in a null net magnetization, as shown in Figure 1.1. However, when a proton is positioned in an external static magnetic field \mathbf{B}_0 (conventionally aligned along the z-axis), the z-component of the magnetic moment is restricted to take one of two possible values:

$$\mu_z = \pm \frac{\gamma h}{4\pi} \quad (1.4)$$

Thus, the axes of spin of the protons can assume two possible different orientations, i.e. partially aligned with (parallel) or against (antiparallel) the magnetic field, corresponding to two different energy states, as one can see in Figure 1.1. The interaction energy of a magnetic moment with \mathbf{B}_0 is defined by:

$$E = -\boldsymbol{\mu} \cdot \mathbf{B}_0 = -\mu_z B_0 \quad (1.5)$$

where B_0 is the strength of the magnetic field. Therefore, the corresponding energy levels for the proton are obtained by combination of (1.4) and (1.5):

$$E = \mp \frac{\gamma h B_0}{4\pi} \quad (1.6)$$

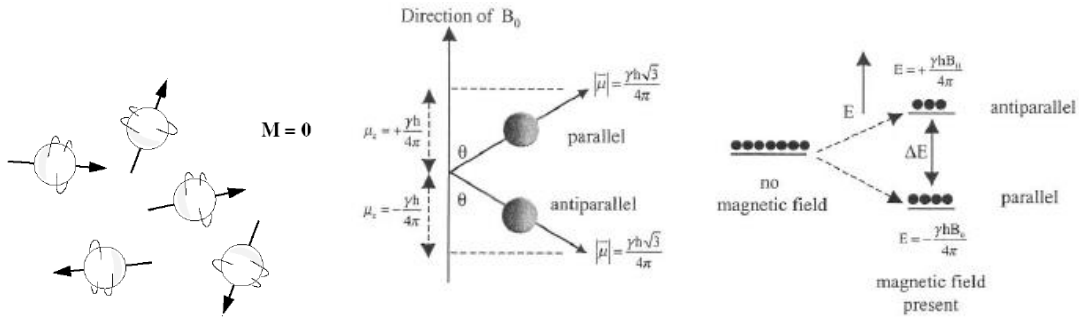


Figure 1.1 – Spins orientation before and after application of an external magnetic field. (Left) Protons with random axes of rotation in the absence of a magnetic field. (Middle) Protons' axes of spin aligned along (parallel) or against (antiparallel) the magnetic field, with $\theta=54.7^\circ$. (Right) Zeeman splitting after application of an external magnetic field, resulting in two energy levels (extracted from [23]).

The torque exerted by the external magnetic field as it tends to align the spins with \mathbf{B}_0 induces changes in the magnetic moment of that spin over time given by:

$$\frac{d\boldsymbol{\mu}}{dt} = \gamma(\boldsymbol{\mu} \times \mathbf{B}_0) \quad (1.7)$$

Therefore, instead of completely aligning with the magnetic field, the protons experience a precession movement around the direction of the magnetic field, as shown in Figure 1.2, with a characteristic angular frequency, known as the Larmor frequency:

$$\boldsymbol{\omega}_L = \gamma \mathbf{B}_0 \quad (1.8)$$

Protons in the parallel state have lower energy and are consequently more stable than protons in the antiparallel state. Statistically, there will be more protons in the lower energy state than protons in the higher energy state, according to the Boltzmann distribution, and the difference between states will depend on temperature and B_0 amplitude [23]. This net excess of protons aligned with the main magnetic field produces an initial net magnetization M_0 along B_0 that provides the basis for MR signal generation, defined by:

$$M_0 = \frac{\Delta E}{2k_B T} n \mu_z z \quad (1.9)$$

where ΔE is the energy difference between the two energy states:

$$\Delta E = \frac{\gamma h B_0}{2\pi} \quad (1.10)$$

k_B is the Boltzmann coefficient, T is the temperature in degrees Kelvin, and n is the number of protons per unit volume. Since this initial net magnetization is fully aligned with z-axis, the longitudinal component M_z of the magnetization is said to be equal to M_0 . The spins' magnetic moment orientation inside the plane orthogonal to B_0 remains random, making the transverse magnetization M_{xy} , i.e. the transverse component of M that is perpendicular to B_0 , equal to zero, as shown in Figure 1.2.

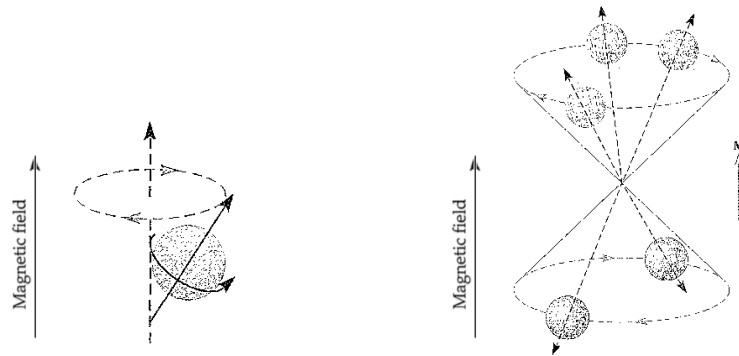


Figure 1.2 – Proton's movement and net magnetization after application of an external magnetic field. (Left) Precession movement of a proton. In addition to the spinning motion, the axis of spin wobbles around the field axis, also known as precession axis. (Right) The net magnetization of all spins in the presence of an external magnetic field only has a longitudinal component due to the net excess of protons in the parallel state (extracted from [24]).

1.2.1.B. Excitation of a Spin System

The previous description describes the thermal equilibrium state. However, magnetic resonance remains unobservable without a perturbation. To generate observable signals, M must be rotated from the z axis towards the xy plane such that a transverse component of magnetization M_{xy} is created. Thus, transitions must be induced between the protons in the parallel and the antiparallel energy levels by providing energy to the spin system in the form of a radiofrequency (RF) pulse, also termed as B_1 field, defined by:

$$B_1 = B_1 x \cos \omega_{rf} t - B_1 y \sin \omega_{rf} t \quad (1.11)$$

where B_1 is the magnitude of \mathbf{B}_1 , t is time and ω_{rf} is the irradiation frequency. This oscillating electromagnetic field consists of an electromagnetic wave adjusted to oscillate at a specific frequency $\nu_{rf} = \omega_{rf}/2\pi$, which is determined by the energy difference between the two energy levels of the nucleus of interest, as given by the Bohr relation:

$$\Delta E = h\nu_{rf} \quad (1.12)$$

The combination of (1.10) with (1.12) provides the resonant frequency condition for the nucleus of interest. The Larmor frequency thus governs not only the frequency at which spins precess, but also describes the resonance condition with which energy can be emitted or absorbed by the system.

When \mathbf{B}_1 is applied, the net magnetization is tipped towards the axis of the radiofrequency pulse according to:

$$\frac{d\mathbf{M}}{dt} = \gamma(\mathbf{M} \times \mathbf{B}) \quad (1.13)$$

where \mathbf{B} corresponds to the summation of both \mathbf{B}_0 and \mathbf{B}_1 . The net magnetization will therefore describe a spiral movement called nutation that combines the rotation from the longitudinal axis to the transverse plane with the precession around the longitudinal axis at the Larmor frequency, as shown in Figure 1.3.

Since both the spins and the excitation pulse rotate at the Larmor frequency, one can adopt a rotating reference coordinate system that is also rotating at that frequency to describe the spin trajectories more easily. The unit vectors in the rotating transverse plane are represented by x' and y' (Figure 1.3). Within this frame, the spins and the RF pulse become stationary and the net magnetization will simply rotate around \mathbf{B}_1 during excitation with an angular velocity equal to:

$$\omega_1 = \gamma B_1 \quad (1.14)$$

The angle formed between the longitudinal axis and the net magnetization vector following excitation is called the flip angle and depends on the duration T of the pulse:

$$\alpha = \gamma B_1 T \quad (1.15)$$

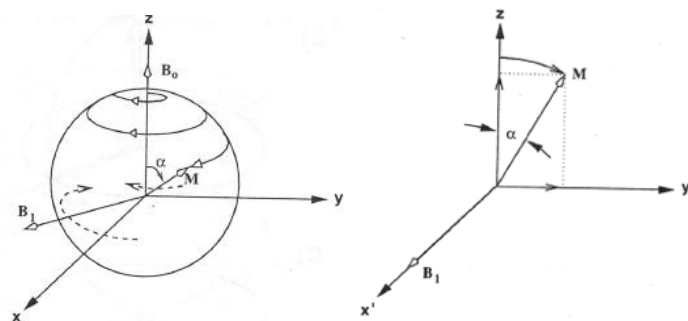


Figure 1.3 – Laboratory and rotating frames. (Left) Global magnetization describing a nutation movement, i.e. moving on the surface of a sphere with radius M_0 , during excitation in the laboratory frame. (Right) Tipping motion of the net magnetization during excitation in the rotating frame (extracted from [25]).

1.2.1.C. Relaxation of a Spin System and Signal Reception

After the application of the RF pulse, the spin system is perturbed from equilibrium and will tend to come back towards the initial conditions by releasing the absorbed electromagnetic energy through processes collectively called relaxation. Spin relaxation occurs in two different ways: by longitudinal relaxation (or spin-lattice relaxation) and by transverse relaxation (or spin-spin relaxation). In turn, the timescales governing relaxation constrain the time during which MR signals can be acquired following a single excitation pulse [24].

Longitudinal relaxation, also called T_1 recovery, occurs when spins in the high-energy state go back to their low-energy state by transferring energy to the surrounding lattice (the main magnetic field in this case), allowing the recovery of the longitudinal component of the net magnetization. This comes with a reduction in the transverse magnetization and therefore a smaller MR signal. The longitudinal recovery is described by the time constant T_1 , which is typically on the order of a few hundreds of milliseconds to a few seconds *in vivo* at high field. The magnitude of the longitudinal component of magnetization following a pulse with a flip angle of α can be described as:

$$M_z(t) = M_0 \cos \alpha + (M_0 - M_0 \cos \alpha) \left(1 - e^{-\frac{t}{T_1}}\right) \quad (1.16)$$

After the application of an ideal 90° pulse, the net magnetization has been fully tipped into the transverse plane and no longitudinal magnetization remains immediately after the pulse, suggesting that each energy state contains identical spin populations, and also that M_{xy} spins are coherent, thus producing a measurable MR signal. However, with time, spin-spin interactions induce an irreversible dephasing. Therefore, the transverse component of magnetization exponentially decreases over time. This process is called transverse relaxation or T_2 decay and is characterized by the time constant T_2 . The magnitude of the transverse magnetization can be described as:

$$M_{xy}(t) = M_0 \sin \alpha e^{-\frac{t}{T_2}} \quad (1.17)$$

A different source of transverse magnetization loss arises due to spatial inhomogeneities in the magnetic field. Due to the field inhomogeneity, spins evolve with a slightly different frequency. By contrast with T_2 relaxation, this type of coherence loss can be reversed using specialized pulse sequences. The combined effect of spin-spin-interactions and magnetic field inhomogeneities is described by another time constant, T_2^* , which is always lower than T_2 and is typically in the order of a few milliseconds at high fields in biological systems. Under idealized conditions, $\frac{1}{T_2^*} = \frac{1}{T_2} + \gamma \Delta B_0$ where ΔB_0 represents the field inhomogeneity.

The T_1 , T_2 and T_2^* values depend on magnetic field strength and can be measured for any type of substance. Since they determine the amplitude of the recovered signal for each type of tissue, different image contrasts can be obtained if appropriate imaging parameters are chosen [23].

In summary, the MR phenomena can be described by the Bloch equation [24]:

$$\frac{d\mathbf{M}}{dt} = \gamma \mathbf{M} \times \mathbf{B} + \frac{1}{T_1} (\mathbf{M}_0 - \mathbf{M}_z) - \frac{1}{T_2} (\mathbf{M}_x + \mathbf{M}_y) \quad (1.18)$$

which explains the combined effect of the magnetic fields and the relaxation of the spins on the net magnetization and provides the theoretical basis for all MRI experiments. If this equation is solved to determine the MR signal at each point in time following excitation, one can conclude that the longitudinal and transverse components of magnetization will recover and decay, respectively, according to:

$$M_z(t) = M_0 + (M_{z0} - M_0)e^{-\frac{t}{T_1}} \quad (1.19)$$

and

$$M_{xy}(t) = M_{xy0}e^{-\frac{t}{T_2}}e^{-i\omega t} \quad (1.20)$$

where M_{z0} and M_{xy0} represent the magnitude of the longitudinal and transverse magnetization at time zero, respectively, and $e^{-i\omega t}$ is the accumulated phase over time t , being the angular frequency ω dependent on the total magnetic field experienced by the system.

Changes in the transverse magnetization of a spin system can be measured through a receiver coil. The precession of the net magnetization at the Larmor frequency causes the density of magnetic flux experienced by the RF detector coil to also change over time, which in turn induces an electromotive force in the coil that can be measured. Since this electromotive force oscillates at the Larmor frequency, the receiver coil must also be tuned to that frequency. The signal obtained by the receiver coil is then demodulated, amplified, and Fourier transformed giving origin to an MR spectrum. Therefore, the MR signal at a given time point is given by the spatial summation of the transverse magnetizations of all three-dimensional volume elements (also called voxels) within the excited sample, as given by the following equation:

$$S(t) = \int_x \int_y \int_z M_{xy}(x, y, z, t) dx dy dz \quad (1.21)$$

1.2.2. Magnetic Resonance Imaging

In 1973, Paul Lauterbur understood that the magnetic resonance phenomenon could be harnessed towards generating images through the use of magnetic field gradients [26]. Lauterbur found that the superimposition of a second spatially-varying magnetic field would make atomic nuclei located at different positions to precess at different frequencies. Therefore, by dividing the MR signal into components with different frequencies, images that provide spatial information can be generated.

To unambiguously encode spatial information in all three dimensions, three types of gradient coils are required. Since the static magnetic field is always directed along the longitudinal axis (or z-axis), the magnetic field gradients along the x, y and z directions only linearly change the strength of the magnetic field along the relevant axis, but not its direction, according to:

$$B(\tau) = B_0 + G_x(\tau)x + G_y(\tau)y + G_z(\tau)z \quad (1.22)$$

where $G_x(\tau)$, $G_y(\tau)$ and $G_z(\tau)$ represent the gradient fields along each direction at the time point τ . Combining (1.20) with (1.21) and substituting the ω term in (1.20) by the individual angular frequencies generated by each magnetic field component described in (1.22) results in the MR signal equation:

$$S(t) = \int_x \int_y \int_z M_{xy0}(x, y, z) e^{-\frac{t}{T_2}} e^{-i\omega_L t} e^{-i\gamma \int_0^t (G_x(\tau)x + G_y(\tau)y + G_z(\tau)z) d\tau} dx dy dz \quad (1.23)$$

Because the activation of the three gradient fields at the same time does not allow to resolve spatial information in all three directions, the process of image formation requires a sequence of gradients and RF pulses applied at a specific order and at specific instants of time, as it is shown in Figure 1.4.

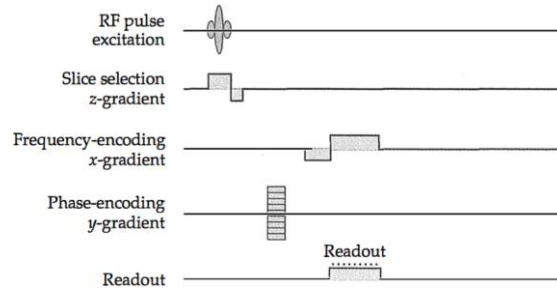


Figure 1.4 – Elements of a pulse sequence necessary for image formation (extracted from [24]).

1.2.2.A. Slice Selection

Although direct three-dimensional imaging is possible, most MRI experiments obtain two-dimensional slices to then join them into three-dimensional images, also called volumes. In such 2-D MRI experiments, the signal should be localized in a two-dimensional slice, which is accomplished using a gradient along the z-direction simultaneously with a shaped RF pulse that contains a band of frequencies whose spectrum matches those of nuclei within the desired slice. This ensures that only those spins are on resonance with the pulse and will absorb energy, change state and contribute to the MR signal. The thickness T of the slice depends not only in strength of the slice selecting gradient but also on the frequency bandwidth $\Delta\omega_S$ of the RF pulse:

$$T = \frac{\Delta\omega_S}{\gamma G_z} \quad (1.24)$$

Since the net magnetization stops depending on z after this step, (1.23) can be further reduced to two dimensions as:

$$S(t) = \int_x \int_y M(x, y) e^{-\frac{t}{T_2}} e^{-i\omega_L t} e^{-i\gamma \int_0^t (G_x(\tau)x + G_y(\tau)y) d\tau} dx dy \quad (1.25)$$

being $M(x, y)$ the integral of $M_{xy0}(x, y, z)$ over slice thickness.

Because the spins accumulate different phases depending on their position within the slice after the pulse has been applied, a rephasing z-gradient is then applied to counteract this loss of phase coherence and make the spins within that slice to have the same phase. Moreover, since it is almost impossible to have a perfect rectangular slice profile and there might be bleeding of excitation from one slice to another, an interleaved slice acquisition is usually used in order to avoid slices pre-excitation and the saturation of the MR signal.

1.2.2.B. Phase and Frequency Encoding

Once the excitation pulse has been applied and the relaxation phenomena have started, the application of other spatially-encoding gradients within the chosen slice must start in order to detect the MR signal before it has completely decayed. In many cases, a phase-encoding gradient is initially applied for a constant period so that spins within the slice can accumulate differential phase offsets along one direction (by convention, the y-direction). Once a spatially dependent phase shift has been established, a frequency-encoding gradient in the orthogonal direction (by convention, the x-direction) is imposed to change the frequency of the spins during data acquisition (DAQ). In order to simplify the understanding of how the MR signal is converted into the final image, the k-space scheme is usually adopted. If one considers the following two variables

$$k_x(t) = \frac{\gamma}{2\pi} \int_0^t G_x(\tau) d\tau \quad (1.26)$$

$$k_y(t) = \frac{\gamma}{2\pi} \int_0^t G_y(\tau) d\tau \quad (1.27)$$

Equation (1.25) can be expressed as

$$S(t) = \int_x \int_y M(x, y) e^{-\frac{t}{T_2}} e^{-i\omega_L t} e^{-i2\pi k_x(t)x} e^{-i2\pi k_y(t)y} dx dy \quad (1.28)$$

From this, one can verify that the k-space and the image space form simple two-dimensional (2-D) Fourier transform pairs, and that the MR signal can be represented by a 2-D function in a coordinate system with axes k_x and k_y and units in the spatial frequency. Decreasing the separation between adjacent k-space points increases the FOV of the image and increasing the extent of k-space increases the resolution of the image.

One can fill the k-space from the maximum negative values of k_x and k_y to their maximum positive values by varying the strength of the y-gradient in each excitation to select each different line of the k-space and by applying a small negative dephasing x-gradient followed by a long positive x-gradient, as shown in Figure 1.5. Thus, the resolution along the phase-encoding direction determines the total time needed to collect the entire image.

Once the k-space is filled, an inverse 2-D Fourier transform can be performed to convert k-space data into the spatial domain to produce an image.

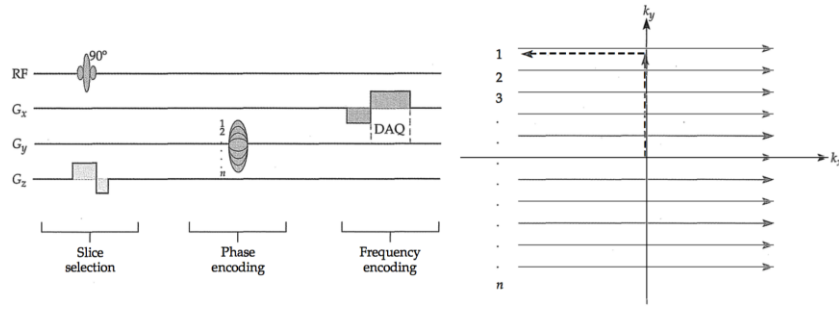


Figure 1.5 – Pulse sequence and the pattern it traverses in k-space. Vertical motion in k-space is determined by the strength of G_y , while the application of G_x causes leftward and then rightward motion in k-space (extracted from [24]).

1.2.2.C. Contrast Generation and Common Pulse Sequences

There are two factors that govern the time at which MR images are collected: the repetition time (TR), which is the time between successive excitations, and the echo time (TE), that is the time between the first RF pulse and MR signal readout. By varying these data acquisition parameters, differential contrast between soft tissues can be introduced.

One of two primary types of pulse sequences used in MRI is the spin-echo (SE) sequence, whose scheme is presented in Figure 1.6. This type of sequence starts with a 90° pulse and allows true spin-spin relaxation that does not depend on field inhomogeneities through an additional 180° refocusing pulse (together with a new slice selection gradient) that flips the precession direction at TE/2 and reverses loss of phase coherence. The magnitude of the signal detected at TE will therefore be governed by the T_2 rather than the T_2^* values of tissues.

On the other hand, gradient-echo (GE) pulse sequences only use gradients to refocus the signal and create an echo, as shown in Figure 1.6. On the contrary to spin-echo sequences, these sequences are sensitive to magnetic field inhomogeneities and are therefore prone to susceptibility artefacts, i.e. signal losses caused by field inhomogeneities, e.g. near air-tissue interfaces. To decrease the time necessary for full longitudinal recovery and allow faster acquisition rates, the flip angle α is usually reduced to a value smaller than 90° . For a given TR, one should choose the Ernst angle, which is calculated from:

$$\alpha_{Ernst} = \cos^{-1} e^{-TR/T_1} \quad (1.29)$$

so that the signal-to-noise ratio (SNR) is maximized while keeping TR relatively short.

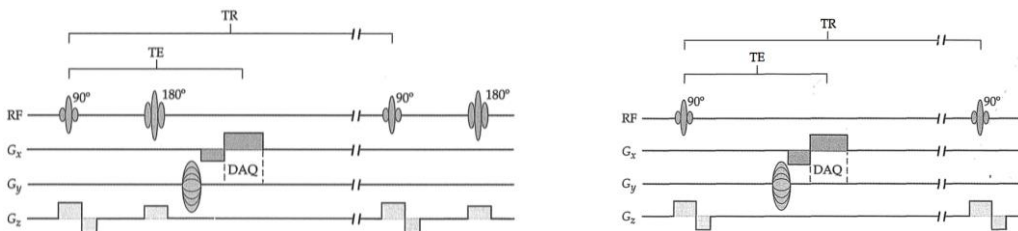


Figure 1.6 – Common pulse sequences used in MRI. (Left) Spin-echo sequence. (Right) Gradient-echo sequence (adapted from [24]).

1.3. Functional Magnetic Resonance Imaging

Functional magnetic resonance imaging (fMRI) is one of MRI's most important methodologies, which allows the investigation of brain function through contrasting physiological changes that are correlated with neural activity. Most fMRI studies rely on the Blood-Oxygenation-Level-Dependent contrast, i.e. on changes in blood oxygenation levels in response to the metabolic requirements of active neurons. These hemodynamic changes report on underlying neuronal activity, and provide insight into how different brain regions are involved in different perceptual, motor or cognitive tasks. This section provides information on how neuronal activity relates to hemodynamic activity and how to image these hemodynamic variations. Considerations about fMRI experimental design and data analysis are also given.

1.3.1. The Blood Oxygenation Level Dependent Contrast

Already in 1936, Pauling and Coryell found that oxygenated haemoglobin (Hb) is diamagnetic – it has no unpaired electrons and a zero magnetic moment – and that deoxygenated haemoglobin (dHb) is paramagnetic as it has both unpaired electrons and a significant magnetic moment [27]. Paramagnetic dHb molecules thus distort the surrounding magnetic field; nearby spins will experience varying field strengths and will precess at different frequencies, resulting in a shorter T_2^* [28]. Ogawa and his colleagues hypothesized in the late 1980s that changes in the proportion of blood oxygen would affect the visibility of blood vessels on T_2^* -weighted images. They observed that pulse sequences sensitive to T_2^* evidenced a decreased MR signal where blood was highly deoxygenated due to the magnetic susceptibility effects of dHb, while oxygenated blood had little or no effect [10][29]. This discovery formed the basis of the BOLD contrast as a measure of brain function. They speculated that this contrast could be used to identify areas of increased brain activity through two nonexclusive mechanisms. First, neuronal activity would increase the consumption of oxygen, increasing the amount of dHb given a constant blood flow. Alternatively, increased blood flow in the absence of increased metabolic requirements might decrease the amount of dHb. This speculation proved to be correct but the mechanism behind the BOLD signal proved, with time, to be much more complex [30][31] and is still not completely understood.

1.3.1.A. Neuronal Activity and its Hemodynamic Effects

Neurons are the basic information-processing units of the central nervous system, performing both integrative and signalling activities that are important for sensory, motor and cognitive processes. Neurons collect information from other neurons through connections via dendrites and cell bodies, and transmit the outcomes of integrative activity to other neurons through specialized junctions, called synapses, where axon terminal processes are located adjacent to the postsynaptic membrane of the dendrite or soma of another neuron, as depicted in Figure 1.7.

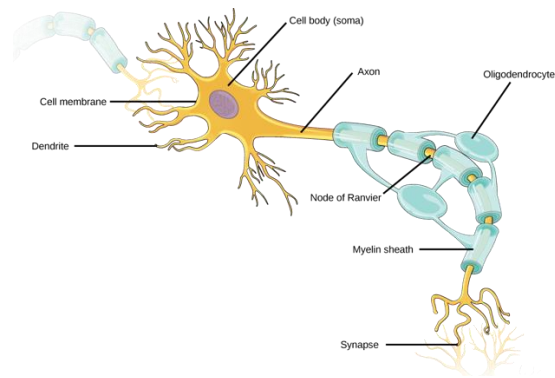


Figure 1.7 – The neuron (extracted from [32]).

Due to the continuous control on the influx and efflux of chemical substances performed by ion channels and pumps present on the neuron lipid bilayer (Figure 1.8), neurons at rest have a greater concentration of potassium ions (K^+) in the intracellular space, while sodium (Na^+), calcium (Ca^{2+}) and chloride (Cl^-) ions have higher concentration in the extracellular space. The ensuing resting electrical potential is about -40 to -70 mV. If the presynaptic process of an axon releases neurotransmitters, i.e. chemicals that travel across the synaptic cleft to interact with receptors on the postsynaptic membrane, transient changes in the permeability of the postsynaptic membrane can occur through the opening of normally blocked ion channels, causing a decrease (depolarization) or increase (hyperpolarization) on the membrane's electrical potential, depending on the ion's polarity. If the net depolarization experienced by a neuron decreases below a certain voltage threshold, many voltage-gated Na^+ channels will open, causing an influx of Na^+ into the cell that will propagate down the axon and therefore trigger an action potential. When this wave of depolarization reaches the end of the axon, voltage-gate Ca^{2+} channels are opened, allowing Ca^{2+} influx into the presynaptic terminal, in turn promoting the release of fresh neurotransmitters into the synaptic cleft. Following depolarization, a K^+ efflux causes the restoration of the membrane potential. While neither of these integrative and signalling activities requires external sources of energy because the translocation of ions occurs along their concentration gradients, the process of restoring both the unequal distribution of ions across the membrane and the resting membrane potential and establish equilibrium by the ion pumps demands consumption of energy.

Adenosine triphosphate (ATP) constitutes the main energy currency for most cells in the body and can be efficiently generated from glucose through aerobic glycolysis, as long as enough oxygen is present. Although this energy is then used to support many aspects of brain physiology, the primary energy expenditure of the brain supports the restoration of membrane potentials following integrative and signalling activities [33][34]. Because the brain has little energy storage capacity, a continuous supply of glucose and oxygen are required to meet the brain's metabolic demands. This is accomplished by the vascular system through increased blood flow to active neurons.

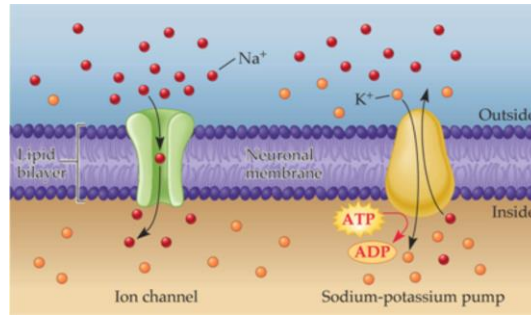


Figure 1.8 – Ion channels and pumps. Ion channels may be gated by specific molecules or by voltage differences across the membrane and allow ions to diffuse along their concentration gradient, while ion pumps require energy to move ions against their concentration gradient across membranes (extracted from [24]).

Despite that the human brain is only ~2% of its weight, about 15 to 20% of the blood flow in the entire human body is directed to the brain. This supply comes through two major arterial systems: the internal carotid arteries, which enter the skull through the foramen lacerum, and the vertebral arteries, that ascend in the anterior surface of the spinal cord and enter the brain through the foramen magnum, fusing then together into the single basilar artery. The basilar artery and the internal carotid arteries interconnect to form the circle of Willis, which then divides into the anterior, middle, and posterior cerebral arteries, as shown in Figure 1.9. Each of these arteries supplies a different region of the brain. Brain’s venous drainage is accomplished through the jugular veins that exit the skull base through the jugular foramen.

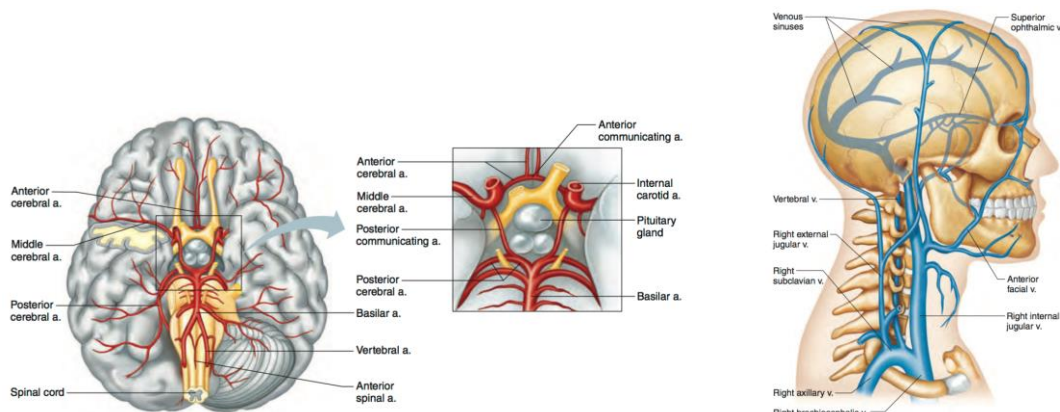


Figure 1.9 – Main arteries and veins that allow adequate supply and drainage of blood to and from the brain. (Left) Major arteries that supply the brain, viewed from the inferior surface of the brain (a. stands for artery). (Right) Major veins that drain blood from the brain (extracted from [35]).

The cerebral cortex is supplied with blood through meningeal arteries that traverse the cortical surface, as illustrated in Figure 1.10. Conducting arteries in the cerebral cortex branch into many shorter and smaller distributing arteries, which continue to ramify on the cortical surface into precortical arterioles. Each precortical artery then branches into smaller arterioles that enter the cortical layers perpendicularly to the cortical surface. The density of vascularization is not uniform across cortical layers, and is higher where cell density is greatest. Therefore, the deep white matter

beneath the grey matter layers has the lowest vascular density. After the diffusion of oxygen and glucose at the capillaries level, the blood is drained from the cortex via the ascending and pial veins.

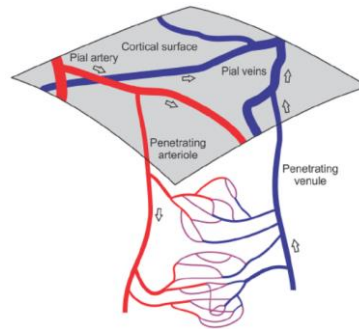


Figure 1.10 – Schematic illustration of cortical vasculature (extracted from [36]).

Neural activity promotes changes in blood flow by modulating the volume of blood vessels and the velocity with which blood moves through them. Active neurons release vasoactive substance that dilate and increase the diameter of the arterioles that supply them, reducing the vessels' resistance and increasing flow. However, this local change is not sufficient by itself for blood flow regulation. Small arterioles on the pial surface that may be distant from the active neurons have high resistance and oppose flow. These resistance vessels convert the pulsatile ejection of blood from the heart into a steady flow through the capillaries, being also an important component in the control of blood flow through the capillary bed.

While the epicentre of the blood flow is in the region of increased activity, arteriolar dilation and increased blood flow are also observed distantly from this region, where there is no neural activity. This imposes some limitations on the spatial specificity of hemodynamic changes as an indicator of neural activity and therefore on BOLD fMRI, because the neural activity produces hemodynamic changes over an area that is larger than the area of synaptic activity.

1.3.1.B. The BOLD signal

Current evidence suggests that the neural activity that is most closely related to changes in the BOLD signal is the local field potential, which corresponds to the total electrical activity in a small region around the recording site, rather than the spiking output of individual cells [31][37]. BOLD fMRI tracks changes in the total amount of dHb in each voxel over time, and dHb is present in capillaries and veins but absent in fully oxygenated arterial blood. Even though dHb decreases the MR signal through shortening of T_2^* , MR signal increases are detected during neural activation. This is explained by a superfluous perfusion of oxygenated blood to active regions, aiming to exceed the metabolic needs. This excess of oxygenated blood displaces the dHb from the capillaries supporting the active neurons and from the downstream venules, resulting in a decrease in the MR signal loss due to T_2^* effects and in a brighter MR image [24].

Therefore, the BOLD signal reflects not only changes in the cerebral metabolic rate for oxygen (CMRO₂), but also changes in cerebral blood flow (CBF) and cerebral blood volume (CBV) following

neuronal activity through neurovascular coupling [30]. The BOLD hemodynamic response function (HRF) corresponds to the change in MR signal on T_2^* images triggered by local neuronal activity and is described by a series of phases, as it is shown in Figure 1.11. It is considered to be the impulse response of the black box that converts neural activation to a BOLD response [38].

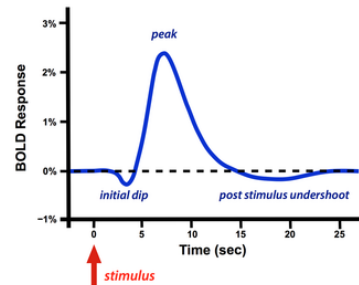


Figure 1.11 – Typical BOLD HRF (extracted from [39]).

At first, the HRF may demonstrate a small initial dip immediately after the stimulus, which may result from an initial metabolic extraction of blood oxygen that increases the amount of dHb locally before the later overcompensatory response. Thereafter, an inflow of oxygenated blood due to the increased metabolic demands of neurons decreases the amount of dHb within the voxel and increases the BOLD signal to a maximum value, known as peak. If the neural activity is long lasting, the signal might decrease somewhat from the peak and stabilize into a plateau. Finally, once the neural activity ceases, the MR signal starts to decrease to a level below the baseline for an extended interval because, according to the balloon model introduced by Buxton and colleagues, CBF decreases more rapidly than CBV, increasing locally the amount of dHb [40]. This effect is known as post-stimulus undershoot and finishes when the blood volume has completely returned to normal levels. Another hypothesis by Lu, van Zijl and colleagues suggests that a sustained metabolic demand might also be an important contributor to the post-stimulus undershoot [41].

Although it is important to understand the properties of the HRF to a single isolated stimulus, in most fMRI experiments multiple stimuli are presented in succession. Therefore, it is important to consider how the hemodynamic response behaves in these situations. If it was considered to be linear, two stimuli separated by a short interval of time would produce a response mathematically equivalent to the sum of the two individual HRFs. However, the BOLD response has been shown to suffer from refractory effects, revealing responses to the second and following stimuli that are reduced in amplitude and increased in latency in comparison with the response to a single stimulus, suggesting that a linear model will overestimate the response to closely spaced stimuli and decrease the effectiveness of the analyses [42]. Thus, one should account for nonlinearities when analysing fMRI data.

1.3.2. Imaging the BOLD Signal

Changes in blood oxygenation levels in response to metabolic requirements of active neurons resolve over periods of a few seconds to a few tens of seconds. Therefore, unlike anatomical images of the

brain in which contrast and spatial resolution are more important than the speed of acquisition, functional studies require high temporal resolution to measure changes in brain function, i.e., at similar rate as the physiological changes of interest [24].

1.3.2.A. Ultrafast Imaging

One of the fastest types of MRI pulse sequences employs a single-shot traversal of k-space. Perhaps the most common single-shot technique is echo-planar imaging (EPI), proposed by Mansfield in 1977 [43]. In EPI, rapidly alternating frequency-encoding gradients are applied over the period of data acquisition with short phase-encoding bursts during transitions, allowing to sample the k-space in a back-and-forth pattern as depicted in Figure 1.12.

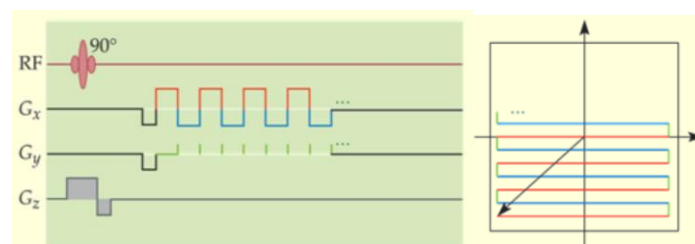


Figure 1.12 – A typical EPI pulse sequence and its k-space trajectory. Gradient changes are highlighted in different colours for easy comparison between the pulse sequence and the k-space (extracted from [24]).

Because the whole image must be acquired following a single excitation pulse, the k-space must be filled before significant T_2^* (in GE sequences) or T_2 (in SE sequences) decays can occur. However, a relatively large k-space usually needs to be sampled to achieve reasonable spatial resolution, which requires gradients with fast rise times. The rapid switching pattern of the gradients that characterizes EPI sequences taxes the gradient system heavily and is prone to artefacts in the low bandwidth dimension.

In particular, GE-EPI is highly sensitive to field inhomogeneities that cause marked signal losses and image distortions. This is particularly apparent in the mouse brain, due to the low volume/surface area ratio [44]. These inhomogeneities can be compensated through shimming coils that optimize magnet homogeneity; however, it becomes more difficult to adequately shim the field at higher magnetic fields.

Spiral imaging sequences use sinusoidal variations in the gradients to describe a spiral trajectory in the k-space thereby reducing gradient hardware demands and making use of more efficient encoding. However, these sequences require an additional step of interpolation because the reconstruction process needs the data points to follow a Cartesian grid [24].

There are multiple other ultrafast sequences that can be used to image the BOLD signal and counteract some EPI disadvantages, such as Spatiotemporal Encoding (SPEN) imaging, Half-Fourier Acquisition Single-shot Turbo Spin Echo (HASTE) or Fast Imaging with Steady state Precession (FISP), but a detailed description of those is beyond the scope of this thesis.

1.3.2.B. Pulse sequence considerations vis-à-vis BOLD

Two important factors that should be considered when choosing a pulse sequence for imaging BOLD are the sensitivity to dHb variations in vessels surrounding firing neurons and the spatial specificity of the acquired signal. Gradient-echo acquisitions are widely used in fMRI experiments due to their sensitivity to T_2^* contrast. However, GE BOLD signals can be influenced by hemodynamic changes in large draining vessels distant from the active neurons, thereby compromising specificity [45].

SE sequences can eliminate the BOLD signal arising from extravascular compartments of large vessels and retain sensitivity to the intravascular and small-vessel extravascular BOLD signal, accentuating microvascular contributions and minimizing signal fluctuations due to physiological processes [46]. They improve the spatial specificity of the BOLD contrast at the cost of a reduced BOLD sensitivity and therefore a smaller signal.

1.3.2.C. Spatial and Temporal Resolution

The spatial and temporal resolution of an fMRI study are crucial both in terms of the underlying activity and sensitivity/specificity trade-offs. Smaller voxel sizes may intuitively seem better for fMRI studies, since it would be easier to distinguish the boundaries between proximal functional areas; however, (1) SNR will suffer due to the proportionality between the active volume and signal intensity; (2) acquisition time may be severely increased; (3) smaller voxels will have smaller susceptibility distribution, thereby making BOLD amplitude paradoxically smaller. On the other hand, larger voxels may suffer from partial volume effects. The temporal resolution in fMRI is limited by the TR and by the vascular system itself, which varies slowly even if the duration of neural activity is very short. Therefore, although a decrease in TR might improve estimates of vascular changes, the use of very short TRs requires smaller flip angles (Ernst angles) leading to a smaller MR signal. Moreover, short TRs also reduce the number of slices one can acquire per TR. One way to improve temporal resolution and avoid these problems is to use interleaved stimulus presentation, which consists of presenting the experimental stimuli at different points within a TR during different trials, increasing the effective sampling rate at the expense of fewer trials per condition and less precision of the estimated HRF.

1.3.3. Experimental Design

Designing an efficient fMRI experiment is of extreme importance, given the extensive resources it requires in acquiring and analysing the data. It starts with an experimental question that is derived into a research hypothesis that makes predictions about the results of a certain manipulation and must be falsifiable. This research hypothesis is then tested through an experiment that manipulates one or more independent variables and assigns different conditions to them, measures the effects of this manipulation on the dependent variables, and evaluates those measurements using statistical tests. The conditions that are assigned to an independent variable can be of two types: an experimental condition or a control condition. While an experimental condition, also known as task condition, contains the stimulus or task of interest, the control condition provides a baseline to which the task

conditions can be compared. When defining these conditions, it is important that they only differ in one property. This way, any change in the outcome of each manipulation can be attributed with confidence to the change in that specific property. If this does not happen, confounding factors arise, i.e., variables that unintentionally co-vary with the independent variable. Minimizing confounding factors by ensuring that they vary randomly with the independent variable is thus crucial.

Most fMRI studies use either blocked or event-related designs [24]. Blocked designs alternate between conditions using different time blocks. Then, the magnitude of the BOLD responses in each block condition is compared. This type of design is useful when the process of interest does not evoke a measurable BOLD response if presented over short intervals. Since it usually provides maximal BOLD amplitude changes between conditions, this type of design is very powerful in terms of detection of voxels with significant fMRI activation. However, blocked designs are relatively insensitive to the shape of the HRF since the response in each block contains contributions from multiple HRFs in time, which gives them a low estimation power of the time course of activation in active voxels.

If the different conditions one desires to test cannot be separated into different blocks, then the choice of an event-related design might be appropriate. In this type of design, short-duration stimuli are presented in random order and with varying interstimulus interval. This gives a higher flexibility than most blocked designs, since the same events can then be analysed in different ways according to the experiment goals. Since event-related designs allow to determine the shape of the HRF for each condition and then compare for example the amplitude or the timing between conditions, they have a strong estimation power. However, because each event only evokes small changes in BOLD signal and usually there are less events to average than in blocked designs, their detection power is weak.

1.3.4. Analysis of fMRI data

One important quantity for fMRI studies is the ratio between the intensity of the task-related BOLD signal and the variability in the data due to noise, also defined as functional SNR. fMRI data have a noisy nature. The signal of interest is usually less (and sometimes much less) than 2 or 3% of the total intensity of the MR signal. In addition, task-related changes in the BOLD signal are very small when compared to other sources of spatial and temporal variability in the data.

The use of a stronger magnetic field also has many effects in the quality of fMRI data. As field strength increases, the small-vessel extravascular component of the BOLD response increases faster than the large-vessel extravascular component, and there is a reduction in the intravascular contribution from large vessels to the signal, which increases the spatial specificity of the BOLD response and its functional SNR. As a consequence, the spatial extent of activation may also increase. However, higher fields entail also increased susceptibility artefacts.

The main causes of temporal and spatial noise in fMRI are the following [24]:

- thermal motion of the electrons within the sample and scanner hardware that causes random fluctuations in the MR signal;

- system noise due to imperfections in the scanner hardware, causing, among others, scanner drift. Scanner drift is detected by slow changes in voxels intensity over time due to variations in the strength of the magnetic field over the course of the scanning session;
- head motion, respiration, heart rate that can be temporally correlated with the experimental manipulation;
- non-task-related brain processes or changes in the cognitive strategy, which are not so critical in anesthetized rodent fMRI.

Therefore, it is important to reduce the variability in the data that is unrelated to the experimental task before proceeding with its statistical analysis.

1.3.4.A. Preprocessing

A set of corrective algorithms are typically applied to raw fMRI data before analysis. A consensus about the best pipeline for fMRI preprocessing has not been reached, but some procedures are very commonly used [38], including slice-timing correction due to slight differences on slice acquisition times, head motion correction, alignment to a reference brain through coregistration and normalization, spatial smoothing and temporal filtering.

Quality Control. One of the most important steps consists of examining and visualizing all data during any stage of fMRI experimentation through time-series movies and plots. This allows detection of artefactual signals, e.g. due to radiofrequency leakage, severe motion, or other artefacts, and elimination of these aberrant data from the analysis.

Slice-timing Correction. Variability in the BOLD responses due to acquiring different slices at different times within one TR can be corrected through slice-timing correction [38], either during preprocessing by temporal interpolation of the data points from all slices to a reference slice, or during task-related statistical analysis where a flexible model of the HRF is used [47]. The most common types of interpolation used are linear, spline and sinc, the last two typically most suitable for noise-related variability [48][49].

Head motion correction. Head movements, even if small, can severely corrupt fMRI data and generate meaningless activation values, especially at the borders of the brain where differences in intensity between neighbouring voxels are large. Small head motion can be corrected through rigid body registration describing motion by six parameters: three for translation and three for rotation in each of the three Cartesian axes. Generally, one chooses a reference volume, and the rigid body transformation that minimizes a certain cost function (usually the sum of squared differences) between the BOLD responses of each volume and the chosen reference is calculated. As a rule of thumb, slice-timing correction should be performed before head motion correction if the slices were acquired in an interleaved fashion and after if they were acquired in an ascending fashion [38].

Coregistration and Normalization. To help identify the anatomical location of a task-related activation that is discovered during data analysis and to allow intersubject comparisons, two more steps are usually followed [38]. First, functional images are aligned to higher-resolution anatomical

images through coregistration. However, since voxel sizes and contrasts are often different in the functional and anatomical scans, the most popular coregistration algorithms use a cost function based on the mutual information between the histogram bins of the voxels in the two types of images. The structural images of the brain are then warped to match the shape, size and orientation of a standard reference brain through normalization. This is usually accomplished through an affine transformation that has 12 degrees of freedom and a nonlinear transformation [38].

Spatial Smoothing. Once the functional images have been aligned to the same space, a spatial smoothing of the data with a Gaussian kernel is typically performed, to reduce high-frequency spatial noise and improve SNR at a cost of spatial resolution. By the central limit theorem, this will make the distribution of the BOLD responses more normal, improving the validity of some statistical testing which assumes normally distributed noise. Furthermore, it allows Gaussian random field theory to be used as a solution to the multiple comparisons problem [38].

Temporal Filtering. Finally, a high pass temporal filter can be applied to reduce the effects of slow fluctuations in the local magnetic field properties of the scanner and improve functional SNR.

1.3.4.B. Postprocessing

Most fMRI analyses are based on significance testing. Experiments are designed to discriminate between an experimental hypothesis with some prediction about the data and a null hypothesis that the experimental manipulation will have no effect on the experimental data. One of the most popular statistical tests used to evaluate the validity of the null hypothesis and identify brain regions that reflect underlying neuronal activity is the general linear model (GLM).

GLM is a regression model that assumes that the observed data results from a linear combination of different regressors with a variable weighting, along with uncorrelated Gaussian noise [38]. Therefore, it can be reduced to the following formula:

$$Y = X\beta + \varepsilon \quad (1.30)$$

where Y is the observed data, X is the design matrix that contains a set of regressors that try to explain the variability in the data, β is the set of weights and ε is the error term whose variance is a measure of the total unexplained variability. This method tries to find the set of weights that minimize the least-squares error and evaluates the statistical significance of a regressor by comparing the amount of variability it explains with the amount of variability explained by the error term. Therefore, regressors that explain much of the variance of the data will have high weights, while regressors that explain little of the signal will have near zero weights.

A basic correlation analysis is equivalent to a model with only one regressor, the predicted BOLD response. However, there are other factors unrelated to the experimental hypothesis that may affect the fMRI signal, also known as nuisance regressors, which should be included in the design matrix to reduce the amount of residual variation included in the error term, increase the significance of the results and improve the validity of the GLM. The most common used nuisance regressors are the six motion parameters calculated during realignment of the volumes to a reference volume, which

describe the accumulated movement along each direction or axis [50]. A baseline activation term is also often added to the model to remove mean signal change for each run. Since BOLD responses can be affected by respiration and heart rate, these data, if acquired, can also be included in the design matrix. It should be noted, however, that the addition of columns to the design matrix decreases the number of degrees of freedom and consequently reduces the significance of the results. It is also important to verify that regressors are as orthogonal to each other as possible, so that the GLM validity is maximized.

The prediction of the BOLD response in activated voxels starts with the assumption that neural activity in neurons that process the stimulus can be modelled by a boxcar function. Then, assuming the linearity and time-invariance of the hemodynamic response, a model of the HRF is chosen and convolved with the boxcar to generate the predicted BOLD response. The most popular choice for the HRF is to select a specific mathematical function with some free parameters, which can be for example a gamma function [51], a difference of two gamma functions that accounts for the initial peak and post-stimulus undershoot of the HRF [52], or a weighted linear combination of basis functions that improves the flexibility of the design matrix [47]. This approach has its weaknesses, however, since the function chosen may not be a particularly accurate model of the HRF. Studies have shown that the HRF varies across brain regions, subjects, stimuli, scanning sessions, age and type of anaesthetic used, which may limit the interpretability of fMRI studies [53][54][55][56].

Once the parameters of the model have been estimated, the research hypothesis can be tested. This is done through the use of contrast vector \mathbf{c} that hypothesizes the weight of the regressors. The simplest type of contrast evaluates whether a single regressor causes significant variations in the BOLD signal. Assuming that the error terms are all uncorrelated and have variance equal to σ_ε^2 , the parameter weights are multiplied by the contrast weights and the resulting quantity is scaled by its standard deviation, leading to the following statistic:

$$t = \frac{\mathbf{c}'\boldsymbol{\beta}}{\sqrt{\sigma_\varepsilon^2 \mathbf{c}'(X'X)^{-1}\mathbf{c}}} \quad (1.31)$$

that is then evaluated, usually with a t -test, against the null hypothesis of zero [38]. This t -statistic is computed for every voxel, allowing the creation of a map with the t -values for each voxel. Each t -statistic can be converted to a probability value based on the degrees of freedom of the data set. If the probability that the results could occur under the null hypothesis is lower than a chosen p -value threshold, the result is considered to be statistically significant. Moreover, since it is expected that all areas of activation extend over a certain number of voxels and it is unlikely that a group of contiguous voxels will all appear active by chance, one can increase the conservatism of the test and decrease the likelihood of false positive results by only considering clusters of voxels as significant. A statistical parametric map that shows the areas of the brain with statistically significant activation can then be generated, as exemplified in Figure 1.13.

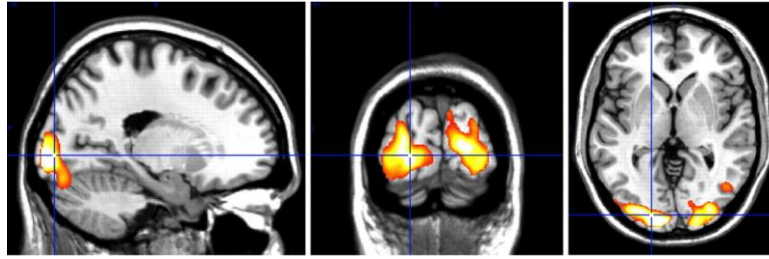


Figure 1.13 – Brain map of significant activation during a fMRI visual task (extracted from [57]).

The GLM approach can be combined with region of interest (ROI) analyses to overcome the problem of using the same HRF and therefore the same design matrix throughout the brain [24]. These analyses evaluate hypotheses about the functional properties of particular brain regions that are usually chosen based on anatomical criteria. Although they might prevent the identification of functionally distinct subregions and consequently cause a loss in spatial specificity, they may increase the ability to detect changes in the region as a whole.

The combination of data from many subjects to test an experimental hypothesis can also greatly increase the experimental power. The two main approaches for accomplishing multi-subject measurements are the fixed-effects analysis and the random-effects analysis [24]. While the former assumes that differences between subjects are caused by random noise and combines the data from all subjects into a single analysis, the latter accounts for differences on the effects of the experimental manipulation across subjects, allowing to make inferences about the population from which the subjects were drawn.

1.4. Mouse Visual Pathway

The neural circuitry of the visual system is one of the most complex of all sensory systems. The process of vision starts in the eye, whose structure differs slightly between humans and mice, as depicted in Figure 1.14. The anterior part of the eye contains a refracting lens system responsible for light focusing, while the posterior part of the eye contains a photoreceptive surface that translates light into nerve signals [35][58][59]. It is composed of two main chambers: the anterior chamber between the cornea and the iris, and the posterior chamber between the iris and the vitreous humor that contains the lens. Both of these chambers are filled with aqueous humor, a fluid produced by the ciliary body that nourishes the cornea and lens and maintains the shape of the front of the eye [35][60].

The eye must be able to compensate for changes from light to dark and from near to far. Light-dark adaptation requires dilatation or contraction of the pupil, the central opening of the iris. Near-far adaptation is achieved by changes in the curvature of the lens (accommodation), in the lines of sight (convergence) and in pupillary width [58]. When the eye is adjusted for long distances (negative accommodation), the surface of the lens is only slightly curved since the ciliary muscle fibres are relaxed, the lines of sight run parallel and the pupils are dilated. On the contrary, when the eye has to accommodate to short distances (positive accommodation), the lens thickens due to the contraction of

the ciliary muscle fibres, the lines of sight cross each other where the fixated object stands, and the pupils constrict.

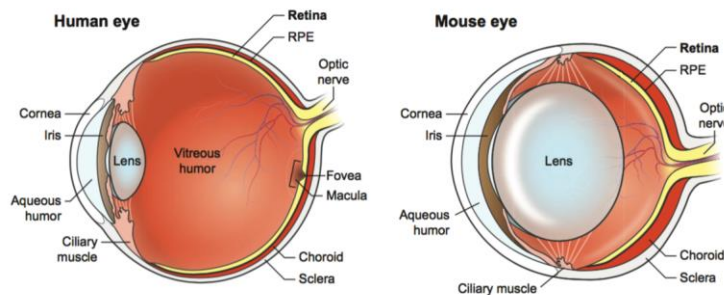


Figure 1.14 – Schematic of the human and mouse eye (adapted from [61]).

There are three main layers that surround the eye: a fibrous layer that includes the cornea and the sclera; a vascular layer composed of the ciliary body, the iris and the choroid, a membrane that contains many blood vessels that nourish the retina; and an internal sensory layer, the retina [58][60].

The retina is an extremely complex relay system. Light impulses that reach the eye already undergo processing at the retina level [58]. It consists of an outer pigmented layer and an inner neural layer. The latter comprises three different main layers of cells: the neuroepithelial layer that contains photoreceptors, a medial retinal layer that contains bipolar, horizontal and amacrine cells, and the ganglion cell layer [58][59][60].

The photoreceptors are light-sensitive cells and represent the first neuron of the visual pathway. They can be one of two types: rods or cones. The rod cells are responsible for light-dark perception, while the cone cells are responsible for color vision and visual acuity. These cells contain light-sensitive pigments that break down when they absorb light energy.

The mouse retina is dominated by rods, which make it specialized for vision under low light conditions [62]. The visual pigment of rod cells is the rhodopsin. The absorption of light by rhodopsin causes variations in its molecular structure, causing it to break down into its protein and pigment components.

Whereas there is only one type of rod in the vertebrate retina, there are usually multiple types of cones that can express one or more pigments. Cones account for approximately 3% of all mouse photoreceptors and can express one or a combination of two pigments: one that absorbs light of short wavelengths (peak sensitivity of 360 nm, which corresponds to UV light) and another that is sensitive to light of medium wavelengths (peak sensitivity between 508 and 512 nm, which corresponds to green light) [63][64][65]. This means that mice lack the third type of cone that is present in humans and that contains pigments sensitive to long wavelengths (red light). Therefore, mice can make dichromatic color discriminations and have some capacity for color vision, which does not happen for example in rats [66].

The region of highest visual acuity of the human retina is called the fovea. It is surrounded by the macula, it does not contain rods and it is the region of the retina that has the highest density of cones.

However, the mouse retina lacks this structure. The distribution of rods is relatively uniform across the retina, while the distribution of cones is markedly varied.

After stimulation by light, the rods and cones trigger electrical signals in bipolar cells. These transmit both excitatory and inhibitory signals to retinal ganglion cells (RGC), which become depolarized and generate nerve impulses [60] that are projected to more than 20 subcortical areas [67]. It has been shown that there are at least 22 distinct types of RGCs [68], with some of them being direction-selective [69]. The RGCs are then collected in a bundle at the optic disk to form the optic nerve that exits in the posterior part of the eye [70], as shown in Figure 1.15. The optic nerves then meet at the optic chiasm, located at the base of the hypothalamus, from where the optic tract starts. There is also a direct retinohypothalamic projection to the suprachiasmatic nucleus that generates and regulates rhythms in behavioural state, performance, hormonal secretion and physiological function.



Figure 1.15 – Schematics of the mouse visual system. (Left) Schematic of the mouse visual pathway. Ipsilateral axons form a few small patches at the LGN, SC and V1 (green patches), while contralateral terminals fill the rest of the tissue (red) (extracted from [59]). (Right) Geniculate (red) and extrageniculate (orange) pathways of the rodent visual system (extracted from [71]).

The optic nerve fibres that originate from the nasal part of each retina cross to the opposite side of the brain in the optic chiasm, while the fibres from the temporal parts continue on the ipsilateral side [58]. This way, the right side of the brain will receive information from the left visual field, while the left side will receive information from the right visual field [59]. Whereas in humans the number of ipsilateral and contralateral RGC axons is approximately equal, the mouse has a smaller degree of binocular overlap in the visual field (about 40°-50° [72][73]) due to the fact that the eyes are laterally positioned in the head. Therefore, more than 95% of the optic nerve fibres cross the midline to the contralateral side of the brain [59].

Each optic tract then projects to three main subcortical structures: the lateral geniculate nucleus (LGN) of the thalamus via the geniculate pathway, the superior colliculus (SC) via the extrageniculate pathway, and the pretectal area of the midbrain, that uses retinal input to produce pupillary and

accommodation reflexes [58][59]. A scheme of the geniculate and extrageniculate visual pathways is presented in Figure 1.15.

The LGN lies at the ventrocaudal aspect of the thalamus and is responsible for processing visual information that ultimately results in visual perception. It shows a different anatomical organization in the human and mouse. In the human, the LGN is stratified into six cell layers. Fibres from the retina of the ipsilateral eye terminate in the second, third and fifth layers, while the crossed optic nerve fibres terminate in the remaining three layers, as seen in Figure 1.16. The mouse LGN, however, lacks this lamination pattern. The predominant innervation to the LGN comes from the contralateral eye, with only a small ipsilateral patch [58][59]. The axons of the neurons from the dorsal LGN form the optic radiation that then projects and transmits visual information to the primary visual cortex (V1), also called striate area, at the medial hemispheric surface at the occipital lobe [58][59]. In addition, the LGN also receives many strong feedback corticofugal projections from V1 [58].

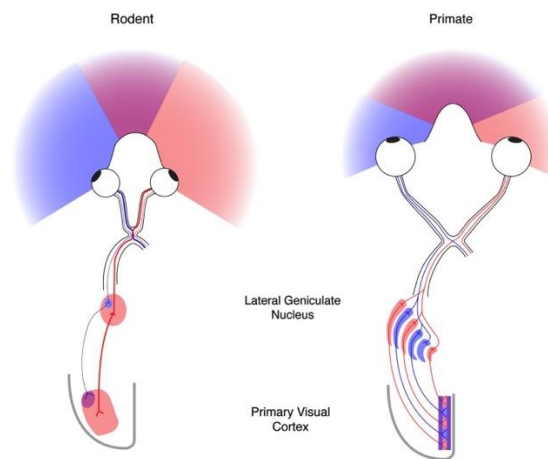


Figure 1.16 – Schematic of the rodent and human visual geniculate pathways (extracted from [3]).

The superior colliculus in the dorsal midbrain constitutes a major relay structure for visual and visuo-motor behaviour. The SC is a horizontally layered structure, with a number of layers that varies according to the species. Neurons in the superficial layers of the SC receive information from the retina and the visual cortex through two major afferent projections and respond to visual stimuli. On the other hand, the deep layers are motor-related, capable of controlling eye movements [59][74][75], and the intermediate layers have cells with sensory and motor properties. It is known that the superior colliculus mediates visual reflexes [58] and is an important structure for the initiation of defensive behaviours [76], orientation of head and body movements [77] and for navigation [78] through the integration of visual, somatosensory and auditory information. It has also been shown that the SC projects via the lateral posterior nucleus to the secondary visual cortex (V2). Moreover, the potential for plasticity of the rodent SC has been the subject of increasing interest [79][80].

The mouse visual cortex encompasses six functional areas and has a retinotopic organization [81], which means that different regions of the visual image formed on the retina are represented in an organized manner in the visual cortex. The primary visual cortex, or area 17 of Brodmann's, is the

terminal station of the optic radiation from the dorsal LGN and its functional and anatomical organization is also different between humans and mice. In humans, V1 shows a functional subdivision into columns that share a preference for one eye over the other. Columns for the right retina alternate with columns for the left retina (ocular dominance columns). In addition to these columns, there are periodically arranged cell populations that responds in a characteristic fashion to the orientation of lines in the visual field (orientation columns) [58]. This fine organization into columns has, however, not been observed in mice [82][83]. The V1 of the mouse is mostly monocular, having only a small binocular region that receives thalamocortical input from both hemispheres [59]. Moreover, V1 is known to send part of its output to a series of extrastriate visual areas that are responsible for complex integration of visual information.

Although V1 and SC neurons of the mouse are less organized and clustered into functionally distinct areas than those of humans, it has been shown in multiple electrophysiological and calcium and intrinsic signal imaging studies that they demonstrate orientation selectivity, direction selectivity and spatial and frequency tuning to stimuli, as well as a topographic organization that reflects the visual image perceived by the retina [6][7][8][9][84][85][86][87][88][89][90][91]. Unfortunately, there is not yet any fMRI study that tried to investigate these intricacies of the mouse visual system.

1.5. Anaesthesia in Rodent fMRI Experiments

The evolution of fMRI in the last decades as a technique to image live animals in a non-invasive and clinically translatable way has enabled its application in longitudinal studies within the same animals and studies about the progression of diseases or the effects of drug candidates on different tissue or organs of the body. However, this also represents a challenge as, in contrast to humans, small animals such as mice often require anaesthesia to ensure their humane restraint and avoid their gross motion during imaging, although some awake animal fMRI studies have already been reported [92][93]. Anaesthesia involves a triad effect that includes loss of consciousness with a concomitant loss of sensation (analgesia) with muscle relaxation (immobilisation) [94]. Moreover, it likely reduces changes in attention during an fMRI session that could affect BOLD signals, a common confounder in human fMRI studies [95]. However, the use of anaesthesia also causes an inevitable autonomic nervous system depression that induces cardiovascular, respiratory and thermoregulation depression, affecting body metabolism. Due to their high body surface/weight ratio and metabolic rate, rodents are likely to suffer hypothermia, which is a frequent cause of mortality in these animals [96].

All of these changes may drastically disturb the animal's homeostasis and affect the blood flow and blood oxygenation values [97], thereby compromising neurovascular coupling and confounding the quality and interpretation of fMRI images. Anaesthesia alters neural function and hemodynamic responses, potentially resulting in a slower time to peak and smaller amplitude BOLD responses. Thus, a good anaesthesia regime guarantees sufficient sedation without compromising the well-being of the animals and the detection of a hemodynamic response associated with the stimulus. Moreover, the need for long acquisition times of some fMRI experiments requires that the anaesthetic being used is able to ensure the animal's homeostasis and constant depth of anaesthesia throughout the whole

scanning period. This is further complicated by the fact that different species and strains may react differently to the same anaesthetic agent [98].

In this regard, inhalation anaesthesia is usually recommended. Inhaled anaesthetics are quickly eliminated via the lungs, which allows a quick recovery and regain of normal physiology and a better control of hypothermia and fluid or electrolyte imbalances. Injectable agents need to be metabolised by the liver and excreted by the kidneys, which makes recovery more complicated. Nevertheless, some injectable anaesthetics such as medetomidine, fentanyl and midazolam have specific antagonists that speed recovery and overcome some of these problems [99]. Their dose rates depend on the species being used, strain, administration route, age, sex, body condition, environment, experimental setup, level of anaesthesia required, among others [100].

Isoflurane is a highly volatile anaesthetic agent that has been extensively used in fMRI experiments with rodents because it is minimally metabolised by the liver and has low mortality rates [101]. It acts on γ -aminobutyric acid type A (GABA_A) receptors, depressing excitatory synaptic transmission [102]. However, isoflurane has been shown to cause neural, cardiovascular and respiratory depression [92][103]. It also increases basal CBF in a dose-dependent manner, limiting neurovascular reactivity [103].

Medetomidine is an α_2 -adrenoreceptor agonist with sedative and analgesic properties and negligible respiratory and small cardiovascular effects. It predominantly acts on presynaptic receptors in the locus coeruleus, resulting in decreased noradrenaline release and therefore a general inhibition of the sympathetic nervous system [104]. Furthermore, its effect can be easily reversed with the α_2 antagonist atipamezole, making it the anaesthetic of choice for longitudinal rodent fMRI studies [105]. In 2006, Weber et al. developed a fMRI protocol for longitudinal experiments using sedation with medetomidine and observed a robust and significant BOLD response to forepaw stimulation in the rat brain [106]. Later in 2010, Adamczak and colleagues established a similar protocol, but for mice [44]. Since then, the use of medetomidine has been proven very successful in multiple fMRI studies [107][108]. In fact, robust activation in the visual cortex of rodents had been difficult to observe [109][110][111][112][113][114] until researchers started to use medetomidine for anaesthesia in fMRI experiments [17][115][116]. However, the use of medetomidine in mouse fMRI also has its shortcomings. The depth of anaesthesia is often not constant throughout the scanning session and tends to decrease to a point in which mice start moving, sometimes dictating the premature end of the session. Moreover, some mouse strains have shown resilience to sedation with this anaesthetic [20][117], which prevents it from being used in cross-comparative fMRI studies of genetically engineered mouse models.

Therefore, in 2016, Petrinovic et al. suggested a novel anaesthesia procedure based on etomidate [20], an injectable anaesthetic that acts on the β -subunit of GABA_A receptors and that has low analgesic properties [118]. Also, it has been reported that etomidate has neutral effects on blood pressure and minimal effects on respiratory and cardiac function [119]. Petrinovic and colleagues have quantitatively assessed local brain perfusion, cerebrovascular reserve capacity and functional responses to pharmacological intervention in mice of different strains and Sprague Dawley rats that

were sedated with etomidate, medetomidine and isoflurane [20]. They saw that cerebrovascular reserve capacity was compromised with isoflurane due to its strong vasodilatory effect, and that medetomidine had a limited effectiveness in sedating some of the strains. On the contrary, etomidate led to a deep and stable anaesthesia across all strains with intact cerebrovascular dynamics upon hypercapnic, pharmacological and sensory stimulation, and afforded full recovery from anaesthesia, thus making it the anaesthetic of choice for comparative and longitudinal fMRI studies across a wide variety of rodent models. More recently, in 2017, Klee and colleagues suggested a fMRI-compatible anaesthesia protocol for mice upon subcutaneous administration of etomidate in order to avoid the large infusion volumes and complex experimental setup that intravenous infusion requires for small rodents [22].

1.6. State of the Art of Rodent Visual fMRI

To date, most of the visual stimulation fMRI experiments in rodents were based on stationary flickering stimulation. This has been accomplished in most of the times by using light emitting diodes (LEDs) coupled to long fibre optic cables that conduct the light to the scanner bore in order to stimulate one or both eyes of the animal [16][17][110][111][112][113][116][120][121][122][123][124][125]. Exceptions to that include an experiment that employed a laser [17] and another that employed a light bulb [109] as light sources connected to optical fibres. There was also another fMRI study that used a stroboscopic light source that was placed in front of the magnet [115]. This approach had, however, the disadvantage of needing to compensate for auditory evoked BOLD responses due to the clicking sounds emitted by the strobe unit. These visual stimulation setups have allowed so far to map brain or retinal activity in response to different flickering frequencies [16][17][115][116][123], light intensities [112][123] and colours [16][123][124].

In 2009, Chan and colleagues investigated the development of visual activations in the rat visual pathway from the time of eyelid opening to adulthood [110], laying a foundation for using fMRI to study functional plasticity and visual maturation in normal or injured developing brains. Later that year, the same group saw residual visual functions on both sides of the subcortical rat brain at postnatal day 60 after neonatal hypoxic-ischemic-injury of the left visual cortex, providing important evidence on functional plasticity of the brain upon injury [111]. In 2011, Lau et al. found significant differences in the temporal dynamics of BOLD responses to short duration (1 s) visual stimuli in the rat SC and LGN. They showed that the signal from the SC rises faster but settles slower than the signal from LGN, suggesting that this difference could be related to depth-dependent differences in blood vessel dilation rate [113].

Still in 2011, Lau and colleagues developed an innovative visual stimulation system composed of four optical fibres illuminated by identical LEDs that were positioned in a linear array in front of one eye [114]. Therefore, when the fibres were flashed sequentially at specific on-off intervals, an apparent back-and-forth motion of a light spot could be produced. They were the first and, to date, the only group to employ fMRI to investigate motion responsiveness in the rodent brain and stimulus speed dependence in the SC and in the LGN. Their work consisted of examining the hemodynamic response

amplitude and extent of activation within the SC and LGN of Sprague-Dawley rats to different stimulus speeds. Their results show that responsiveness in these structures increases monotonically with increasing speed, although a strong decline has been observed in both regions at the highest speed tested (164°/s).

While all of the studies described above have been performed in rats, so far only three visual stimulation fMRI experiments used the mouse as an animal model. The first one was done in 1996 by Huang and colleagues [109]. Although BOLD responses have been observed in the visual cortex following flickering visual stimulation, their study did not report any activation in subcortical regions that represent important relay sites to the cortex. In 2016, Niranjana et al. investigated the use of snapshot GE-EPI, the stimulus frequency dependence and the difference between using bright flashes against a dark background and dark flashes against a bright background in the mouse brain [17]. More recently, in 2017, the same group demonstrated the feasibility of line-scanning fMRI in the mouse brain for measuring BOLD signals at a higher temporal resolution (200 ms) than what is typical in fMRI studies (1 to 3 seconds) [125]. This was accomplished by using a GE pulse sequence without phase encoding in combination with saturation bands, therefore sacrificing the generation of three-dimensional (3-D) maps.

In a general overview, these studies were able to show BOLD activation in the retina, primary and secondary visual cortex, superior colliculus, lateral geniculate nucleus, lateral posterior nucleus and pretectum of the anesthetized rodent brain, being isoflurane and medetomidine the most common choices for the sedation and restraint of the animals.

1.7. Thesis Outline

As reported in the beginning of this chapter, there are two main factors that compromise the growth of fMRI as a technique to study vision in the mouse. The first one is the lack of evidence that supports the use of subcutaneously administered etomidate as an anaesthetic agent in mouse fMRI studies. Secondly, most fMRI experiments that studied the visual system of rodents have relied on simple visual stimulation setups that do not have the capability to deliver more complex stimuli and allow the study of other features of the brain regions associated with vision, such as their retinotopy, preference for specific orientations, directions of movement or shapes. Furthermore, the long and narrow scanner bores, the high-field strengths of pre-clinical MRI scanners and the susceptibility to radiofrequency interference make it even more difficult to build a new and more complex MR-safe mouse visual stimulation system that can probe a large portion of the visual field.

Therefore, with this project, one hopes:

- to investigate the BOLD response dynamics following flickering visual stimuli of different light intensities and frequencies on mice anesthetized with subcutaneous injection of etomidate;
- to compare the ensuing maps with others obtained while using medetomidine and thus validate the use of subcutaneously administered etomidate as the anaesthetic of choice for longitudinal fMRI studies across a wide variety of mouse models;

- to optimize the current free-breathing protocol for subcutaneous administration of etomidate at recoverable doses in mice [22];
- to design and develop a system for preclinical fMRI of the visual pathway in mice, capable of delivering accurate and complex (e.g. moving stimuli, projection of different shapes, polychromatic, etc.) visual stimuli, and that, when coupled to the high-field MRI scanner, enables the high signal-to-noise ratio, spatial resolution and sensitive investigation of the entire pathway in the anesthetized or awake mouse.

2

Materials and Methods

This chapter describes in detail all of the steps that were performed in order to concretize the objectives defined for the project. Specifically, the experiments that were executed to validate the implementation of the new subcutaneous anaesthetic protocol are explained, as well as the logic behind the construction of the MRI safe visual stimulation system.

All aspects of these study were preapproved by the Champalimaud Centre for the Unknown's Ethics Committee operating under Portuguese and EU Law.

2.1. Visual Stimulation fMRI Experiments

Three different kinds of experiment were designed to investigate the applicability of subcutaneous etomidate on BOLD fMRI in the mouse, based on the presentation of binocular flickering stimuli. The first experiment investigated the BOLD responses of etomidate-sedated mice to different light intensities (Experiment 1). The second one explored the frequency tuning capability of etomidate-sedated mice, using the light intensity from the first experiment that evoked stronger responses in vision associated areas of the brain (Experiment 2). Finally, for comparison purposes, one stimulation condition from the previous experiments was chosen and presented to medetomidine-sedated mice (Experiment 3). The following subsections describe in a detailed manner the setup used for delivery of visual stimuli, the way animals were prepared for the experiments inside the scanner, the MRI acquisition protocol, the visual stimulation paradigm, and the analysis steps that were used to obtain valid conclusions from these experiments.

2.1.1. Setup for Delivery of Stationary Visual Stimuli

As in other visual stimulation fMRI studies [16][17], a fibre-coupled LED was used as a source of light. In particular, an LED with central wavelength located at 470 nm (blue) was chosen (LEDC_HB01-B_FC, Doric Lenses, Canada). The driver used to regulate the high-power LED (LEDD1B T-Cube driver, Thorlabs, United States of America) features a control knob that allows output current tuning from 0 to 1200 mA and, therefore, LED brightness tuning, and can be externally controlled by a voltage in the 0 to 5 V range. Both devices can be seen in Figure 2.1.



Figure 2.1 – LED and LED driver employed for accurate delivery of stationary visual stimuli. (Left) Connectorised high-brightness LED used as a light source (extracted from [126]). (Right) LED driver used to control the LED (extracted from [127]).

Synchronization with the MRI scanner protocol and accurate control of the stimulus presentation were accomplished through an Arduino microcontroller (Arduino Mega 2560, Arduino, United States of America) for trigger detection and LED driver control. The pulse sequences used for imaging were programmed in the scanner operator console to send triggers, i.e. transistor-transistor logic (TTL)

signals, at specific time points chosen by the user, that could be detected by the Arduino. The latter, for its part, has been programmed to switch the LED current on and off according to the user needs.

An ~8 m two-branching fibre-optic patch cord (BFP(2)_200/220/2000-0.53_8m_FCM-2xZF1.25(FP), Doric Lenses, Canada) was then coupled via a metal ferrule connector to the LED in order to leave all electronics in the control room, conduct the light to the magnet bore in a MRI-compatible fashion and allow binocular stimulation. A 1.25 mm inner diameter and 6.8 mm length Zirconia sleeve (SLEEVE_ZR_1.25, Doric, Canada) was then connected to the Zirconia ferrule at each of the two fibre-optic patch cord ends in order to diffuse light, rendering it less aggressive to the eyes of the mouse.

In order to guarantee that the fibres would always be placed in the same position across experiments, i.e. at approximately 1 cm from each eye, a pair of 3-D printed custom pieces was designed in Autodesk Fusion 360 software for students. Each piece was built to fit one side of the mouse bed used in all experiments, which was also 3-D modelled to be used as a reference, and to allow the insertion of one fibre-optic patch cord through its hole and therefore its accurate positioning, as it can be seen in Figure 2.2.

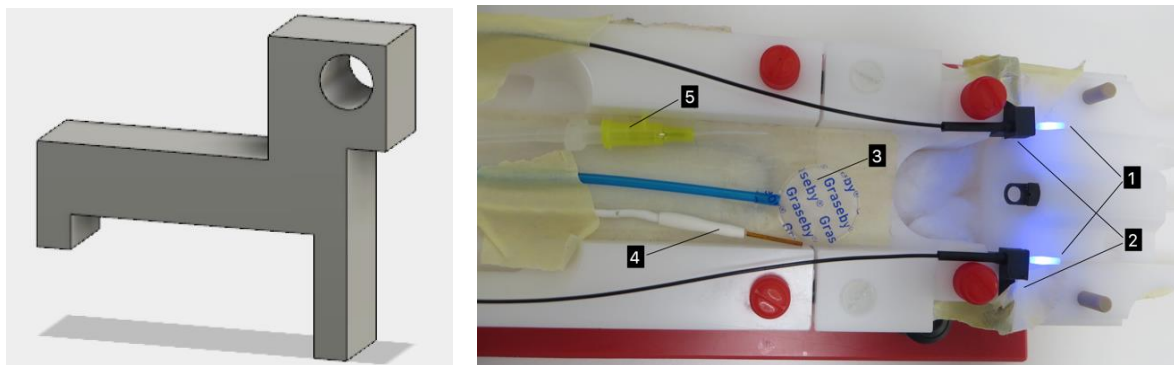


Figure 2.2 – Visual stimulation setup used for delivery of stationary flickering stimuli inside the scanner. (Left) 3-D modelled piece designed for accurate positioning of each fibre-optic patch cord across experiments. (Right) Experimental setup for visual pathway mapping in the mouse. (1) Fibre-optic cables with Zirconia sleeves, (2) 3-D printed pieces for stable positioning of the fibre-optic cables, (3) Pressure sensitive pad for respiration monitoring, (4) Rectal probe for temperature monitoring, (5) Catheter for delivery of anaesthesia.

The light output power and intensity reaching each eye of the mouse from each fibre were measured using a handheld digital power meter console (PM100D, Thorlabs, United States of America) and a photodiode power sensor with an aperture diameter of 9.5 mm (S130C, Thorlabs, United States of America). This way, the positions of the LED driver control knob could be defined before the beginning of the experiments for each of the light intensities chosen to test.

2.1.2. Animal Preparation

A total of 11 male C57BL/6J mice aged between 7 to 8 weeks old were used in these experiments: 4 weighing 23.7 ± 2.5 g for Experiment 1, 4 weighing 25.7 ± 0.9 g for Experiment 2, and 3 weighing 25.7

± 1.1 g for Experiment 3 (weight values indicated as mean ± standard deviation). Mice were reared in a temperature-controlled room and held under a 12/12 hour light/dark regimen with standard chow and water supply *ad libitum*.

Anaesthesia was induced with a mixture of 5% isoflurane (Vetflurane, Virbac, France) and ambient air maintained by an isoflurane vaporizer (VetEquip, United States of America) in a custom-built plastic anesthetizing box. Oxygen levels were carefully maintained at 27-30% with the aid of an oxygen sensor (MX300-I, Viamed, United Kingdom). Once the mouse had loss of righting reflex, isoflurane concentration was reduced to 3% for maintenance during preparation and the animal was moved to a balance (Traveler TA1501, Ohaus, Switzerland), weighted, placed in the prone position on an animal bed (Bruker BioSpin, Germany) and stabilized with a bite bar and a nose cone through which all gases were continuously being supplied. Temperature and respiration sensors (Model 1030 Monitoring Gating System, S.A. Instruments, United States of America) were placed for real-time monitoring of mouse physiology and to allow the possibility to later compensate for some variability in fMRI data through the identification of changes over time that might influence the quality of the images. A heated water bed was also used to avoid body temperature to drop dramatically once the animals were immobile, and eye drops (Bepanthen Eye Drops, Bepanthen, Germany) were applied in both eyes to prevent drying of the corneas.

In Experiments 1 and 2, a 24G x 3/4" infusion needle was inserted in the mice and a subcutaneous bolus of etomidate (Etomidate-Lipuro 2 mg/ml, B. Braun Melsungen AG, Germany) at 23 mg/kg was injected, followed by a constant infusion of 0.6 mg/kg/min initiated 5-10 min after bolus and delivered by a syringe pump (GenieTouch, Kent Scientific, United States of America), according to the protocol suggested by Klee et al. [22]. For Experiment 3, anaesthesia was maintained with a subcutaneous administration of medetomidine (Dormilan 1 mg/ml, Vetpharma Animal Health S.L., Spain) previously diluted 1:10 in saline, at 0.4 mg/kg for bolus and 0.8 mg/kg/h for infusion initiated 10 minutes after bolus, similar to the protocol suggested by Adamczak et al. [44].

Following administration of the bolus, isoflurane was gradually discontinued at a rate of approximately 0.3% per minute so that no isoflurane was available after the next 10 minutes.

At the end of fMRI Experiment 3, medetomidine was antagonized by a subcutaneous injection of atipamezole (Antidorm 5 mg/ml, Vetpharma Animal Health S.L., Spain) also diluted 1:10 in saline, at 2 mg/kg, and mice were allowed to recover before being returned to their original cages (usually 15 minutes after injection). After Experiments 1 and 2, mice were placed inside a cage with a heating pad below in order to prevent hypothermia until complete recovery from anaesthesia.

2.1.3. MRI Protocol

All MRI experiments were carried out on a 9.4T horizontal MRI scanner (BioSpec 94/20 USR, Bruker BioSpin, Germany) equipped with a gradient system capable of producing up to 660 mT/m in all directions. An 86 mm inner diameter quadrature resonator was used for RF transmission (RF RES 400 1H 112/086 QSN TO AD, Bruker BioSpin, Germany) and a 10 mm inner diameter loop surface coil

was used for signal reception (RF SUC 400 1H ID=10 LIN RO AD LNA, Bruker BioSpin, Germany) that was placed over the dorsal side of the head between the two ears and connected to its preamplifier (RF SUC 400 1H LNAV3, Bruker BioSpin, Germany).

Once the animals were sedated and the receiver coil was placed above the head, the entire assembly was placed inside the bore of the scanner, which was then covered with cardboard and a blanket to prevent the entrance of external light. Scout images were acquired in three orthogonal planes with a Fast Low Angle Shot (FLASH) pulse sequence (TR = 100 ms, TE = 2.3 ms, flip angle = 30°, matrix size = 256 x 256, FOV = 40 x 40 mm², slice thickness = 1.0 mm) in order to assess the quality of position of the head in 3-D. If the head was tilted, the animal was removed from the scanner and repositioned until it became as aligned in the scanner as possible. Once the animal was properly positioned in the scanner, the FOV was decreased and another scan was acquired with a FLASH pulse sequence (TR = 50 ms, TE = 3.5 ms, flip angle = 20°, matrix size = 160 x 160, FOV = 16 x 16 mm², slice thickness = 0.6 mm) in order to optimize the location of the slices in the high-resolution structural scan and in the functional scans. A B_0 field map was then obtained and field inhomogeneities were corrected through shimming in a cuboid volume that contained the slices of the brain to be imaged in the anatomical scan. This step was sometimes done twice during the session because distortions in the magnetic field tend to reappear in the middle of the session due to scanner drift.

High-resolution anatomical images were acquired using a Rapid Acquisition with Relaxation Enhancement (RARE) sequence with: RARE factor = 8, number of averages = 4, TR = 2000 ms, TE = 8.8 ms, matrix size = 200 x 160, FOV = 20 x 16 mm², and 20 parallel 0.6 mm thick coronal slices, such that the fourth slice was approximately centred in the transverse fissure of the brain, as shown in Figure 2.3. A saturation band was also placed below the ventral part of the brain to suppress the MR signal from tissues outside the brain. Moreover, slice acquisition order was interleaved with the order being [1 3 5 7 9 11 13 15 17 19 2 4 6 8 10 12 14 16 18 20].

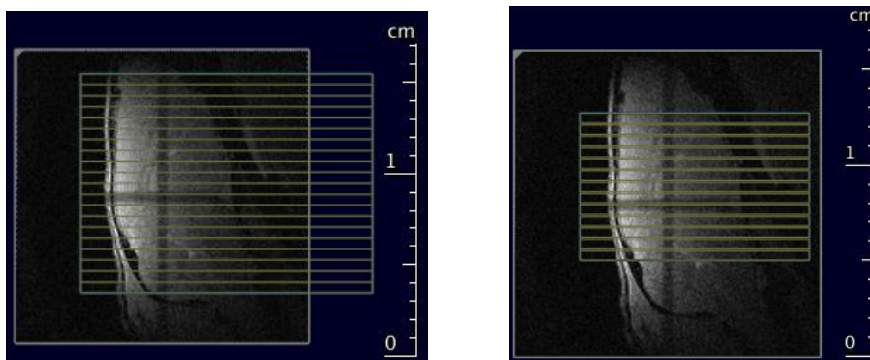


Figure 2.3 – Definition of the position of the slices for the structural and functional scans. (*Left*) Sagittal image of the brain with representation of the slices for the anatomical scan. (*Right*) Sagittal image of the brain with representation of the slices for the fMRI acquisitions.

After the anatomical scan, fMRI data were acquired using a GE-EPI sequence with: TR = 1000 ms, TE = 15 ms, matrix size = 120 x 84, FOV = 17 x 12 mm² (yielding, therefore, an in-plane resolution of 142

x 143 μm^2), flip angle = 55°, and 13 parallel coronal slices each 0.5 mm thick, separated by gaps of 0.1 mm, such that the first slice was approximately centred in the transverse fissure of the brain, as shown in Figure 2.3. Slice acquisition order was also interleaved with the order being: [1 3 5 7 9 11 13 2 4 6 8 10 12].

2.1.4. Visual Stimulation

Animals were stimulated with the blocked design paradigm shown in Figure 2.4, each block encompassing 40 volumes at rest and 20 volumes at visual stimulation (since the temporal resolution of the fMRI scans was 1 volume/s). This basic block was repeated 5 times in an entire fMRI run, resulting in 340 GE-EPI volumes acquired in each 340 s length run.

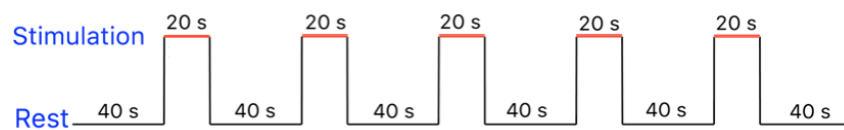


Figure 2.4 – Block paradigm used for all fMRI experiments. Rest periods were 40 s long, while stimulation periods were 20 s long (indicated by the red bars).

In Experiment 1, two different stimulation frequencies (2 Hz and 10 Hz) and three different light intensities ($9.2 \times 10^{-3} \text{ W/m}^2$, $9.2 \times 10^{-2} \text{ W/m}^2$ and $8.1 \times 10^{-1} \text{ W/m}^2$) were chosen based on previous studies of visual stimulation responses in the rodent brain [17][112], resulting in 6 different stimulation conditions. The duration of the stimulation pulses was always 10 ms. Each fMRI scan was conducted twice for each condition in a pseudo-random order, with the constraint that all 6 conditions had to be presented once before their repetition. This resulted in 12 runs per mouse. Mice were allowed to rest 7-10 minutes between runs. In total, each experimental session lasted about 4 hours, with approximately 30 minutes for animal preparation, 30 minutes for scanner adjustments and preparatory MRI scans, and the remaining 3 hours for acquisition of fMRI data.

In Experiment 2, the duration and intensity of the flickering pulses were kept constant at 10 ms and at $8.1 \times 10^{-1} \text{ W/m}^2$, respectively. Stimulation frequencies, on the other hand, were varied between 2 Hz, 5 Hz, 10 Hz and 20 Hz. Each condition was again repeated twice for each mouse, resulting in a total of 8 runs per mouse. Moreover, the mice were allowed to rest for 7 minutes before the beginning of another run. This experiment lasted about 3 hours and 10 minutes per session.

In Experiment 3, only one condition was tested: the LEDs were flashed at a frequency of 2 Hz and a pulse width of 10 ms, and light intensity reaching the eyes was fixed at $8.1 \times 10^{-1} \text{ W/m}^2$. Between 5-9 runs were completed for each mouse in every session, depending on the animal's physiological stability, with intervals of 8 minutes between each run. In total, 19 runs were acquired for the 3 mice: 8 for one mouse, 5 for another, and 9 for the other one.

2.1.5. Data Analysis

All data was analysed using the Statistical Parametric Mapping (SPM) package developed by the Wellcome Trust Centre for Neuroimaging at the University College London, and some user-defined functions and routines in Matlab. The ImageJ software [128] was also used to draw ROIs for the ROI analyses.

Anatomical and functional images were converted to NIfTI format, and videos of each slice for each functional run were displayed for detection of large movements or abnormal oscillations in the data that could prevent the continuation of the analysis of that dataset.

Functional images' SNR was calculated by dividing the mean intensity of an ROI inside the brain in a single time point by the standard deviation of another ROI centred outside of the brain, and averaged over all animals.

A mask covering the brain was then designed and temporarily applied to each functional run, in order to only analyse voxels that contained brain tissues. The average signal timecourse in each brain slice was plotted for detection of signal fluctuations in relation to the 2nd degree polynomial that was fitted to that timecourse. In addition, the signal from each voxel in the brain slice was displayed in a 2-D map in order to also help detecting those outliers in the data. After manual selection of those time points, the intensity of the voxels in the non-masked slice at those time instants was replaced by doing a cubic spline interpolation from the signal those voxels had in the remaining time points. In average, 8% of each slice's frames (about 27 out of 340) were corrected in each functional run of Experiment 1, 2% of each slice's frames (about 6 out of 340) were corrected in Experiment 2 and 6% of each slice's frames (about 21 out of 340) were corrected in Experiment 3.

Images from each functional run were then corrected for slice-timing differences using sinc-interpolation and realigned to the mean volume. If the functional images from a session were strongly misaligned with the anatomical ones, a manual alignment was then done in order to get a good enough first approximation between them. Coregistration was then finalized by estimating the rigid body transformation between the anatomical volume and the mean volume from each functional run, which were both brain masked in order to prevent fat and bone tissues from affecting the estimation of the transformation matrix. This transformation was then applied to all of the images from the corresponding run. In order to normalize all of the brains, the Allen mouse brain atlas (2012 version) [129] was used as a reference. At first, anatomical and functional images were manually aligned with the reference brain. Thereupon, the affine transformation between the masked anatomical image from each session and the reference brain was estimated and applied to all anatomical and functional images from that session. Both these transformations (rigid and affine) led to anatomical and functional images from all the mice being positioned exactly in the same space, as it is depicted in Figure 2.5 for one mouse.

Finally, fMRI data was spatially smoothed using a 3D Gaussian kernel with a full width at half maximum (FWHM) of 0.28 mm before GLM fitting.

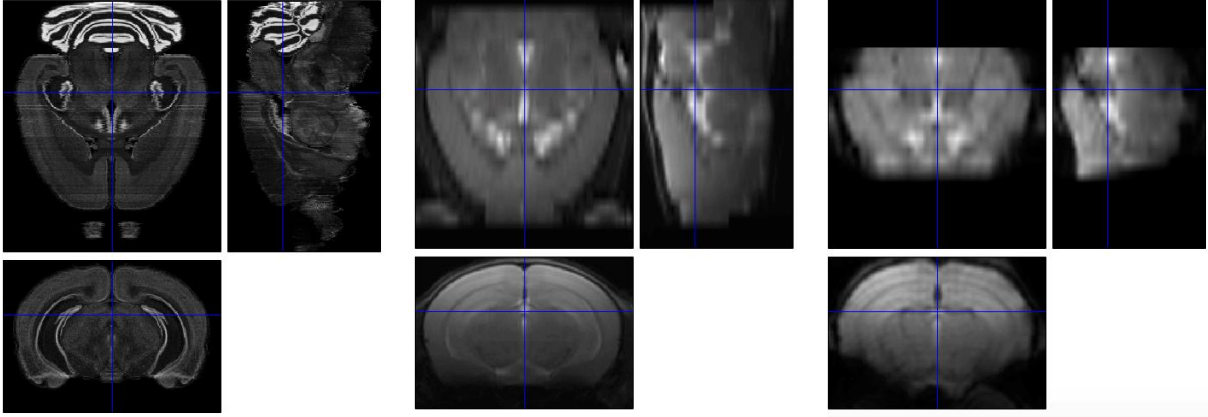


Figure 2.5 – Brain alignment after coregistration and normalization. (*Left*) Axial, sagittal and coronal slices of the mouse brain atlas that was used as a reference for normalization [129]. (*Middle*) Axial, sagittal and coronal slices of a mouse’s anatomical volume. (*Right*) Axial, sagittal and coronal slices of the mean volume from a functional run of the same mouse. Blue lines intercept exactly in the same position of the brain in the three volumes presented.

For statistical parametric mapping, a 1st level GLM analysis was conducted for each functional run and for each subject under each condition (single subject fixed-effects analysis). A fixed-effects group analysis was then done by including all subject scans for each condition in a single GLM in order to build global maps of activation for each condition. In either case, each functional run was regressed with the predicted BOLD response as the experimental regressor and the six realignment parameters as nuisance regressors. The former was calculated from the convolution of the stimulus paradigm (which was assumed to be representing neural activity) with a HRF representing neurovascular coupling, which was chosen to be modelled by a double-gamma function [52]:

$$h(t) = \frac{1}{C} \left[\frac{t^{n_1-1}}{\lambda_1^{n_1} (n_1 - 1)!} e^{-\frac{t}{\lambda_1}} - a \frac{t^{n_2-1}}{\lambda_2^{n_2} (n_2 - 1)!} e^{-\frac{t}{\lambda_2}} \right] \quad (2.1)$$

where a is a constant between 0 and 1 that measures the magnitude of the post-stimulus undershoot, n_1 and λ_1 primarily model the early peak and n_2 and λ_2 model the late dip in the HRF. The constant C guarantees that the area under the HRF is equal to 1. In order to assure that the chosen function adequately modelled the BOLD response in regions of the visual pathway, 9 different sets of parameters were tested in a few datasets. The resulting functions and their respective convolution with a block of the stimulus paradigm are plotted in Figure 2.6. The values of the parameters that describe those functions and the time instants where they peak can be found in Table A.1. Specifically, GLM analysis and t -tests were performed in 6 functional runs from different individuals using each of the 9 different HRFs. The function that was chosen was the one that resulted in higher t -values in visual pathways regions (SC, V1 and LGN). In particular, the HRF peaking at 1.40 s after the stimulus was chosen (HRF number 3 in Table A.1).

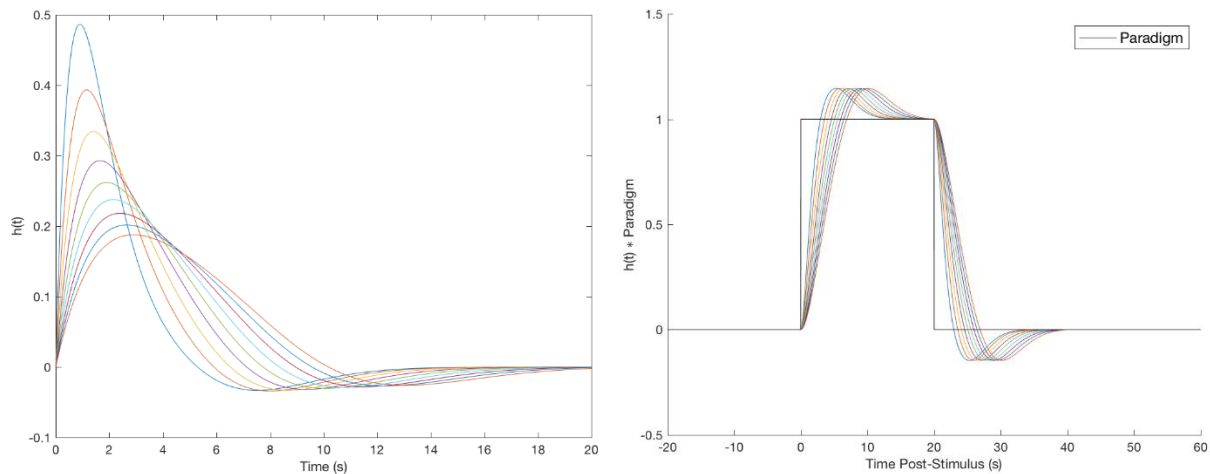


Figure 2.6 – Models of HRFs that were tested. (Left) Plot of the 9 different HRFs that were tested. Peaks between consecutive functions are 0.25 s apart. (Right) Plot of the convolution of each function with a block of the stimulus paradigm. Initial peaks between consecutive responses are 0.61 s apart.

The default SPM12 options of grand mean scaling and auto-correlation modelling were also used, with a high-pass filter of 80 s to remove slow signal drifts. Moreover, voxels were only analysed if they were included in a brain mask that was manually drawn. Once the design matrices had been built, the parameters of the GLM were estimated and positive and negative contrasts were defined. A t -test was then performed for both contrasts on a voxel by voxel basis to test the null hypothesis that the visual stimulation does not increase or decrease the BOLD signal. The p -value and the minimum cluster size thresholds for statistical significance were respectively set at 0.02 and 8 to build the single subject statistical parametric maps, and at 0.001 and 8 to build the group maps.

In order to conduct ROI analyses, ROIs were drawn around the SC, the LGN and the V1 on the reference brain according to the Paxinos and Franklin's mouse brain atlas [130]. Since visual stimuli were always binocular, ROIs included both brain hemispheres. These masks were then applied to the normalized unsmoothed images and the average time series from all enclosed voxels was computed. Thereafter, each timecourse was detrended and normalized to percentage signal change by estimating the 2nd degree polynomial that best fitted to it using the rest data points, subtracting this curve from the timecourse, and dividing each resulting time series by the median value of the rest periods. Timecourses were then averaged over stimulus blocks for each run so that a representative cycle could be shown. Finally, both the timecourses and the average cycles were averaged across runs and mice and the BOLD peak amplitude of the average cycles was registered.

2.2. Optimization of Etomidate Dosage

Due to the high mortality rate of mice anesthetized with etomidate that was observed in the experiments described in Section 2.1, some bench tests were performed in order to understand if it was possible to decrease the dosage of etomidate and thus decrease the mortality rate that comes from it, while maintaining a constant depth of anaesthesia throughout the whole experiment.

For that, 9 male C57BL/6J mice weighting 26.3 ± 1.8 g and aged between 7 to 8 weeks old were used. Animal preparation was done exactly in the same way it was described for Experiments 1 and 2 in Subsection 2.1.2, with the exception that etomidate concentration and isoflurane discontinuation were modified. Mice were injected with a 23 mg/kg bolus and a constant infusion of 0.6 mg/kg/min initiated 5 minutes after bolus of etomidate as before. However, after 35 minutes of bolus, mice were randomly assigned to 3 different groups of 3 animals each:

- group 1 continued to be administered a constant infusion of 0.6 mg/kg/min;
- group 2 started to be administered a constant infusion of 0.3 mg/kg/min, i.e. $\frac{1}{2}$ of the concentration that was previously being injected;
- group 3 started to be administered a constant infusion of 0.2 mg/kg/min, i.e. $\frac{1}{3}$ of the concentration that was previously being injected.

Furthermore, discontinuation of isoflurane was extended in time because some mice from Experiments 1 and 2 in Section 2.1 tended to have a burst in respiration rate and move when isoflurane was completely discontinued after 10 minutes of bolus, even if after they would remain stable until the end of the fMRI session. Therefore, it was attempted to have isoflurane at 0% only after 20 minutes of bolus in two mice. However, since the same phenomenon continued to happen, a new protocol was defined for the remaining animals, which is shown in Figure 2.7.

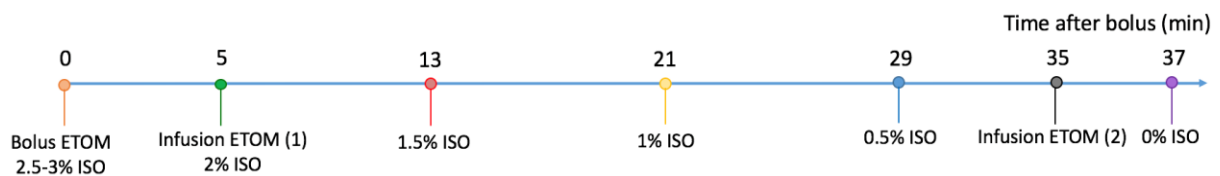


Figure 2.7 – Timeline showing the variations in isoflurane (ISO) and etomidate (ETOM) after bolus of etomidate. (1) represents the constant infusion of 0.6 mg/kg/min, while (2) represents the time at which mice were divided into different concentration groups.

After 3 hours of bolus, mice were removed from the animal bed and placed inside a cage with a heating pad below in order to prevent hypothermia until they were completely recovered from anaesthesia.

2.3. Setup for Delivery of Complex Visual Stimuli

An innovative visual stimulation system for preclinical fMRI of the visual system of mice and capable of delivering a wide variety of accurate and complex visual stimuli was developed. The hardware that was required to build this system and the preparation of the setup for the delivery of moving bar stimuli are described in the following subsections.

2.3.1. Equipment

The confined space of a small animal scanner makes it difficult to position any kind of screen or mirrors that can effectively project light visual stimuli towards the animals' eyes. The largest resonator

that was available for mice in this project has only 86 mm of inner diameter, which, linked to the fact that the eyes of the mice are laterally positioned in the head, makes it difficult to place a screen in front of an eye at a distance that is enough for it to minimally focus in response to a complex visual stimulus.

Keeping the reasoning of the setup described in Subsection 2.1.1, multiple fibre-coupled LED sources controlled by multiple LED drivers can constitute a good solution if one wants to create a system that allows motion stimuli presentation, which, in fact, has already been done once [114]. The only shortcoming of this approach is, however, its price. If one wanted to build for example a 4x4 matrix of monochromatic lights of that kind, the whole system could cost almost up to ten thousand euros. A low-cost MRI safe alternative that offers several advantages in comparison to that setup is the use of an organic light emitting diode (OLED) flat display. The 0.95-inch OLED display module with a 96 x 64 dots matrix and 16-bit colour depth (PGO095F9664N01M, Panox Display, Hong Kong) was chosen for that purpose. Besides being a low-power device, this small display allows independent control of each of its 6144 pixels which can assume more than 65 thousand different colours and does not contain ferromagnetic metals, which are forbidden in the scanner room because they can be strongly projected towards the magnet bore due to the magnetic pull exerted by the magnetic field on this type of material. Moreover, together with its breakout module (POB095SPI22W, Panox Display, Hong Kong), with which it communicates via a 4-wire write-only serial peripheral interface (SPI), it only costs a dozen of euros.

The OLED was connected to its breakout module through a 1.5 m cable that was properly isolated with layers of a fine metal mesh so that the OLED circuitry did not suffer from induced currents from gradients field, avoiding therefore any interference on image acquisition or contamination of the visual patterns presented by the OLED. Synchronization with the MRI scanner protocol and accurate control of the stimulus presentation were in this case accomplished through an Arduino Due microcontroller (Arduino, United States of America) for trigger detection and OLED control. The pulse sequences used for imaging were programmed in the scanner operator console to send two different TTL signals at specific time points chosen by the user, that could be detected by the Arduino.

During rest, the optical axis of the mouse is spontaneously directed 64° lateral to the mid-sagittal plane and 22° superior to the horizon [131]. In order to guarantee that the display would always be placed in the same position across experiments, i.e. at approximately 2.5 cm from the left eye, and that the optical axis of the mouse intercepted the screen in the middle of the field of view to be used (a 64 x 64 pixel square region in the right part of the screen), a 3-D printed custom piece was designed in Autodesk Fusion 360 software for students, as it can be seen in Figure 2.8. This distance was estimated by placing three sedated mice in the bed and measuring the distance from their eyes to some key points of the bed, allowing to model their usual position in relation to the bed and to the screen.

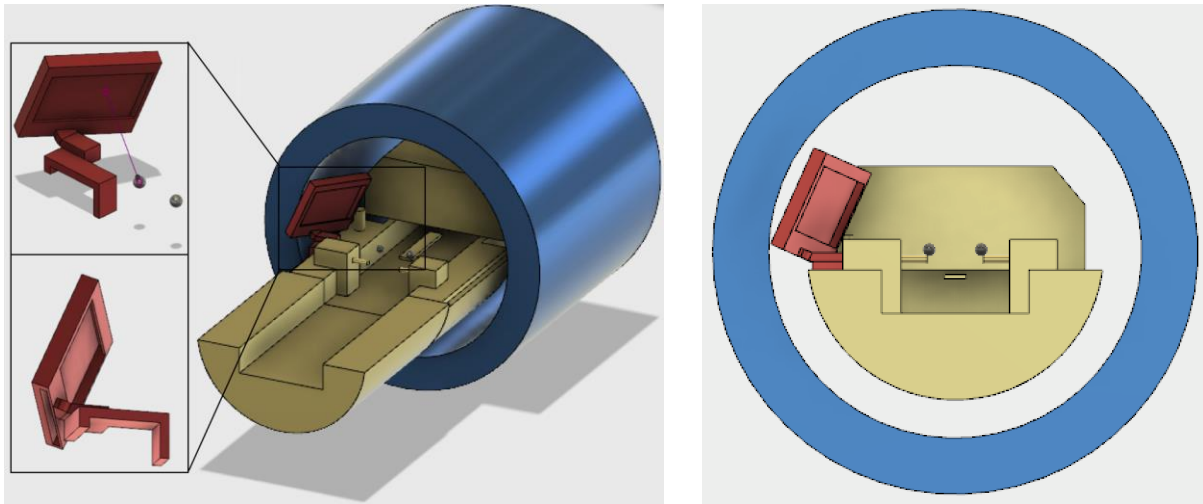


Figure 2.8 – 3-D models of the bed, resonator, eyes and piece designed for accurate positioning of the OLED display across experiments. (Left) Close-up view of the piece (red) in two different perspectives and its position relative to the mouse's eyes (gray spheres). The 86 mm inner diameter resonator is represented in blue and the bed is represented in yellow. (Right) Same components as in (Left) but viewed from a different perspective.

The entire system with all of its components assembled together is shown in Figure 2.9.

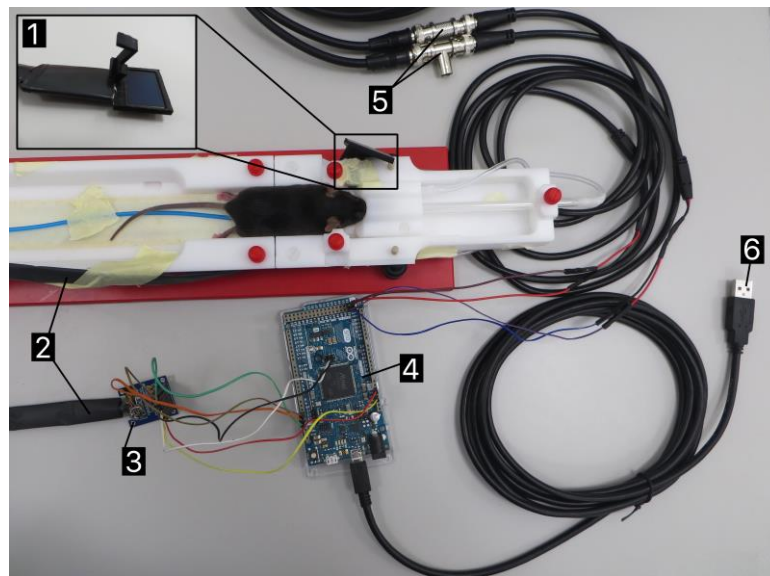


Figure 2.9 – Experimental setup for visual pathway mapping in the mouse, with all the elements that are essential for the delivery of complex visual stimuli. (1) OLED display inserted in the 3-D modelled piece that attaches to the bed, (2) 1.5 m cable that is used to put all electronic components away from the inside of the scanner bore, (3) OLED breakout module, (4) Arduino Due microcontroller, (5) Cables and connectors used to allow the reception of 2 TTL trigger signals from the scanner. A tee connector is used in one of these two connections to also allow the physiological monitoring gating system to record when fMRI data acquisition is occurring, (6) Cable that connects the Arduino to the computer.

In order to calculate how many degrees of the visual field were covered by the screen's FOV, the Cartesian coordinates of the screen were converted to spherical coordinates, as it is displayed in Figure B.1. Each pixel spans less than 0.5° of the visual field in each direction, and the total FOV

covers $\sim 30^\circ \times 30^\circ$ of the visual field. Therefore, the portion of the visual field subtended by the screen was estimated to be approximately $49^\circ - 79^\circ$ azimuth and $7^\circ - 37^\circ$ elevation relative to the mid-sagittal plane and the horizon, respectively.

2.3.2. Preparation of the setup for monocular visual stimuli delivery

Once the setup had been assembled, the OLED was programmed to present moving bars of different speeds along the temporal-nasal and upward-downward directions to the left eye of the mouse. Although the screen is placed uniquely in the left visual field, reflective surfaces within the scanner can allow the right eye to also receive some light from the moving stimulus. In order to avoid light leaking into the right eye of the animal, a 3-D eye patch was modelled, printed and placed above the right eye of the animal, as it is shown in Figure 2.10.

When monitors are flat, such as the screen adopted in this study, the size (in $^\circ$) and speed (in $^\circ/s$) of drifting bars can become gradually reduced for larger eccentricities of the stimulus when the drifting bar is kept constant in its width (in pixels or mm) and speed (in pixels/s or mm/s). If the stimulus covers a large region of the visual space, this distortion can become quite substantial, requiring spherical stimulus correction [9]. However, considering that the screen used in this case is small and that the eccentricity is kept at a low value ($\sim 15^\circ$ of visual angle from the centre point of the screen), the distortion is not significant and does not call for any correction.

The Arduino was programmed to receive two different TTL signals from the scanner: one to trigger rest periods, in which a static vertical or horizontal bar in the OLED is kept on as long as the trigger is being received, and another to trigger stimulation periods, i.e. periods of motion of the bar. Therefore, if a block design paradigm is to be used, the Arduino is programmed to light up a bar at a random position of the screen in the first rest period, promote its back-and-forth movement along the screen in the stimulation periods, and keep the last bar than was on at end of each stimulation period as the static bar that is on in the subsequent rest period, in order to prevent abrupt discontinuities in the bar position during the functional run. Moreover, different speeds can be produced by changing bar on-off intervals.



Figure 2.10 – Mouse viewing a moving bar stimulus. (*Left*) Mouse viewing the screen with its left eye, while its right eye is covered with an eye patch. (*Middle*) Visual stimulation of the left eye with a vertical bar moving across the screen. A loop surface coil is placed above the head for RF signal reception and is connected to its preamplifier. (*Right*) Animal bed and screen inserted in the 86 mm inner diameter volume coil used for RF signal transmission.

3

Results

In this chapter, the most important results of the BOLD fMRI visual stimulation experiments are presented to the reader, as well as the results of the attempt to decrease the dosage of the anaesthetic under study.

3.1. Visual Stimulation fMRI Experiments

The first results presented in this thesis involve three types of visual stimulation experiments aiming to validate the use of subcutaneous etomidate on mouse BOLD-fMRI experiments, with intentions to replace the use of medetomidine.

First, quality of raw fMRI data from all experiments is evaluated. Results from single animals and from all animals grouped together are given, and physiological stability plots and some statements about the recovery capability of the mice are then presented. Results from subjects which were discarded from group analysis are also shown. Finally, statistical parametric maps of BOLD in the brain and BOLD signal timecourses in specific ROIs are given for each of the three experiments.

3.1.1. Quality control and representative fMRI results

Figure 3.1 shows the raw anatomical images from one representative mouse. These are characterized by having quite high-resolution, excellent SNR and almost no distortions.

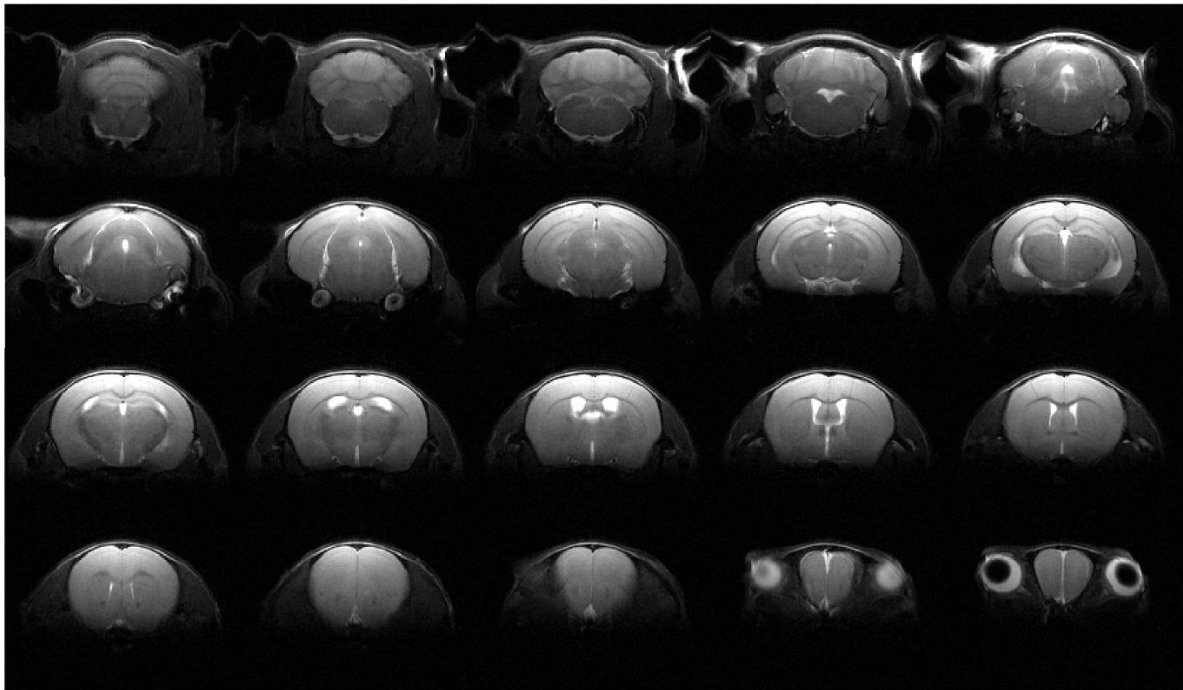


Figure 3.1 – Raw anatomical images from one representative mouse. Slices are presented from the caudal part to the rostral part of the brain (from left to right and top to bottom in the figure). The “cut” in the bottom of the brain is due to the FOV saturation pulses.

Functional images cannot be expected to have the same quality of anatomical scans, but EPI sequences in this study performed quite well. Figure 3.2 shows representative images of raw fMRI data, and demonstrates relatively high SNR and relatively few distortions for an EPI sequence at 9.4T. A few cortical regions evidence signal losses in these images (white arrows) due to susceptibility effects, and slightly higher signals were observed in the dorsal parts of the brain in comparison to the

lower regions due to the larger distance from the ventral regions to the loop coil used for signal reception. Nevertheless, raw functional data were reliable and robust across runs and animals, showing a high and reproducible SNR of 35.6 ± 6.2 (mean \pm standard deviation), even at the high spatial and temporal resolution they were acquired with.

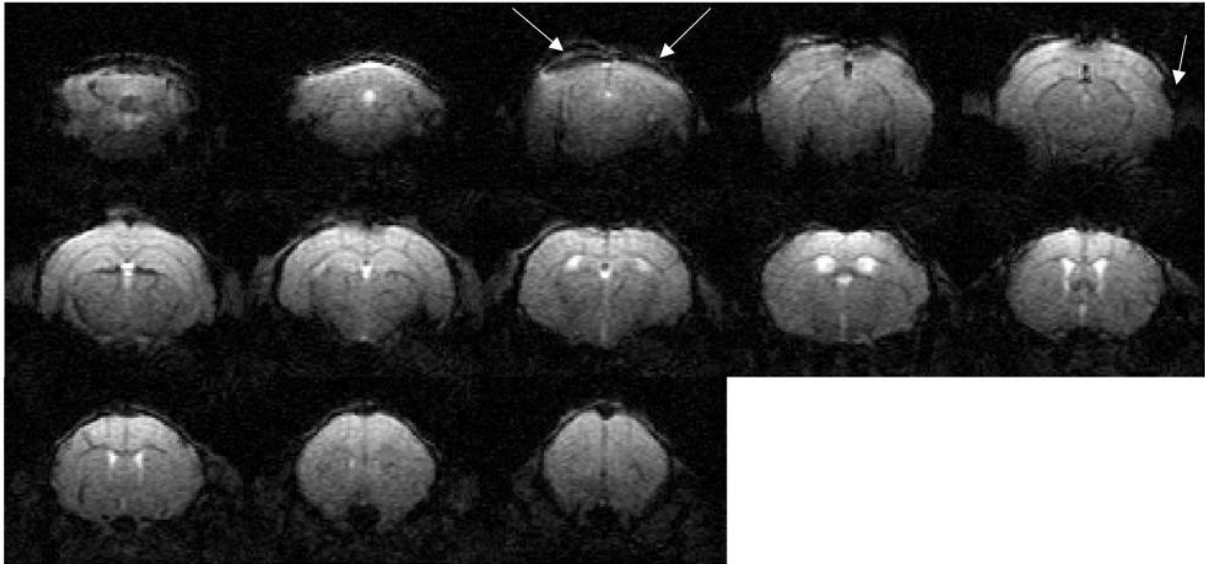


Figure 3.2 – Raw functional images (from one frame on a single run) from one representative mouse. Slices are presented from the caudal part to the rostral part of the brain (from left to right and top to bottom in the figure). White arrows point to regions of the brain with signal losses.

As described in Subsection 2.1.5, in the fMRI experiments, some repetitions had to be corrected due to signal fluctuations, as depicted for one brain slice in Figure 3.3, which plots the signal evolution over time (columns) in the slice (all voxels plotted in one row). Some outlier columns can be identified in the voxels' timecourse map shown in Figure 3.3 (black arrows), suggesting that signal intensity from all voxels within the slice had momentarily fluctuated. The time points associated with these fluctuations correspond to the time points at which the average signal in the brain largely deviates from a fitted (low order) polynomial curve. Moreover, the occurrence of these outliers in the data is random in time and not correlated in any way to specific visual stimulation or rest epochs.

Therefore, during preprocessing, when such outliers were identified, the intensity of the entire set of voxels from those slice frames was replaced with data interpolated using cubic splines. An example of the resulting timecourses after correction is shown in Figure 3.4. Clearly, the large fluctuations in voxel intensity have been almost completely removed from the data.

This step was indeed very important, as some previously significant responses in non-visual related regions of the brain disappeared from the statistical parametric maps at the defined thresholds for significance, without removing clusters of activation in vision associated areas, as exemplified in Figure 3.5.

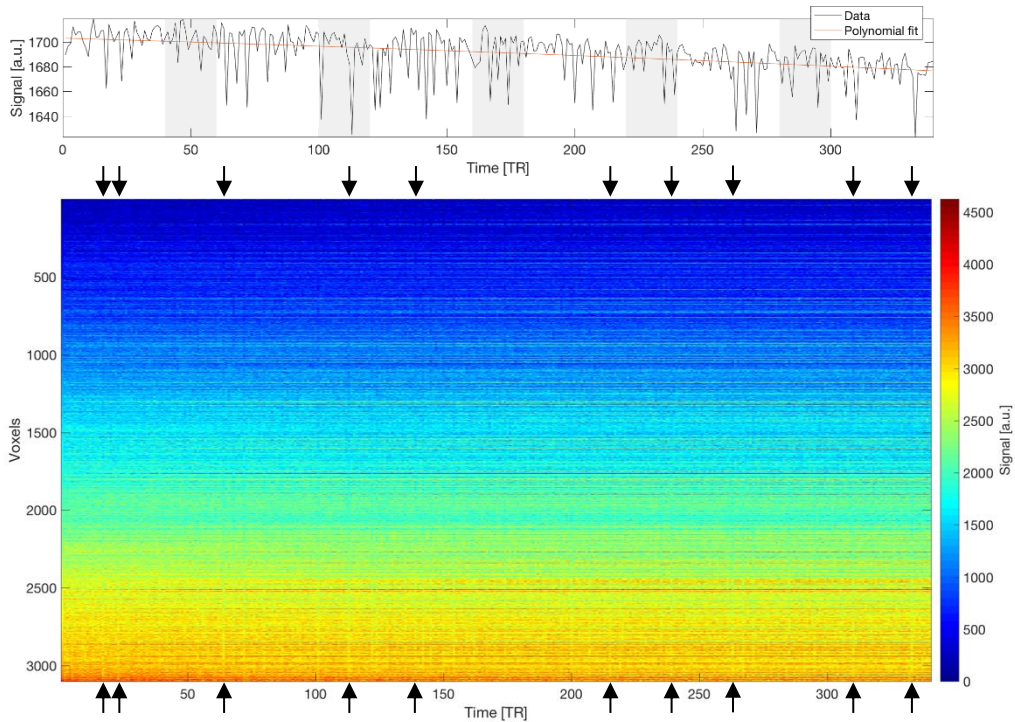


Figure 3.3 – Raw signal timecourses in one brain slice before corrections. (*Top*) Average signal timecourse in one brain slice before correction, and the 2nd degree polynomial that was fitted to it. Grey shaded regions represent 20 s stimulation periods. (*Bottom*) 2-D map of every time series within a brain slice, where rows represent each brain voxel's timecourse before correction, columns represent each frame and colours represent intensity. Vertical black arrows are pointing to signal fluctuations.

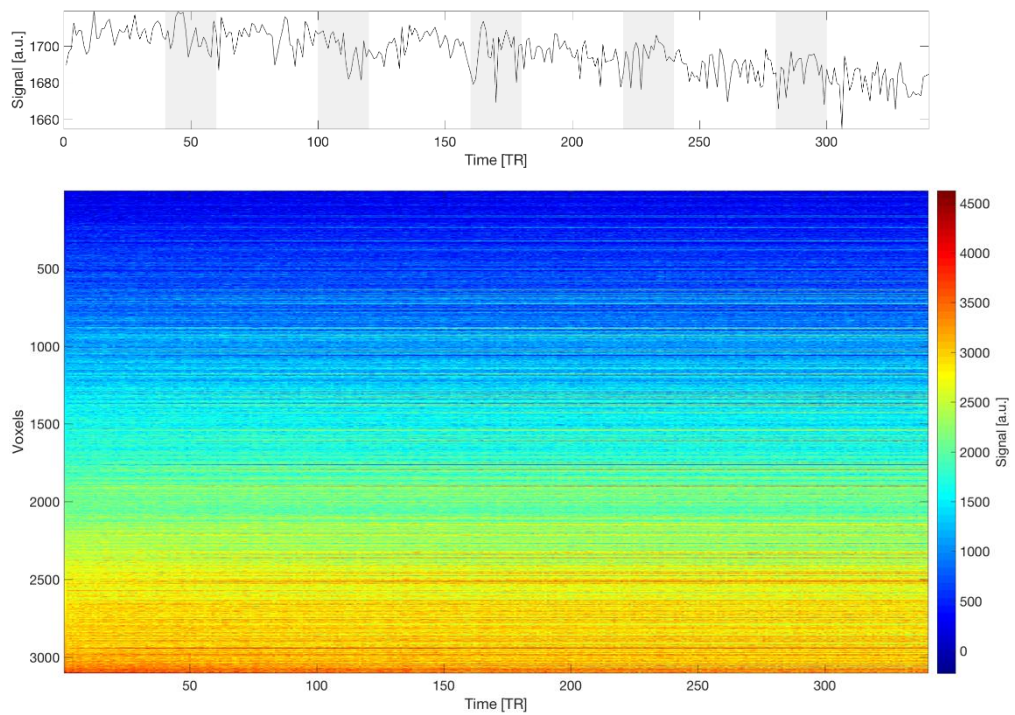


Figure 3.4 – Idem to Figure 3.3, but for corrected timecourses.

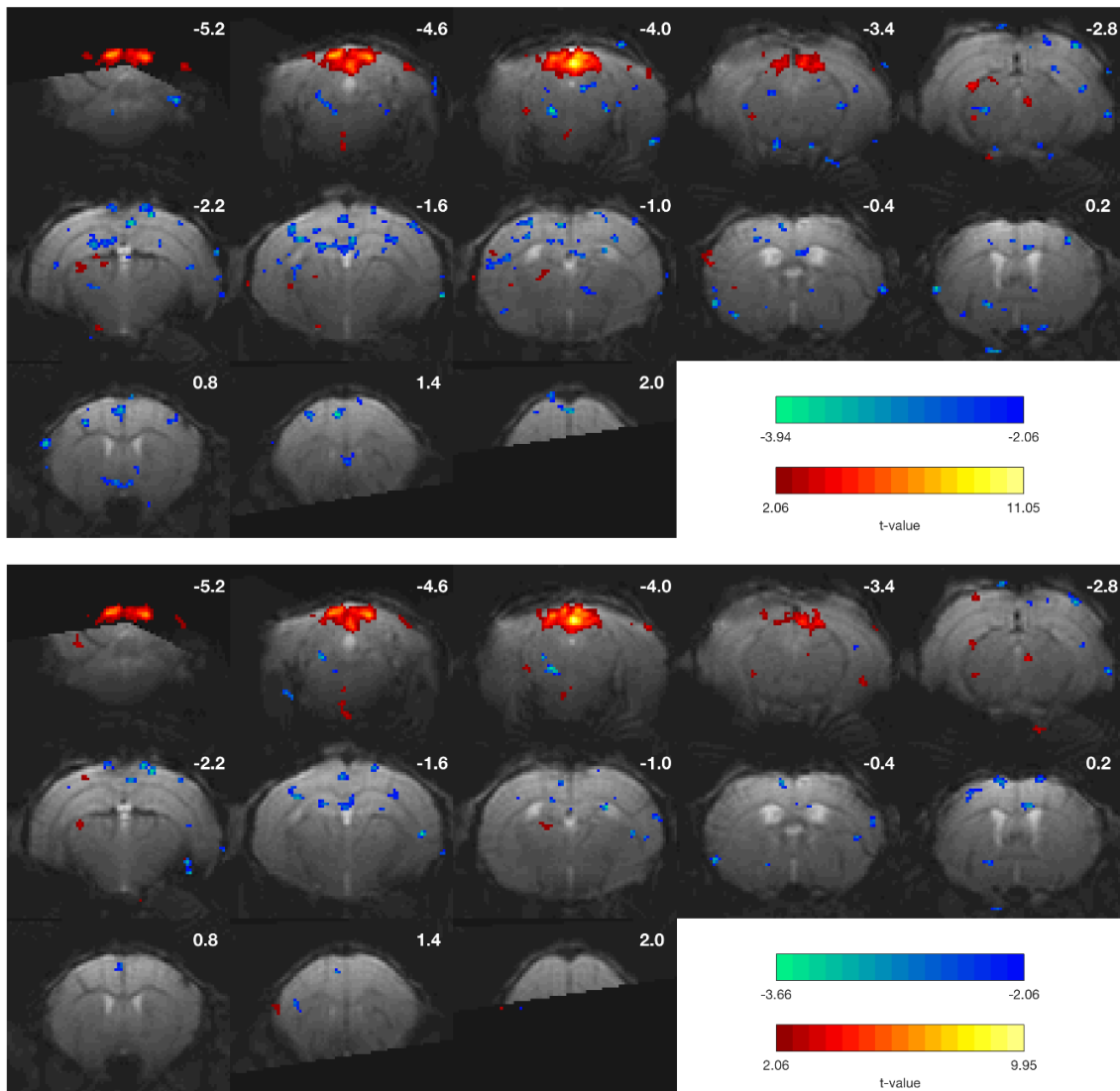


Figure 3.5 – Brain maps of significant ($p < 0.02$, minimum cluster size = 8) BOLD activation to binocular visual stimulation with 2 Hz flashing frequency and $8.1 \times 10^{-1} \text{ W/m}^2$ of light intensity in consecutive coronal slices from a single run of a representative mouse, without performing corrections at the slice level (*Top*) and after interpolating some frames of each slices for correction of outliers (*Bottom*). Approximate distances from Bregma are indicated in each slice. The most rostral and caudal image slices are cut as a result of realignment, coregistration and normalization.

Clear BOLD responses were observed in ROIs placed in relevant regions along the visual pathway with the naked eye in single runs, even before averaging on the multiple runs or on different animals (Figure 3.6). Despite the constant presence of high-frequency noise and the appearance of relatively low frequency oscillations uncorrelated with the stimulus paradigm (cf. for example, in V1), BOLD signals in the SC, LGN and V1 evidenced clear signal changes during stimulation periods, which resulted in a clear differentiation between rest and stimulation periods also in the averaged cycle plots. Furthermore, activation peaks were sometimes noticed at the beginning and ending of stimulation, and in some cases, a post-stimulus undershoot could also be detected.

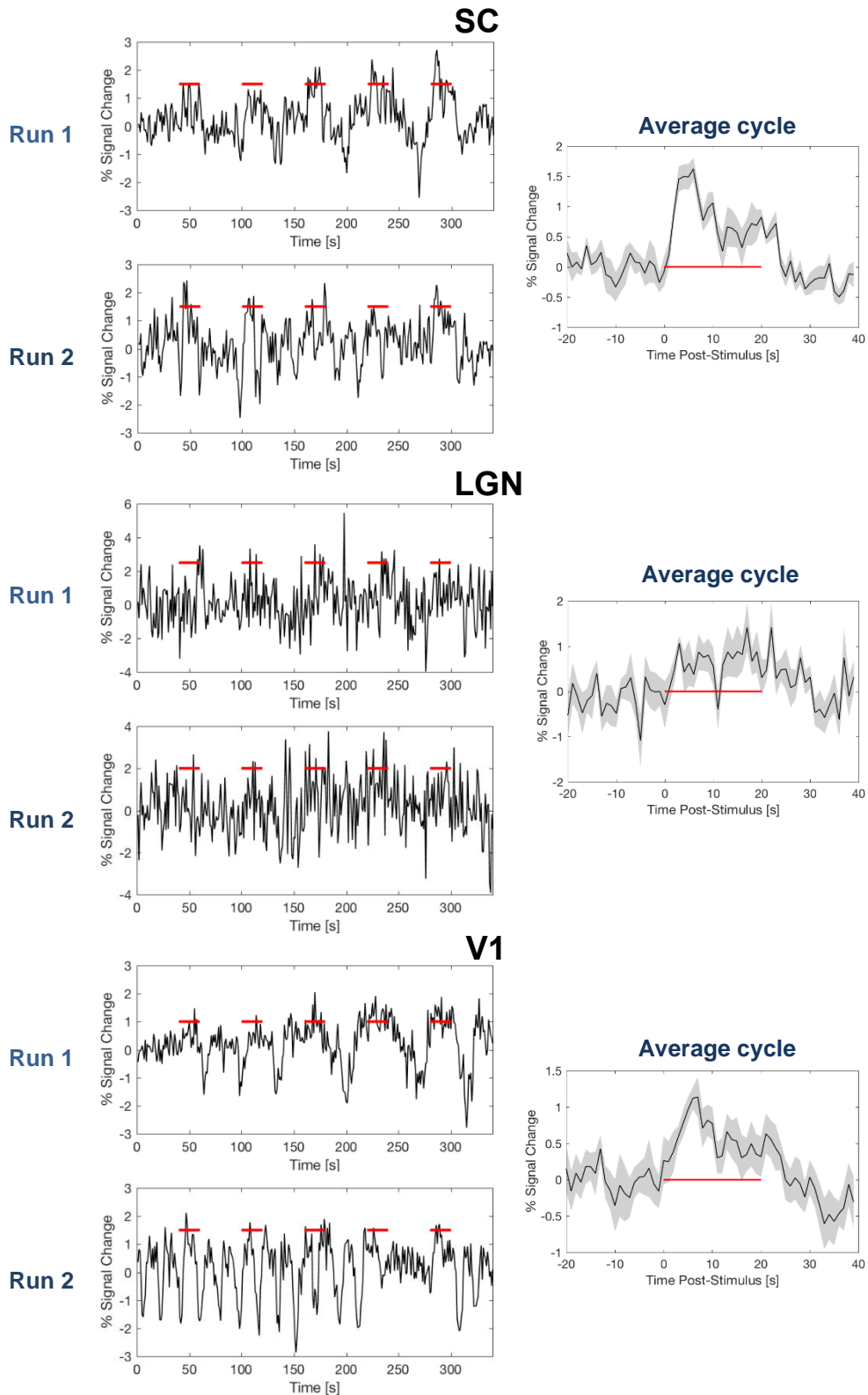


Figure 3.6 – Uncorrected BOLD signals in the SC, LGN and V1 of a single mouse in response to binocular visual stimulation with 2 Hz flashing frequency and $9.2 \times 10^{-2} \text{ W/m}^2$ of light intensity. Plots on the left represent ROI's timecourses in single runs with five stimulus epochs, while each timecourse on the right represents the average cycle of the BOLD response computed from the corresponding 2 runs on the left and is plotted as mean percentage of signal change (solid line) \pm standard error of the mean (shaded region). The red bars indicate 20 s stimulation periods.

After averaging all BOLD signal timecourses for identical stimulus conditions across animals, BOLD responses became easier to detect in all ROIs following stimulation, as exemplified in Figure 3.7.

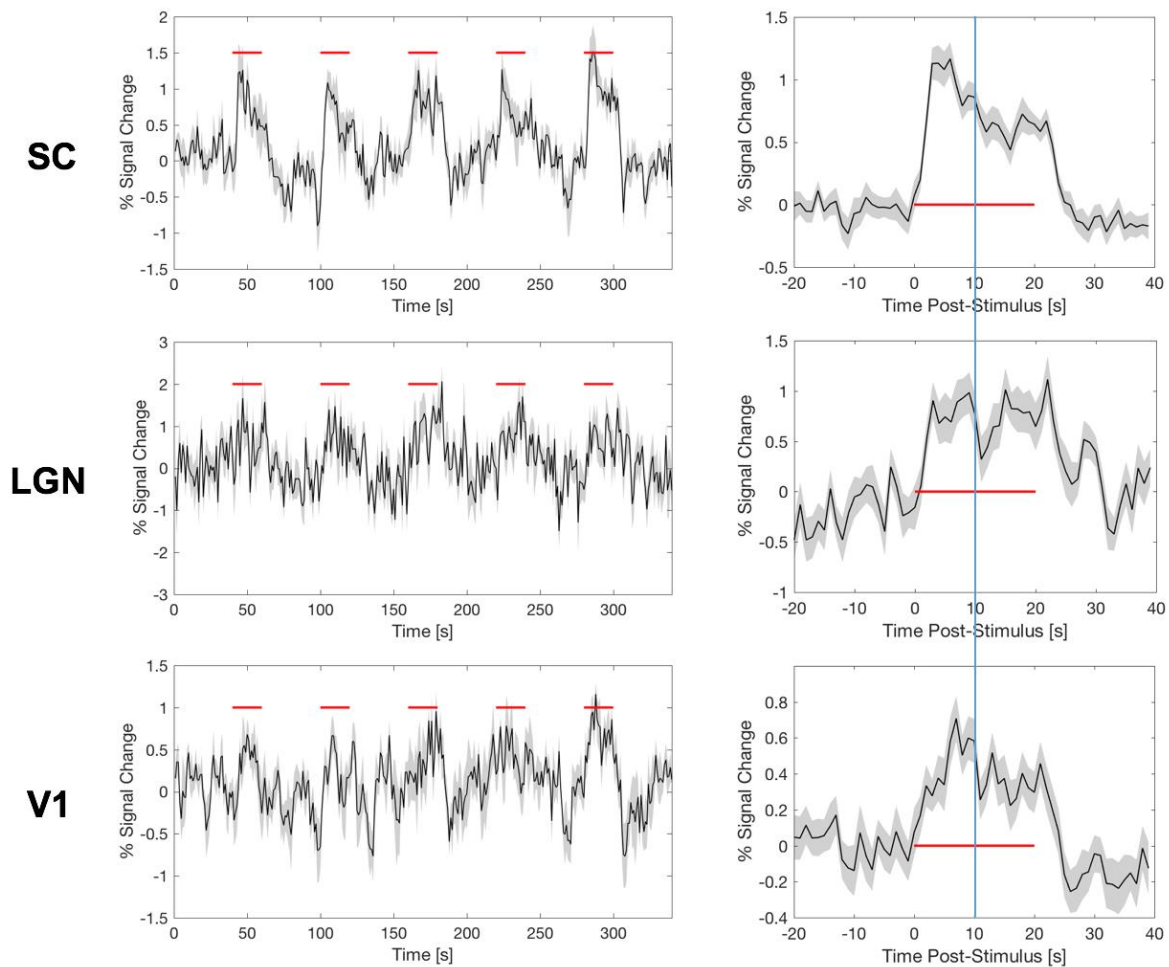


Figure 3.7 – Idem to Figure 3.6, only now the plots are averaged over 3 animals ($n = 6$ runs). A vertical line is drawn in the average cycle plots to guide the eye at 10 s from the beginning of stimulation.

Figure 3.8 shows the BOLD response map measured from one representative animal for one visual stimulus condition. Structures activated include the SC, V1 and LGN of the brain. However, in single subject maps, small clusters of activation are also frequently found in other brain regions that are not known to be functionally related to the visual pathway. In particular, significant negative BOLD responses are detected in the most anterior slices from the animal represented in this figure, and, according to the mouse atlas, are concentrated in the primary motor cortex. However, besides not having detected any kind of movement throughout the specific run at which these responses were recorded, similar clusters are not found neither in the brain map from the other run in which this mouse was subjected to the same stimulus condition, nor in brain maps from similar runs in other animals.

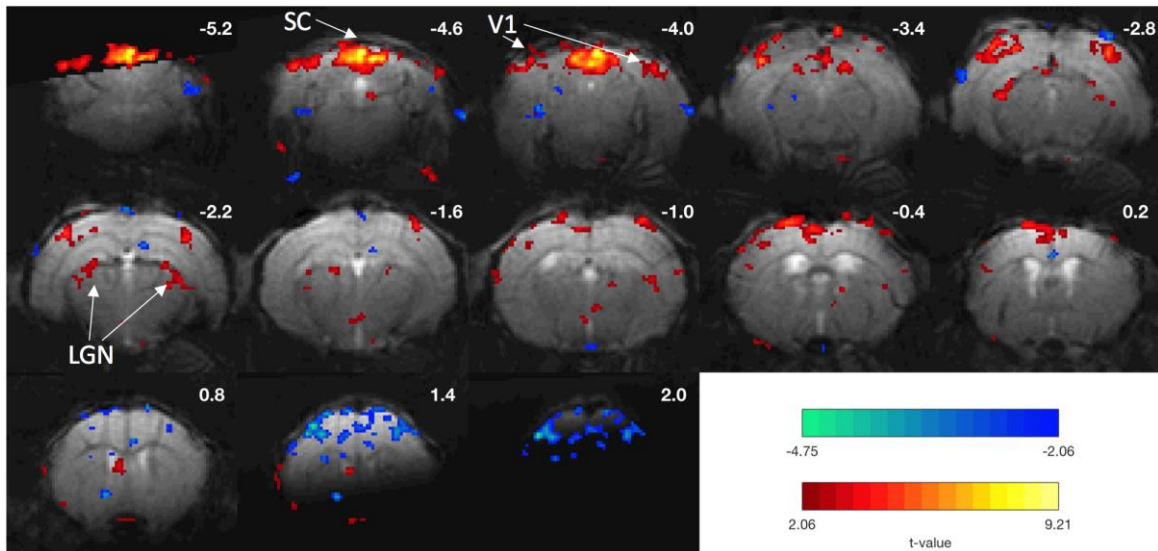


Figure 3.8 – Brain map of significant ($p < 0.02$, minimum cluster size = 8) BOLD activation to binocular visual stimulation with 2 Hz flashing frequency and $9.2 \times 10^{-2} \text{ W/m}^2$ of light intensity in consecutive coronal slices from a representative mouse ($n = 2$ runs). Approximate distances from Bregma are indicated in each slice. The most rostral and caudal image slices are cut as a result of realignment, coregistration and normalization. SC, LGN and V1 are labelled.

Therefore, group-level brain maps were built to find which voxels show the most significant activation across experiments. Figure 3.9 shows the group-level map obtained for the same stimulus condition as in Figure 3.8.

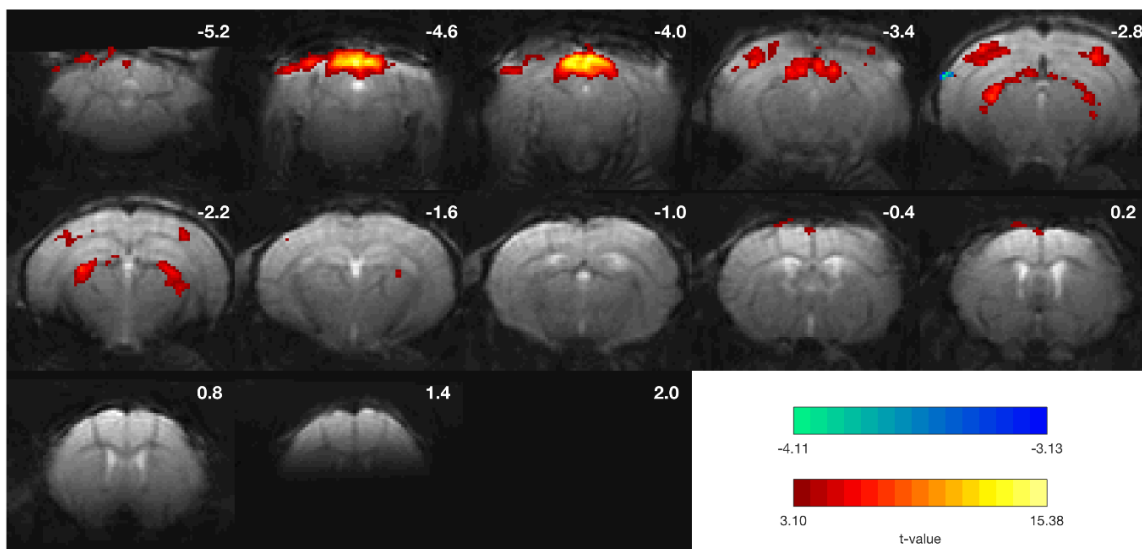


Figure 3.9 – Brain map of significant ($p < 0.001$, minimum cluster size = 8) BOLD activation to binocular visual stimulation with 2 Hz flashing frequency and $9.2 \times 10^{-2} \text{ W/m}^2$ of light intensity in consecutive coronal slices from an average of 3 mice ($n = 6$ runs). Approximate distances from Bregma are indicated in each slice. The most rostral image slices are cut as a result of realignment, coregistration and normalization.

Clusters of activation can still be observed in the SC, LGN and V1 with high statistical significance. However, voxels in brain regions not associated with vision that appeared active in some single subject maps were eliminated in the group analysis.

3.1.2. Experiment 1: BOLD responses to different light intensities under etomidate

Although the physiological parameters of all mice used in Experiment 1 were stable during the entire experimental session (Figure 3.10), with a mean \pm standard deviation of 109 ± 13 breaths/min and 34.9 ± 1.4 °C across all mice, the 1st and 3rd mice that were used died within one day following the experiments. This was most probably caused by the administration of etomidate. The other two mice, on the other hand, returned to their normal state within some hours after the experiment.

It should be noted that temperature values rapidly decreased to values outside the normal physiological range after anaesthesia induction, starting to increase at a slower pace back to normal values just before the beginning of functional runs.

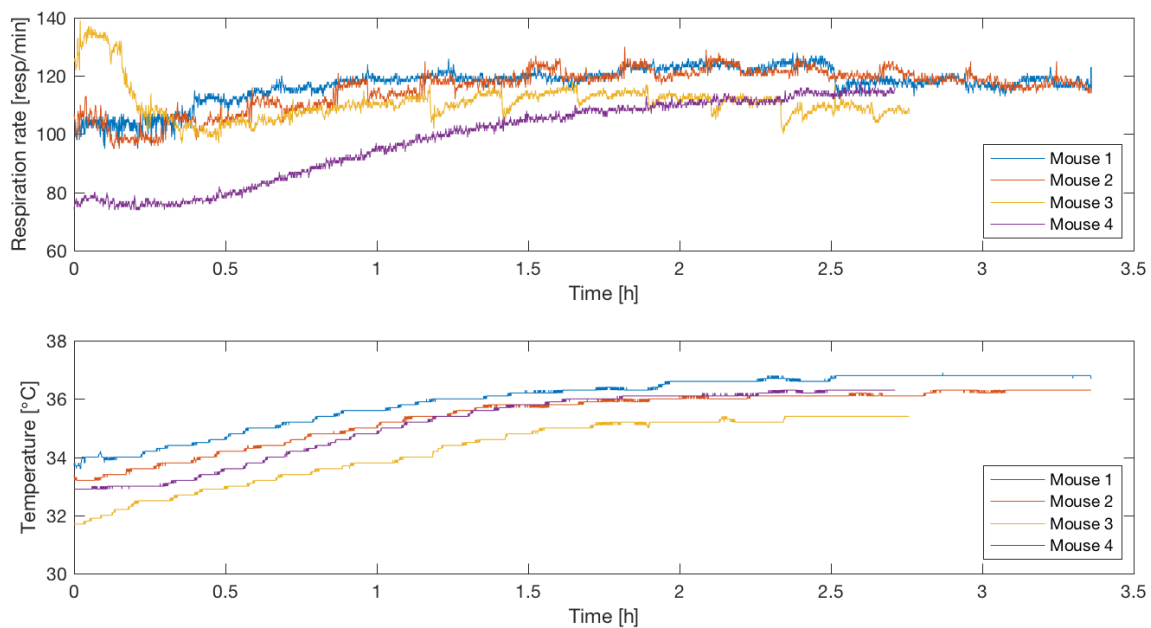


Figure 3.10 – Respiration rate (in respirations per minute) and temperature (in °C) plots for all mice used in Experiment 1, from the time that functional acquisition started until the end of the session.

Moreover, the 3rd mouse revealed almost no response to the stimuli in the visual pathway. Figure 3.11 and Figure 3.12 present the brain map of significant BOLD activation and the average cycle of the BOLD response in ROIs along the pathway, respectively, following binocular visual stimulation with 2 Hz flickering frequency and 8.1×10^{-1} W/m² of light intensity. This stimulus condition is in the set of stimuli that were expected to trigger stronger BOLD responses in these regions. However, it can be seen that, although a slight activation is seen in the SC in the beginning and end of stimulation, responses in the visual system were almost inexistent. Moreover, responses to other stimulus

conditions are equally poor along the pathway. Therefore, the data from this mouse was discarded from the group analysis. It should also be noted that this mouse was the one that died in the shortest time after the experiment, i.e. between 1 and 2 hours after the session had ended.

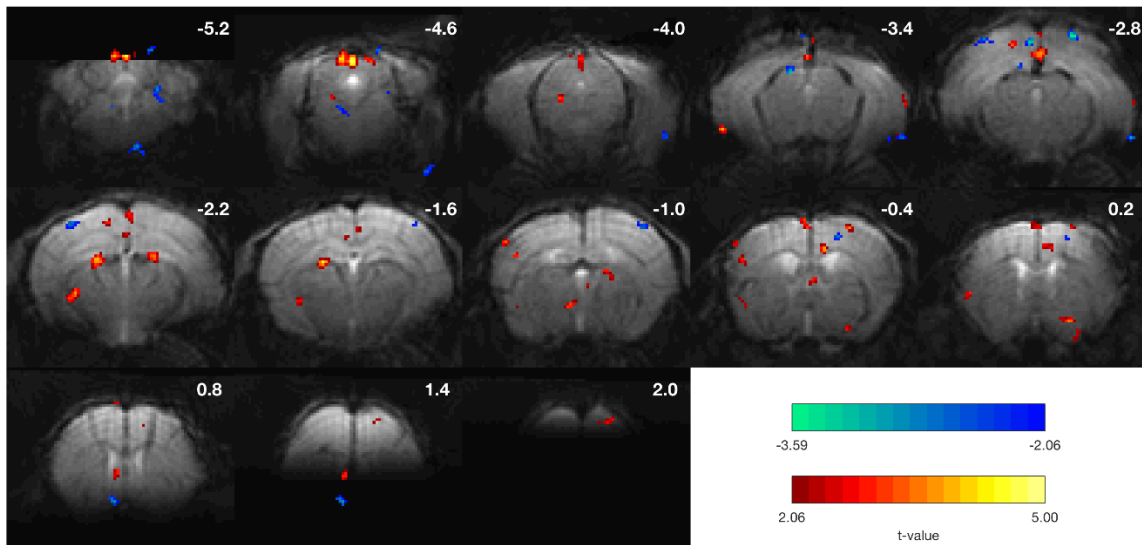


Figure 3.11 – Brain map of significant ($p < 0.02$, minimum cluster size = 8) BOLD activation to binocular visual stimulation with 2 Hz flashing frequency and $8.1 \times 10^{-1} \text{ W/m}^2$ of light intensity in consecutive coronal slices from the 3rd mouse used in Experiment 1 ($n = 2$ runs). Approximate distances from Bregma are indicated in each slice. The most rostral and caudal image slices are cut as a result of realignment, coregistration and normalization.

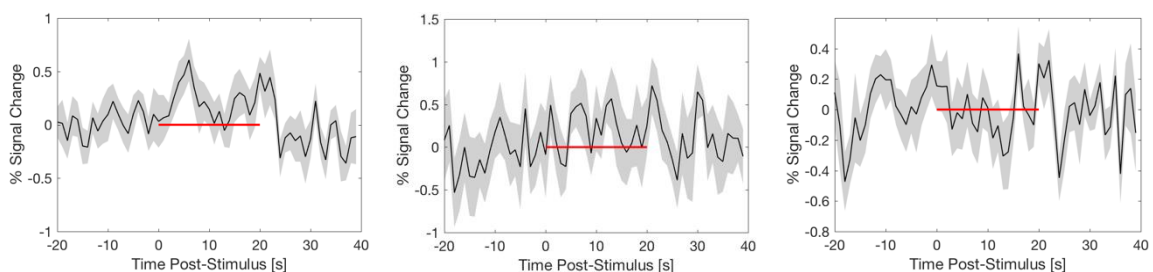


Figure 3.12 – Average cycle of the BOLD response to binocular visual stimulation with 2 Hz flashing frequency and $8.1 \times 10^{-1} \text{ W/m}^2$ of light intensity in the SC (*Left*), LGN (*Middle*) and V1 (*Right*) of the 3rd mouse used in Experiment 1 ($n = 2$ runs), plotted as mean percentage of signal change (solid line) \pm standard error of the mean (shaded region). The red bars indicate one 20 s stimulation period.

The group-level maps for each light intensity ($9.2 \times 10^{-3} \text{ W/m}^2$, $9.2 \times 10^{-2} \text{ W/m}^2$ and $8.1 \times 10^{-1} \text{ W/m}^2$) are shown in Figure 3.13 for 2 Hz of flickering frequency, and in Figure 3.14 for 10 Hz stimuli. Since responses are mainly concentrated in 6 slices, the other 7 slices are not shown. Bilateral BOLD responses to the stimuli were clearly observed in the SC, V1 and LGN at all intensities, though with different significance levels.

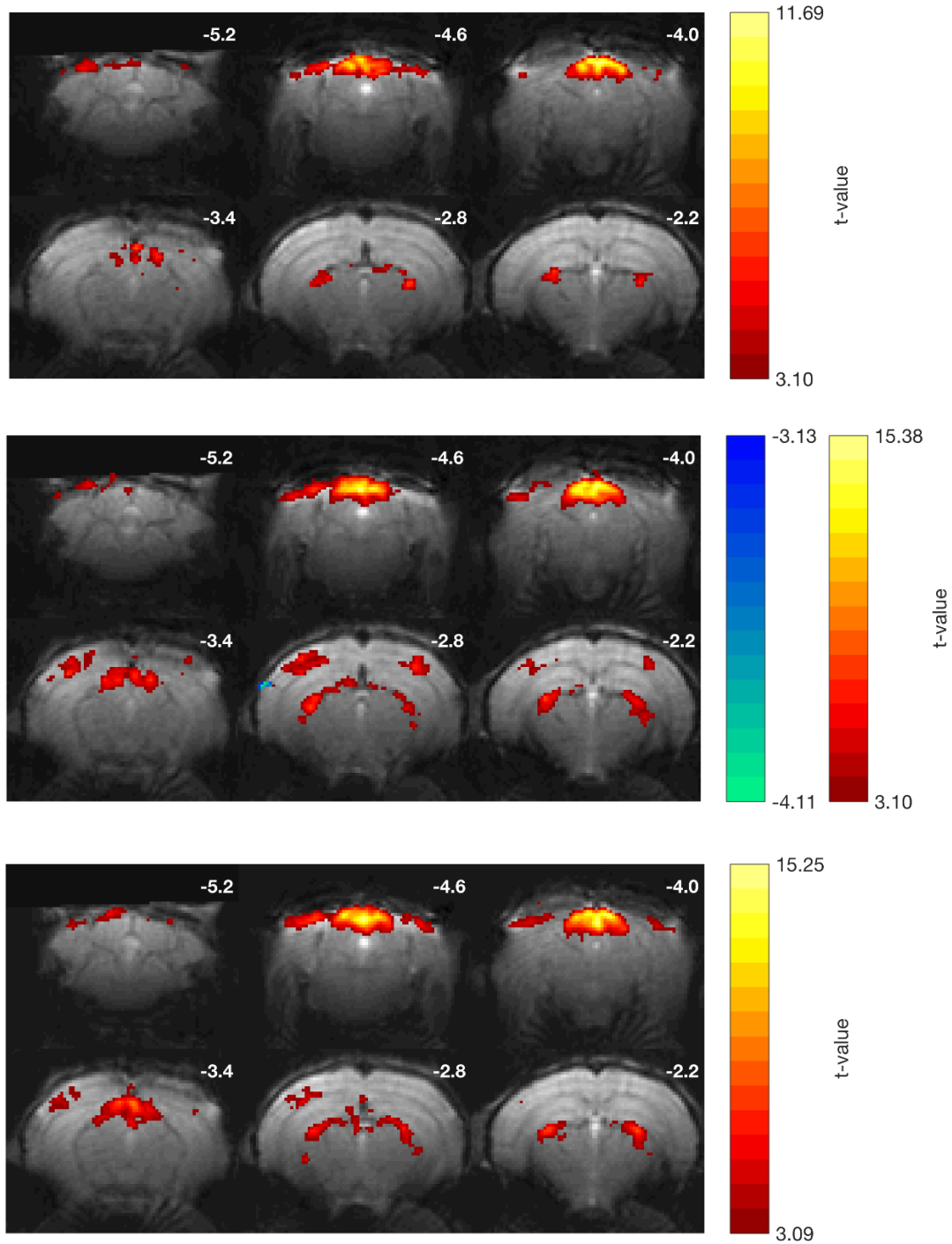


Figure 3.13 – Brain maps of significant ($p < 0.001$, minimum cluster size = 8) BOLD activation to binocular visual stimulation with 2 Hz flashing frequency and $9.2 \times 10^{-3} \text{ W/m}^2$ (Top), $9.2 \times 10^{-2} \text{ W/m}^2$ (Middle) or $8.1 \times 10^{-1} \text{ W/m}^2$ (Bottom) of light intensity in consecutive coronal slices from an average of 3 mice ($n = 6$ runs). Approximate distances from Bregma are indicated in each slice.

Significant SC responses are observed in slices 2-4 at all intensities for both frequencies, with the higher t -value voxels located in the more dorsal layers. Moreover, the t -values and the number of responsive voxels appear to increase with intensity, especially at the 10 Hz flickering frequency. Significant LGN responses are mainly found in slices 5 and 6 in both hemispheres. Similar to the SC, the size of the LGN clusters slightly increases with increasing intensity. Highly significant BOLD

responses were also detected in V1 in every run for all animals, although the number of slices occupied by active V1 varied between different runs and light intensities. Moreover, clear bilateral negative BOLD responses were found in the cortex at 10 Hz for all intensities, while responses at 2 Hz were positive.

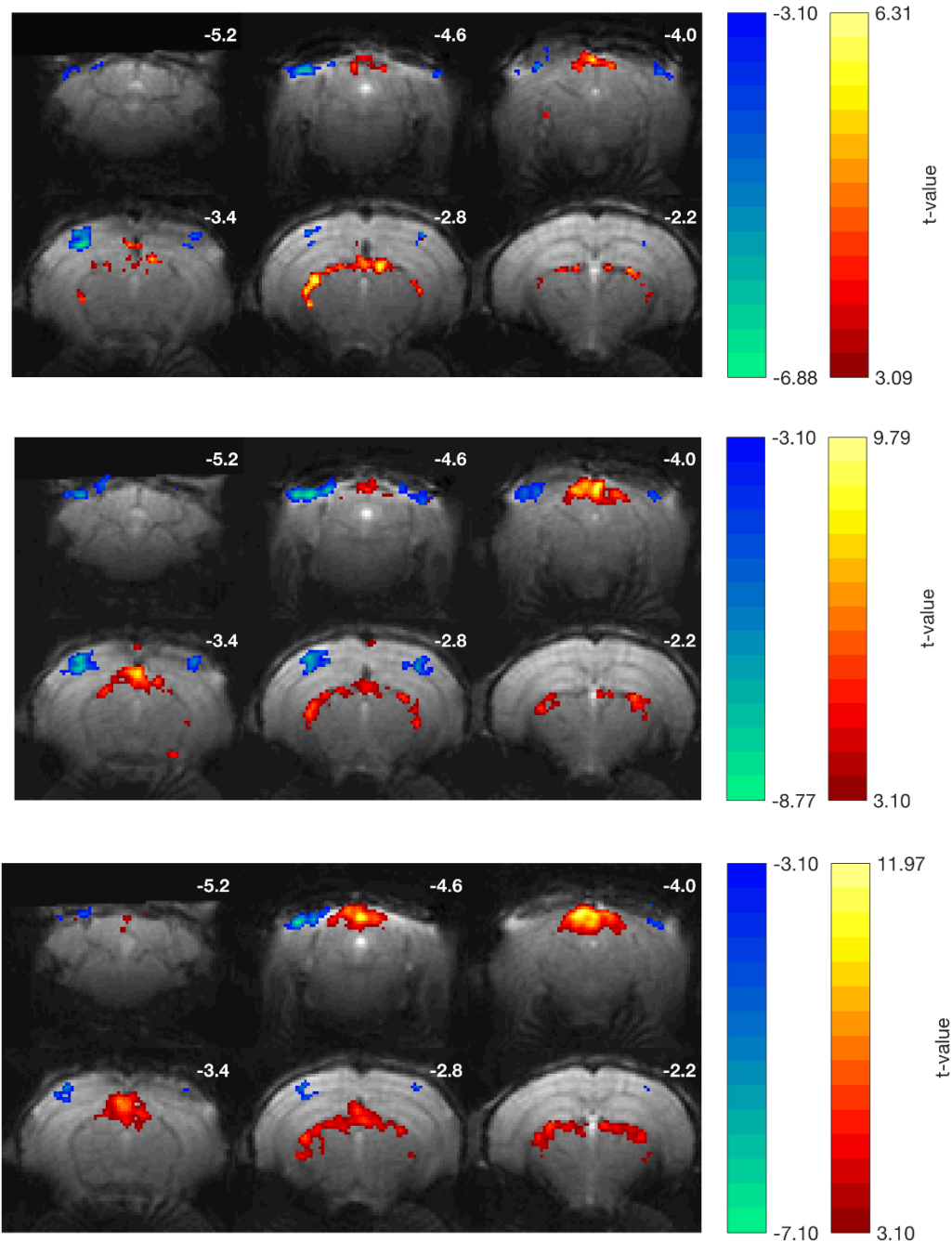


Figure 3.14 – Brain maps of significant ($p < 0.001$, minimum cluster size = 8) BOLD activation to binocular visual stimulation with 10 Hz flashing frequency and $9.2 \times 10^{-3} \text{ W/m}^2$ (Top), $9.2 \times 10^{-2} \text{ W/m}^2$ (Middle) or $8.1 \times 10^{-1} \text{ W/m}^2$ (Bottom) of light intensity in consecutive coronal slices from an average of 3 mice ($n = 6$ runs). Approximate distances from Bregma are indicated in each slice.

To more easily compare these results, the average BOLD response amplitudes for each stimulus condition are shown in Figure 3.15. Smaller peak BOLD amplitudes are detected in the SC and LGN

for the lowest light intensity used ($9.2 \times 10^{-3} \text{ W/m}^2$) in comparison to the highest intensities, either for 2 Hz or 10 Hz flashing stimuli. Moreover, although a significant difference between the maximum amplitudes registered in the SC and LGN for all stimulus conditions was not observed, responses detected in V1 reach lower percent signal change values in comparison to the other two structures of the visual pathway. Moreover, in accordance to the maps presented in Figure 3.14, negative BOLD responses are found in V1 at 10 Hz.

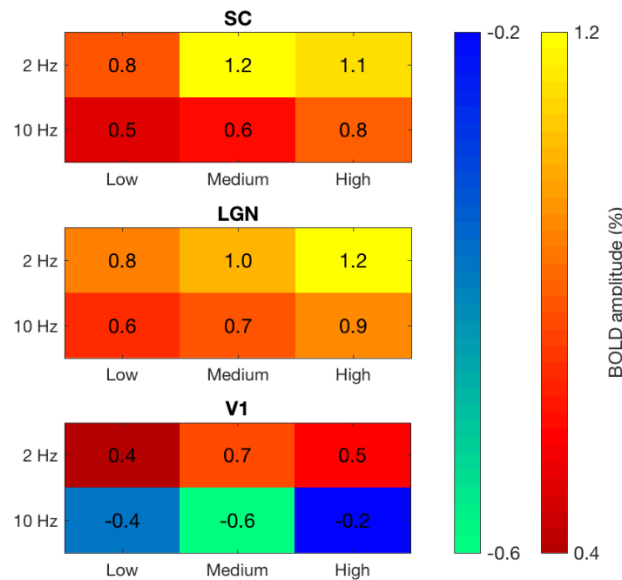


Figure 3.15 – Maximum BOLD percent signal change values in the SC, LGN and V1 for flickering stimuli at 2 Hz or 10 Hz and low ($9.2 \times 10^{-3} \text{ W/m}^2$), medium ($9.2 \times 10^{-2} \text{ W/m}^2$) or high ($8.1 \times 10^{-1} \text{ W/m}^2$) intensities.

Additionally, BOLD responses in the SC and LGN reached their maximum amplitude at about 4 to 5 seconds after the onset of stimulation for all stimulus conditions, while responses in V1 required about 5 to 8 seconds to reach the peak, as exemplified in Figure 3.7 for one stimulus condition. A second peak after the end of the stimulation was also found in the SC at almost all stimulus conditions, and in some cases in the LGN and V1 (Figure 3.7).

3.1.3. Experiment 2: BOLD responses to different frequencies under etomidate

The etomidate anaesthetic regime produced a stable respiratory rate and temperature of 104 ± 20 breaths/min and $35.5 \pm 1.4 \text{ }^\circ\text{C}$ (values indicated as mean \pm standard deviation), respectively, in the 4 mice that were used in Experiment 2. Figure 3.16 presents the timecourses of those parameters for each one of those mice. Similar to Experiment 1, temperature values rapidly decreased to values outside the normal physiological range after anaesthesia induction, starting to increase at a slower pace back to normal values just before the beginning of functional runs.

Despite the physiological stability, the 2nd mouse of this experiment died within one day after the end of the session. Moreover, this mouse also revealed almost no response to the stimuli in the visual

pathway. Figure 3.17 and Figure 3.18 present the brain map of significant BOLD activation for a single run and the average cycle of the BOLD response in ROIs along the pathway, respectively, following binocular visual stimulation with 2 Hz flickering frequency and $8.1 \times 10^{-1} \text{ W/m}^2$ of light intensity. Similar to what happened to the 3rd mouse from Experiment 1, responses to other stimulus conditions are also practically inexistent along the pathway. Therefore, the data from this mouse was not included in the group analysis.

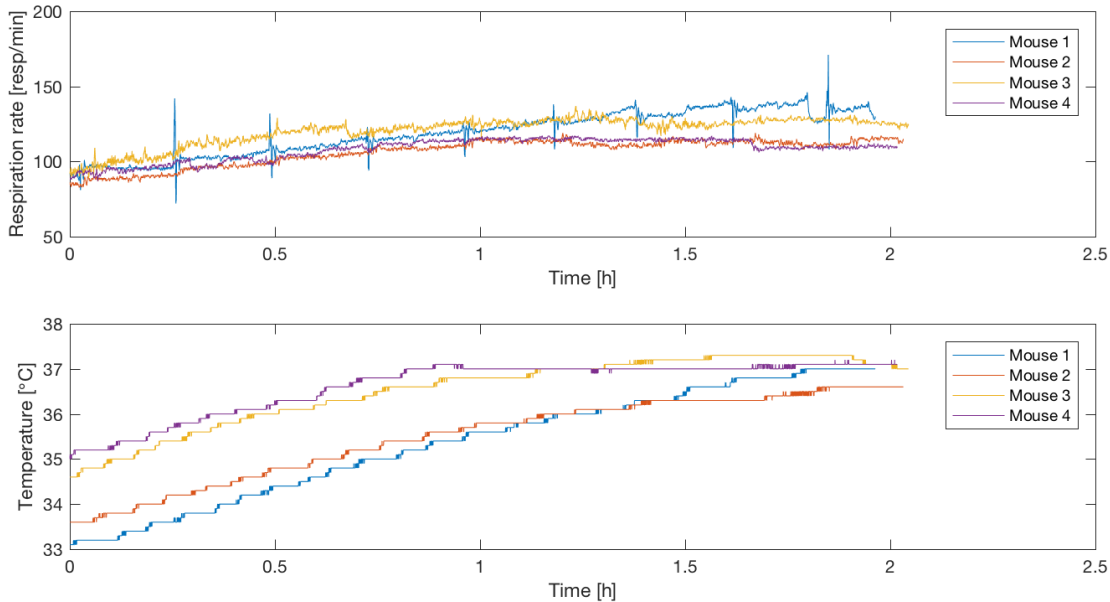


Figure 3.16 – Idem to Figure 3.10, but now for Experiment 2.

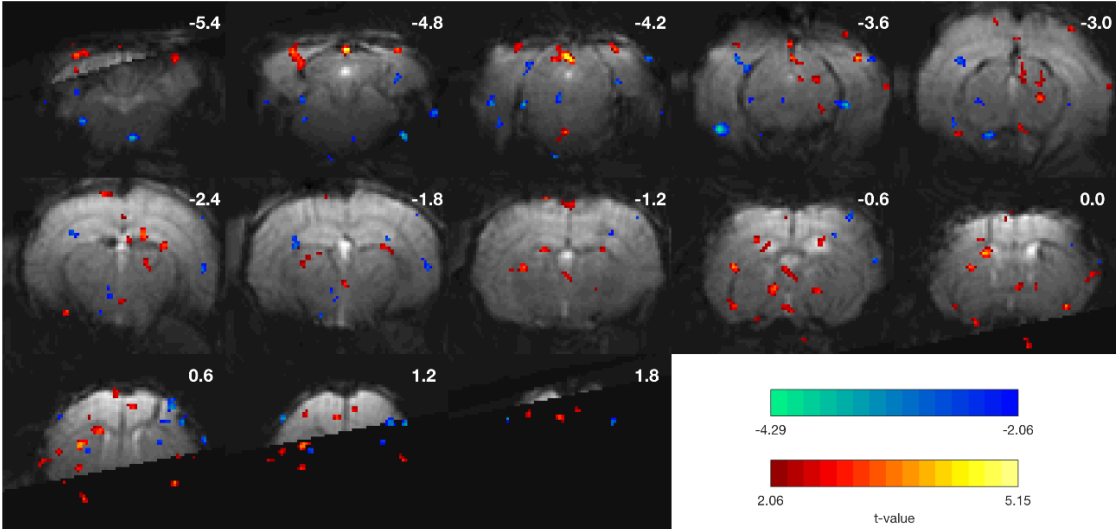


Figure 3.17 – Brain map of significant ($p < 0.02$, minimum cluster size = 8) BOLD activation to binocular visual stimulation with 2 Hz flashing frequency in consecutive coronal slices from one single run of the 2nd mouse used in Experiment 2. Approximate distances from Bregma are indicated in each slice. The most rostral and caudal image slices are cut as a result of realignment, coregistration and normalization.

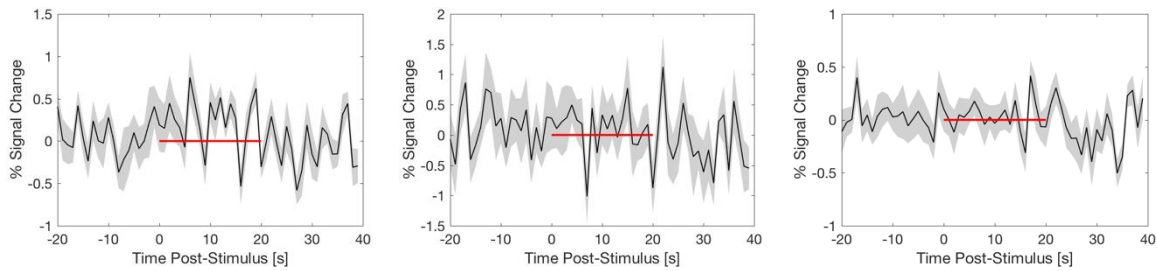


Figure 3.18 – Average cycle of the BOLD response to binocular visual stimulation with 2 Hz flashing frequency in the SC (*Left*), LGN (*Middle*) and V1 (*Right*) of the 2nd mouse used in Experiment 2 ($n = 2$ runs), plotted as mean percentage of signal change (solid line) \pm standard error of the mean (shaded region). The red bars indicate one 20 s stimulation period.

The group-level maps for each frequency are shown in Figure 3.19 for 2 Hz of flickering frequency, Figure 3.20 for 5 Hz, Figure 3.21 for 10 Hz and Figure 3.22 for 20 Hz stimuli. In general, significant BOLD responses to the stimuli are identified in the SC, V1 and LGN, but not at all frequencies. In particular, the SC responds to almost all flickering frequencies, registering high t -values in both sides of the brain, the highest being detected at 2 Hz. Furthermore, the span of the activation seems to be approximately equal for the 2 Hz, 5 Hz and 10 Hz frequencies. However, the group-level map for 20 Hz stimuli does not document significant SC responses. Clusters of activation in the LGN also seem to be approximately of the same size for the three lower frequencies of stimulation, and significantly reduced for the 20 Hz. On the other hand, the t -values in V1 show a clear negative trend with frequency, with the highest t -values and number of responsive voxels being detected at 2 Hz, and the lowest t -values at 20 Hz. Although V1 responds to all frequencies, relatively few voxels are considered statistically significant at 5 Hz and 10 Hz.

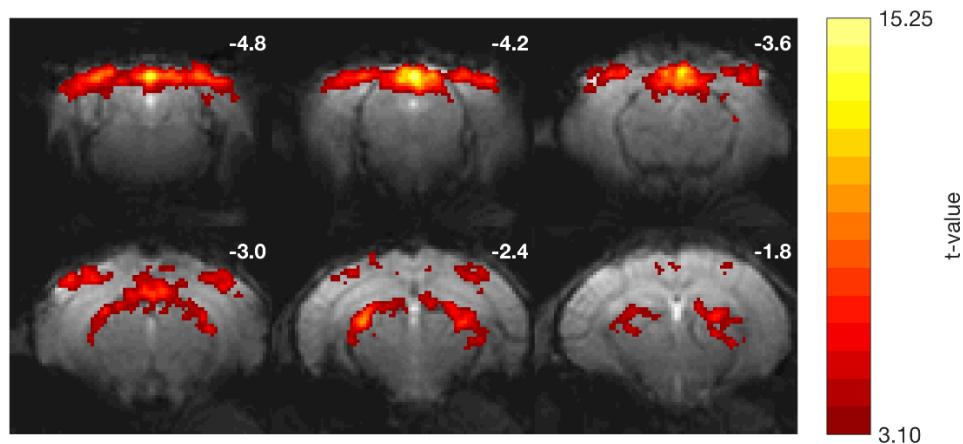


Figure 3.19 – Brain map of significant ($p < 0.001$, minimum cluster size = 8) BOLD activation to binocular visual stimulation with 2 Hz flashing frequency in consecutive coronal slices from an average of 3 mice ($n = 6$ runs). Approximate distances from Bregma are indicated in each slice.

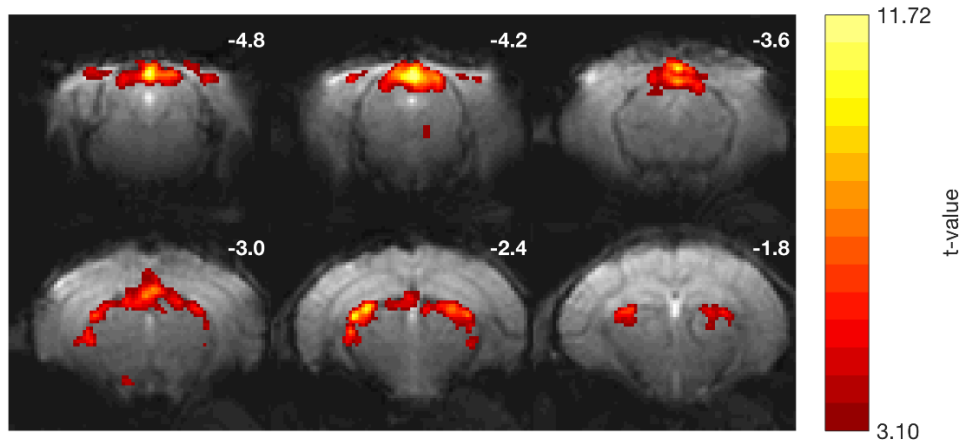


Figure 3.20 – Brain map of significant ($p < 0.001$, minimum cluster size = 8) BOLD activation to binocular visual stimulation with 5 Hz flashing frequency in consecutive coronal slices from an average of 3 mice ($n = 6$ runs). Approximate distances from Bregma are indicated in each slice.

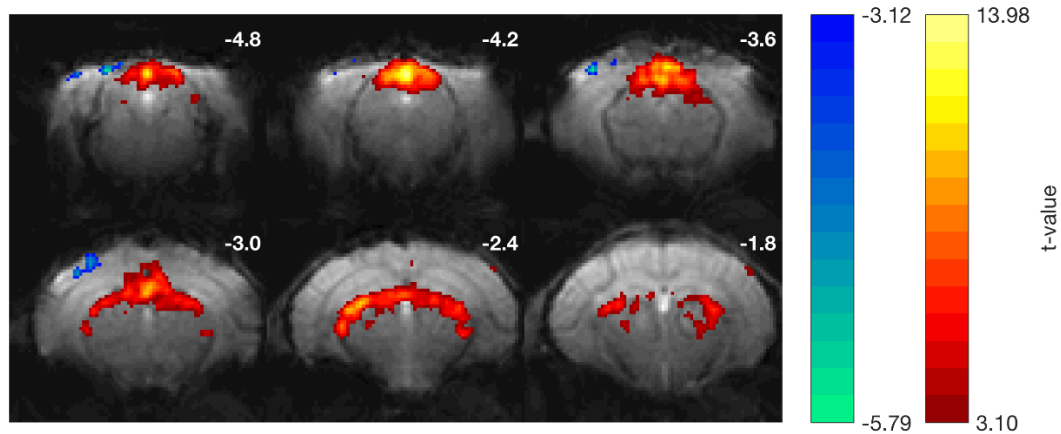


Figure 3.21 – Brain map of significant ($p < 0.001$, minimum cluster size = 8) BOLD activation to binocular visual stimulation with 10 Hz flashing frequency in consecutive coronal slices from an average of 3 mice ($n = 6$ runs). Approximate distances from Bregma are indicated in each slice.

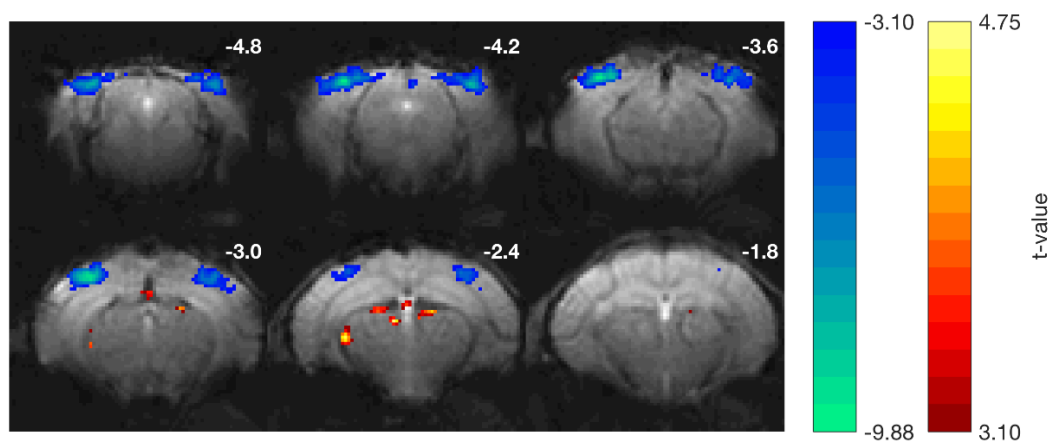


Figure 3.22 – Brain map of significant ($p < 0.001$, minimum cluster size = 8) BOLD activation to binocular visual stimulation with 20 Hz flashing frequency in consecutive coronal slices from an average of 3 mice ($n = 6$ runs). Approximate distances from Bregma are indicated in each slice.

As observed in Figure 3.23, the smallest peak amplitudes of the average cycle of the BOLD response in the SC and LGN were detected at 20 Hz. On the contrary, responses in these regions attained high peak values at the other tested frequencies, with LGN reaching the highest percent signal change values. Whereas responses in V1 at 2 Hz and 5 Hz are clearly positive in both sides of the brain, reaching their peaks at positive values, BOLD responses at 10 and 20 Hz exhibited negative peaks. A negative trend with frequency is found in the BOLD contrast of V1, with the most negative peak value being registered for 20 Hz.

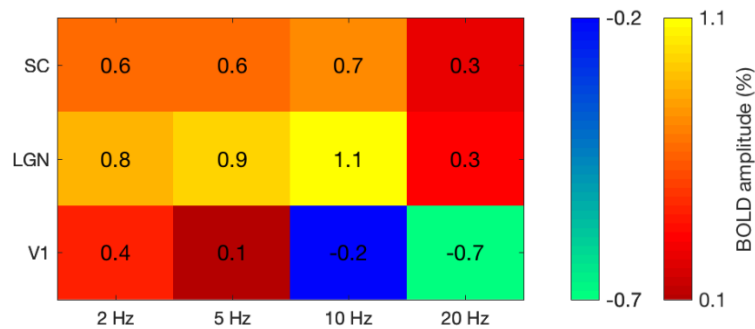


Figure 3.23 – Maximum BOLD percent signal change values in the SC, LGN and V1 for flickering stimuli at 2 Hz, 5 Hz, 10 Hz or 20 Hz.

Similar to what is shown for Experiment 1, responses in the SC and LGN reached their maximum amplitude at about 4 to 5 seconds after the onset of stimulation for 2 Hz, 5 Hz and 10 Hz stimuli. Moreover, responses in V1 at 2 Hz and 20 Hz reached the positive or negative peak at 6 and 8 seconds, respectively. However, times to peak in the SC and LGN at 20 Hz and in V1 at 5 Hz and 10 Hz deviated from these intervals. Responses in the SC and LGN peaked around 3 seconds at 20 Hz, while responses in V1 at 5 Hz and 10 Hz peaked (positively and negatively, respectively) after 4 and 9 s, respectively. Nevertheless, it should be noted that these responses do not have very well-defined peaks compared with the others, since variations from the baseline are very small.

3.1.4. Experiment 3: BOLD responses under medetomidine

The physiological parameters of all mice used in this experiment were stable during the entire experimental session (Figure 3.24), with a mean \pm standard deviation of 112 ± 16 breaths/min and 35.0 ± 1.2 °C across all mice. Moreover, due to the administration of atipamezole, medetomidine effects could be reversed and mice could return to their normal state within 15 minutes after injection of the antagonist. It should be noted, however, that the 3rd mouse used in this experiment was found dead within one week after the experimental session. Nonetheless, in this case, one cannot infer if this was caused by the administration of medetomidine or by any other reason intrinsic or extrinsic to the experiment. It is also important to report that, on the contrary to mice anaesthetized with etomidate, these three mice started to move while they were still in the scanner, respectively 3 h, 1 h 50 min, and 2 h 50 min after the bolus of medetomidine.

Similar to previous experiments, temperature values decreased to values outside the normal physiological range after anaesthesia induction and started to increase at a slower pace back to normal values before the beginning of functional runs.

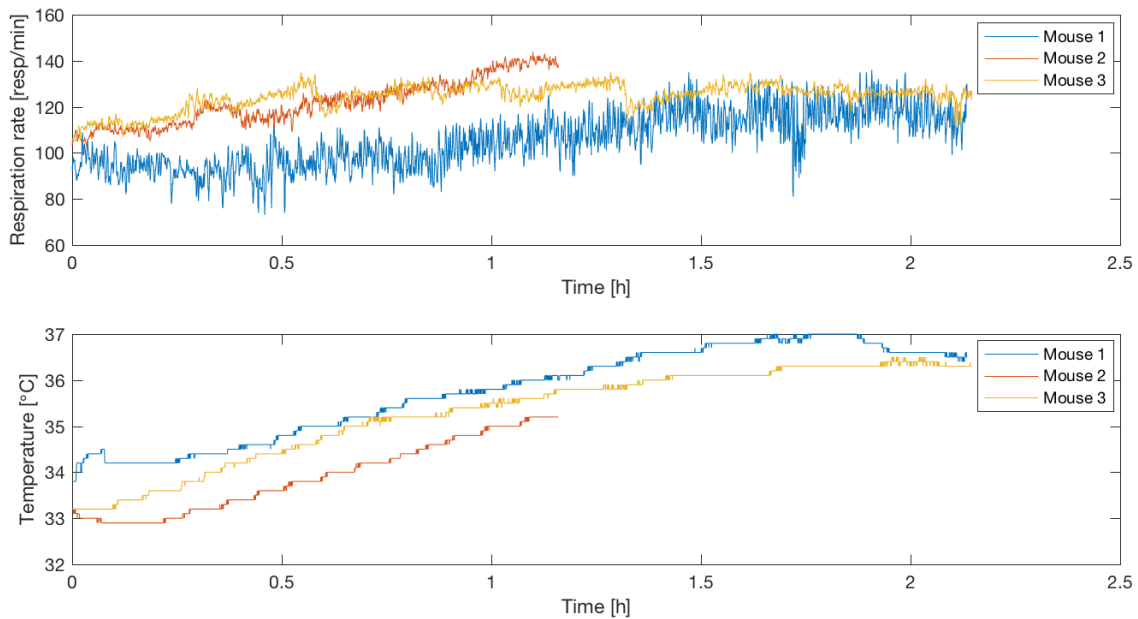


Figure 3.24 – Respiration rate (in respirations per minute) and temperature (in °C) plots for all mice used in Experiment 3, from the time that functional acquisition started until the moment the animal started to move.

According to the group visual map for 2 Hz stimuli shown in Figure 3.25, the greatest density of voxels with statistically significant responses is found in the SC, V1 and LGN. Moreover, this map showed higher t -values in comparison to the equivalent maps obtained for mice sedated with etomidate presented in the bottom of Figure 3.13 and in Figure 3.19.

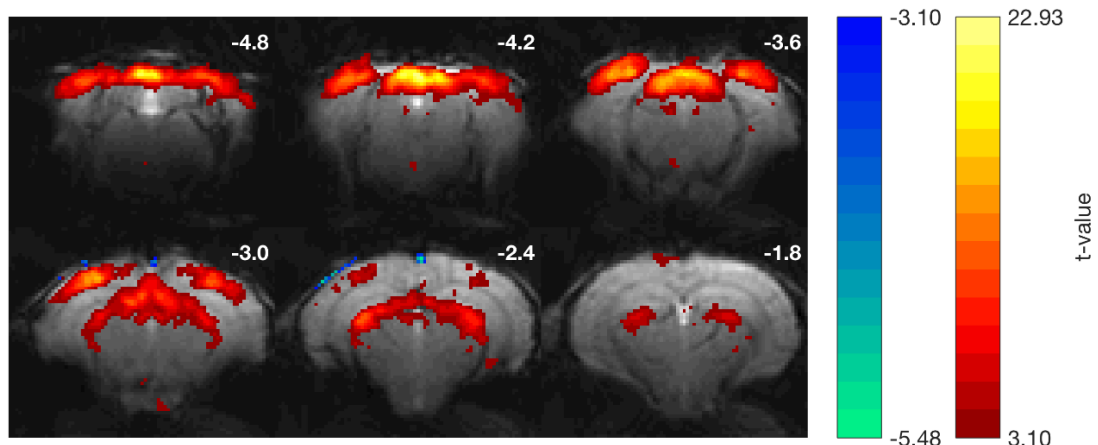


Figure 3.25 – Brain map of significant ($p < 0.001$, minimum cluster size = 8) BOLD activation to binocular visual stimulation with 2 Hz flashing frequency in consecutive coronal slices from an average of 3 mice ($n = 6$ runs) anaesthetized with medetomidine. Approximate distances from Bregma are indicated in each slice.

Mean BOLD responses to the visual stimulus for the LGN, SC and V1 are shown in Figure 3.26 for mice anaesthetized with medetomidine and mice anaesthetized with etomidate from Experiment 2. The maximum BOLD percent signal change value differs between each region of medetomidine-sedated mice, with the highest being found in the SC (approximately 2.0%) and the lowest in V1 (about 1.1%). Peak amplitude in the LGN is found at 1.6%. Moreover, these structures reach their maximum contrast about 4 to 5 seconds from the stimulus onset. Additionally, the SC shows a strong decrease in the BOLD contrast after the initial peak, exhibiting a second peak in activation slightly before stimulation is turned off. Contrarily, LGN response appears to remain constant throughout the whole stimulation period. V1 response is also shown to slightly decrease throughout the entire period and to go below baseline for some seconds when stimulation is off.

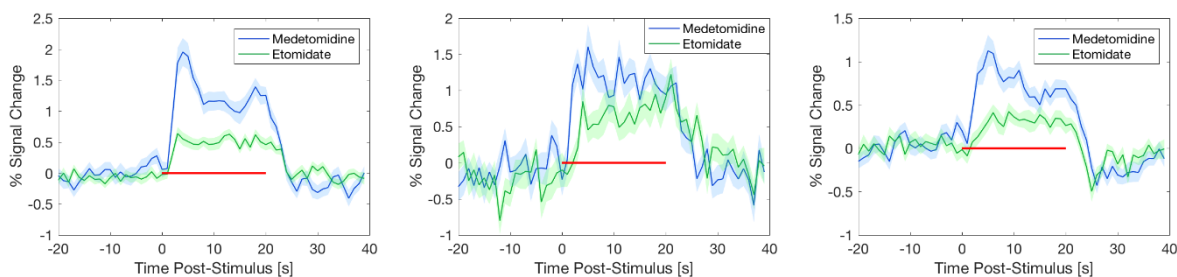


Figure 3.26 – Cycle of the BOLD response to binocular visual stimulation with 2 Hz flashing frequency in the SC (Left), LGN (Middle) and V1 (Right) of mice anaesthetized with medetomidine (blue tones) and etomidate (green tones). Timecourses were averaged over 3 animals ($n = 6$ runs) and plotted as mean percentage of signal change (solid line) \pm standard error of the mean (shaded region). The red bars indicate 20 s stimulation periods.

Despite that the shape of the BOLD responses in the SC, LGN and V1 is similar for both anaesthetics, clear higher maximum BOLD percent signal change values are found in mice anaesthetized with medetomidine, especially in the SC and V1.

3.2. Optimization of Etomidate Dosage

As described in Section 2.2, 9 mice were divided into 3 different groups and subjected to distinct anaesthetic regimes with the purpose of decreasing the mortality rate and the long time for recovery that etomidate was causing in the animals from the previous experiments. Table 3.1 summarizes some of their characteristics at the time of the experiment, namely their age and weight, and the average respiration rate and temperature throughout the experiment, from the time isoflurane was completely discontinued until the end of the 3 hours after bolus.

All mice remained stabilized and motionless during the 3 hours under etomidate sedation, with the exception of the two mice (mouse 1 and 4 from Table 3.1) in which isoflurane was discontinued too early (20 minutes after bolus), and that exhibited some movements ~3-7 minutes after isoflurane was lowered to 0%. Nevertheless, after introducing isoflurane at 0.5-1% for 10 more minutes, both these mice remained stable until the end of the experiment, without having any other burst of activity.

Moreover, after adopting the anaesthesia protocol with a longer time to completely remove isoflurane (in Figure 2.7) for the remaining 7 mice, this problem did not occur anymore.

In the end of the experiment, only one mouse (mouse 3 from Table 3.1) died. This animal belonged to the group that was administered with the highest dosage of etomidate.

Table 3.1 – Age, weight and physiological parameters, indicated as mean \pm standard deviation, of mice that were subjected to one of the 3 different anaesthetic regimes. The values for the respiration rate and the temperature were averaged from the recordings obtained from the complete discontinuation of isoflurane until the end of the experiment. The symbol † indicates death.

Group	Mouse	Age (weeks)	Weight (g)	Respiration rate (respirations/min)	Temperature (°C)
1	1	8	27.1	95 \pm 5	35.9 \pm 0.3
	2	8	26.1	97 \pm 6	35.4 \pm 0.4
	3 †	7	26.8	108 \pm 4	35.2 \pm 0.3
2	4	8	27.4	91 \pm 10	35.1 \pm 0.7
	5	8	26.7	123 \pm 11	35.5 \pm 0.5
	6	7	23.5	146 \pm 11	35.8 \pm 0.5
3	7	8	23.3	107 \pm 8	35.3 \pm 0.4
	8	8	28.5	118 \pm 13	36.3 \pm 0.5
	9	7	27.2	107 \pm 5	36.1 \pm 0.6

4

Discussion

The present chapter is dedicated to the discussion of the methods employed in this project and the analysis of the results obtained. Results from visual stimulation fMRI experiments in mice are compared to the literature and possible improvements to the imaging techniques, the protocol for anaesthesia with etomidate and the developed system for delivery of complex and varied stimuli are described.

4.1. Visual Stimulation fMRI Experiments

Before discussing particular results obtained for each of the three visual stimulation fMRI experiments presented above, considerations on choices made in the protocol for all experiments should be presented.

Choice of mouse strain, gender and age. Male C57BL/6J mice aged 7 to 8 weeks were used since female mice of this strain exhibited lower contrast sensitivity than male counterparts [132]. Moreover, hormonal variations associated with the oestrous cycle might indirectly increase variations in fMRI results obtained. Additionally, it was desired that mice had already reached adulthood to ensure that their visual system was fully developed, but without showing any visual impairment caused by aging. Since a new anaesthetic protocol was being tested for the first time, we attempted to ensure that mice survive the initial dosage of etomidate, which older age may compromise.

Choice of pulse sequences. We have chosen to work with GE-EPI pulse sequences for delivering the functional contrast in this study. GE-EPI provides very good spatiotemporal resolution and very good sensitivity towards BOLD signals due to its reliance on T_2^* contrast. However, GE-EPI is also somewhat less robust toward field inhomogeneities, which in turn can cause some signal loss and image distortions in the brain (Figure 3.2). In the most posterior slices, V1 was affected by these distortions and the analysis of the BOLD response to different types of visual stimuli was greatly compromised. SE-EPI, FLASH, or other types of fast sequences that are less sensitive in the low bandwidth dimension can be used in the future to ensure less artefacts; alternatively, one slice – even at the posterior of the brain – can be shimmed (rather than the entire brain, as it was done in this study), and the corrections are typically sufficient to produce excellent GE-EPI images, if only for a single slice.

BOLD contrast. It is interesting to consider that GE BOLD signals can be influenced by hemodynamic variations in large vessels distant from the firing neurons [45]. In the future, SE-EPI can be performed to provide complementary information and, due to SE-EPI's sensitivity towards T_2 mechanisms, the microvascular contributions can be accentuated, thereby improving specificity at the cost of a reduced BOLD sensitivity [46] and perhaps also temporal resolution.

Major efforts have been made to try to link BOLD signal changes to neuronal spiking or local field potentials [133][31]. Given that the BOLD signal is sensitive to blood dynamics and oxygenation in vessels and is not directly related to neuronal activity, it becomes difficult to assess direct circuit dynamics through BOLD fMRI. Moreover, as mentioned in Section 1.3.4, BOLD responses have been shown to be modulated by the type of anaesthetic used [134][135]. Therefore, care must be taken when inferring underlying neuronal activity directly from the measured BOLD signal in anaesthetised rodents. In this way, future experiments could make use of non-BOLD techniques such as diffusion-weighted fMRI that measures water diffusion in brain tissues and allows to achieve a greater specificity in the maps.

Data analysis considerations. Although corrections performed at the slice level slightly decreased the maximum t -values found in the statistical parametric maps, as shown in Figure 3.5, they also helped removing significant artefacts from the maps. Moreover, despite the fact that *ex vivo* brain images have been used as a reference for normalization [129], this seemed to be quite accurate for all animals used in the fMRI experiments of this project. Because all acquisitions differed slightly on the exact position of the slices, which were also not exactly coronal, and because brain dimensions differ between animals, the three alignment steps that were applied to the images during preprocessing cut the most rostral and caudal slices, as shown in the mean functional images of the brain displayed in Figure 3.8. Nevertheless, in the context of this study this does not appear to be of particular interest or source of problem.

Although SPM offers the possibility to use the canonical HRF to predict the BOLD response to a given stimulus paradigm, this model was specifically designed for humans, whose response function has been estimated to peak at 5-6 seconds [47]. In 2009, Wall et al. found that the hemodynamic response functions that best fitted the SC response to binocular stimulation in humans peaked at 4 to 5 seconds after stimulus onset, while the responses that best fitted the LGN profile peaked at 6 seconds [136]. However, a much shorter response function has been demonstrated in mice. For example, Pisauro et al. verified that hemodynamic responses in the primary visual cortex of mice peaked at approximately 2 seconds in awake mice and at 4 seconds in mice anaesthetized with isoflurane [137]. Therefore, instead of using the canonical HRF in this study, different functions that peaked at less than 5 seconds were tested to find which ones were most accurate to predict the BOLD response to the stimuli. The convolution of the chosen function (HRF number 3 in Table A.1) with the paradigm peaked at 6.51 seconds, which seems adequate since the BOLD responses in the three main regions of the visual pathway studied in this project have been shown to peak in the 4 to 8 seconds' interval, independently of the anaesthetic being used. Nevertheless, it should be noted that even though the function chosen for the HRF might not be the most accurate model to explain hemodynamic activity across the whole brain, it is also known that this has little effect on the predicted BOLD response in blocked designs, because this response becomes constant for much of each block: it saturates at task blocks and it decays to zero at rest blocks [38]. However, as with any model, the model used is constrained to the model parameters. In the future, coherence analysis can be used to avoid the specifics of the HRF (to first order), and other data-driven approaches can be used to test the validity of the SPMs.

Finally, one needs to be wary of unreliable statistical results, namely due to the multiple comparisons problem. Very high rates of false positives in single-subject fMRI analysis have been demonstrated, especially when using blocked designs and short TRs [138]. A different way of performing the analysis of fMRI data that has been suggested to counteract this problem is to follow a non-parametric approach, such as a permutation test, that originates familywise error rates closer to the expected values. Although it seems unlikely that the accurate activation of all visual pathway components reported here is a statistical fluke, such nonparametric tests could be performed in the future to contrast the SPM results with more stringent tests.

4.1.1. Light intensity and frequency tuning under etomidate

Regions exhibiting highly significant BOLD activation upon visual stimulation in all experiments performed in this project included the SC, LGN and V1, which is in agreement to previous rodent visual fMRI studies [17][112][113][114][116]. Although a clear separation between the superficial, intermediate and deep layers of the superior colliculus has not been observed in the statistical maps, higher t -values in this subcortical region seem to be localized in the most dorsal layers, which was expected since these are the ones known to receive direct projections from the retina. Therefore, if the ROI analysis had separated the SC into these three main layers, the strongest BOLD responses would likely be detected in the superficial layers.

As observed in the maps shown in Figure 3.13 and Figure 3.14, the t -values and the number of responsive voxels in the SC increased from the lowest intensity ($9.2 \times 10^{-3} \text{ W/m}^2$) to the higher intensities ($9.2 \times 10^{-2} \text{ W/m}^2$ and $8.1 \times 10^{-1} \text{ W/m}^2$). Moreover, when analysing the dynamics of the response at the ROI level, as seen in Figure 3.15, smaller BOLD amplitudes were detected in the SC and LGN for the lowest intensity in comparison to the others, either for 2 Hz or 10 Hz flashing stimuli. These results are in good agreement with the results obtained by Zhang et al. [112], which found that BOLD response in the SC of Sprague-Dawley rats is weaker under dim light and that it saturates at higher intensities, suggesting that these dependences reflect retinal responses. Specifically, they found the lowest response amplitude and number of activated voxels in the SC for $4.2 \times 10^{-3} \text{ W/m}^2$, which is at the same order of magnitude as the lowest frequency tested in this study for mice, and relatively small differences in amplitude and number activated voxels from $7.6 \times 10^{-2} \text{ W/m}^2$ to 0.74 W/m^2 stimuli, whose orders of magnitude are also the same as the medium and highest intensities applied in this study, respectively.

Maximum BOLD percent signal change values found in the SC, LGN and V1 for flickering stimuli at 2 Hz, 5 Hz and 10 Hz (Figure 3.23) are very close to the values found for the BOLD contrast in the fMRI study in mice done by Niranjana and colleagues [17]. In contrast to what they found, responses in the SC and LGN in the present work did not show a positive trend in BOLD amplitude with increasing frequency. Even if the amplitude of the BOLD response in Experiment 2 slightly increased from 2 Hz to 10 Hz stimuli for both of these regions, the same was not detected in Experiment 1 (Figure 3.15). Nevertheless, it should be noted that the slope of the increase of the BOLD contrast with frequency found in their study was not very steep either, and that the strongest frequency preference was found in V1 in comparison to those subcortical structures. Moreover, the bilateral negative BOLD responses elicited in V1 at 10 Hz, as shown in Figure 3.14 and Figure 3.21, and the negative trend it shows in response to increasing frequency are in agreement with their findings. They suggested that these negative responses observed at higher frequencies can be explained by a breakdown in neurovascular coupling at higher temporal frequencies, or by inhibitory neurons elsewhere in the brain that decrease neuronal activity in V1 and trigger these negative BOLD responses.

All these ROI analyses should be further validated resorting to statistical tests that compare the BOLD amplitude and the number of responsive voxels between different regions, light intensities and frequencies.

In 2013, Bailey et al. measured BOLD responses to flashing light in the brain of Long Evans rats and compared these signals with extracellular recording from the SC and V1 [16]. They found that the neural activity becomes decoupled from the BOLD response with increasing frequency, especially at 10 Hz, at which the plateau of the BOLD response did not become negative but was significantly attenuated in comparison to 1 Hz stimuli. On the contrary to what was found in this study for mice (Figure 3.7), their data shows that BOLD signal peaks occurred first in V1 and only then in the SC. Still, that difference did not seem to be significant in their study given the high standard deviation of those values. Moreover, different anaesthetic and species were used in their study, which does not allow a direct comparison between these results.

The decay in the response after the initial peak exhibited by the SC and V1 of mice anaesthetized with etomidate (Figure 3.7) and medetomidine (Figure 3.26) in the present study had already been found in rat studies for stimuli of 1 to 10 Hz [16][116], as well as the second peak in activation found in the SC and V1 following stimulus cessation at some stimulation frequencies, which may be a result of an “off” response in brisk-transient retinal ganglion cells following stimulation [139]. Furthermore, shown in Figure 3.15 and Figure 3.23, responses detected in V1 reached lower BOLD amplitudes than the SC and LGN even when positive responses were observed (for 2 Hz and 5 Hz), which is in line with the studies of Van Camp et al. and Pawela et al. in rats [115][116].

The temporal resolution of BOLD signals is also an important factor to consider in the context of onset times. In a recent rat fMRI study, approximately 0.2 seconds elapsed for the signal to reach 50% of maximum amplitude between the BOLD responses of the SC and LGN [113]. However, in this study, the temporal resolution was 1 second, rendering a proper separation of rise times infeasible. Nevertheless, after carefully visualizing the average cycles of the BOLD responses obtained with the study, it was possible to infer that the SC and the LGN peaked at about 4 to 5 seconds after stimulus onset, and the V1 at about 5 to 8 seconds. It is known that V1 receives visual information from the dorsal LGN through the optic radiation [59], which might explain this delay in the time-to-peak observed in V1 in comparison to the subcortical structures. Future experiments can make use of line-scanning techniques such as the one suggested by Niranjana et al. to measure BOLD signals at sub-second temporal resolution [125] or shorter duration stimuli that are better for estimating the shape of the hemodynamic response and the associated timing parameters [113].

4.1.2. Comparison between etomidate and medetomidine

The present study has demonstrated that regions of the visual pathway that exhibit significant responses to binocular visual stimuli in mice anaesthetized with medetomidine (Figure 3.25) also show significant responses in mice anaesthetized with etomidate under the same stimulus conditions (Figure 3.13 and Figure 3.19). Besides that, results regarding the frequency tuning capability of the SC, LGN and V1 observed in this work are very similar to the ones obtained from mice anaesthetized

with medetomidine [17], proving that subcutaneous etomidate is also a suitable anaesthetic for functional studies in mice.

Mice anaesthetized with etomidate that were subjected to the visual stimulation sessions remained physiologically stable and under a constant depth of anaesthesia for the time required to complete all desired scans (Figure 3.10 and Figure 3.16), even if it was necessary for them to stay under etomidate sedation for 4 hours. On the other hand, sedation with medetomidine did not last for more than 3 hours in either of the three mice, which led to an uneven number of runs performed across mice. Although it was only necessary to run a few acquisitions in this particular study in order to be able to make direct comparisons between the two anaesthetic regimes, this premature motion of the animals can compromise the completeness of future more complex fMRI experiments that require longer scanning sessions. Moreover, subcutaneous etomidate avoids the large infusion volumes and complex experimental setup that intravenous infusion requires for mice [22], decreasing the risk of fluid overload or pulmonary edema [21].

Despite these important advantages of subcutaneous etomidate, some relevant differences between these two anaesthetics (etomidate and medetomidine) are worth mentioning. First, three mice died after being subjected to etomidate sedation. Two of these mice exhibited lack of responsiveness of the visual centres being studied in comparison to the other mice, as shown in the maps of Figure 3.11 and Figure 3.17 and in the ROI timecourses of Figure 3.12 and Figure 3.18, resulting in their discarding from the group analyses. This difference in mice recovery might be due to individual susceptibilities to anaesthesia or to the different times during which mice were being infused with etomidate. For example, one of the mice that died (1st mouse from Experiment 1) was the one that had the longest session of all mice used in this project (4 h 40 min). Still, it did not seem that time under sedation was the only fact that explained these differences, since there were mice that were administered with etomidate for 4 hours and recovered, and others (the other two mice that did not live) that were only anaesthetized for 3 h 15 min and did not survive. Secondly, the group-level statistical parametric map obtained from mice anaesthetized with medetomidine (in Figure 3.25) revealed higher t -values in comparison to the equivalent maps obtained for mice sedated with etomidate presented in the bottom of Figure 3.13 and in Figure 3.19. Moreover, despite that the shape of the BOLD responses in the SC, LGN and V1 was similar for both anaesthetics, ROI analyses in those regions revealed higher maximum BOLD percent signal change values in mice anaesthetized with medetomidine, as it can be confirmed by comparing timecourses displayed in the ROI plots of Figure 3.26.

All this cumulative evidence points to the same conclusion: the protocol suggested by Klee et al. [22] may not be optimal for long fMRI scanning sessions, and may in fact be much too stringent. The possibility of decreasing the dosage of etomidate should be tested, such that the mortality rate and functional SNR of these experiments are matched or superior to medetomidine. It should also be noted in this context that if medetomidine is administered at higher doses, the fMRI signals disappear (data not shown).

The physiology measurements obtained from animals used in the three different experiments exhibited a steep decrease on the temperature values in the first ~30 min after anaesthesia induction, followed

by their slow increase until the end of the session. This suggests that heating is not sufficient to avoid hypothermia (~32 °C) in the beginning of the experiments. Although no detrimental effects were seen on BOLD responses in this study, future experiments should avoid such decreases in the temperature so that quality of BOLD responses does not become affected by physiological fluctuations during the session. This can be accomplished by placing for example a second heating pad above the animal during the first hour of the experiment, or even through the use of a feedback controlled heating system.

4.2. Optimization of Etomidate Dosage

The mortality that was observed as a result of the administration of subcutaneous etomidate in the visual stimulation experiments performed in this study was carefully analysed in terms of its causes and ways to decrease it, since it might prevent etomidate's use for longitudinal functional studies in the future, which was stated as one of the most promising characteristics of this anaesthetic [20].

Interestingly, it has been reported that a long-term administration of etomidate in septic patients requiring mechanical ventilation is associated with an high mortality rates [140]. Moreover, it has been shown that etomidate causes adrenocortical suppression with a significant decrease in plasma cortisol, corticosterone and aldosterone concentrations [141]. This happens because the enzyme that is responsible for converting 11-deoxycortisol to cortisol, named 11- β -hydroxylase, is inhibited by etomidate in a dose-dependent manner, leading to an increase in the levels of cortisol precursors and adrenocorticotrophic hormone [142]. Cortisol is a glucocorticoid produced in the adrenal cortex of the adrenal glands that influences glucose, protein and fat metabolism. Among its functions, cortisol inhibits protein synthesis in tissues, promotes breakdown of triglycerides and fatty acid release from adipose tissue to decrease the use of glucose as an energy source, and stimulates liver cells to synthesize glucose from non-carbohydrates. These actions help maintain normal blood glucose levels between meals [35][60]. Furthermore, it also has anti-inflammatory effects by inhibiting white blood cells that participate in inflammatory responses [60].

It has been reported that vitamin C supplementation can inhibit adrenal suppression and restore cortisol levels back to normal after etomidate use [143][144][145], likely due to its positive regulation of cortisol synthesis from cholesterol [35][146]. Therefore, one possible way to try to decrease the observed negative effects of etomidate on mice could be the supplementation of their diet with vitamin C. This could be administered for example in drinking water at about 1 mg/day, one or two weeks prior to the experiment [147].

Moreover, we have attempted to decrease etomidate dosage and still maintain a sufficient depth of anaesthesia during the whole experiments. Our preliminary results show that mice can remain physiologically stable and motionless even if the constant infusion dosage is decreased to 1/3 of its initial value (Table 3.1). Even more promising, it should be noted that the mice subjected to lower dosages did not die although n.b. that only 3 animals were tested. Future work will test this new regime in the context of an fMRI session, along with its associated acoustic noises, in order to properly

conclude if this decrease in the dosage still guarantees a sufficient depth of anaesthesia in mice that prevents them from moving when they are being intensively stimulated. Moreover, it should also be confirmed through fMRI experiments if the extension of the time to completely discontinue isoflurane in the beginning of each session that was suggested in Figure 2.7 does not suppress BOLD response, given the limitation on neurovascular reactivity this substance is known to cause [103].

4.3. Setup for Delivery of Complex Visual Stimuli

As shown in Figure 2.10, the setup developed for presentation of spatially structured visual stimuli to mice was able to accurately fit in the confined space of the scanner as expected from the 3-D models shown in Figure 2.8. Even if the resonator with a large diameter and a small loop surface coil have been chosen as the electromagnetic coils to be used in combination with the new visual stimulation system, limitations in space were still a major challenge when designing it. Therefore, even if small adjustments on the current position of the screen can be done in the future and other screens be added to the current setup, there will not probably be much space for large modifications. Binocular visual stimulation by repositioning the screen in the binocular visual field of the mouse might also be possible, with the constraint that the screen cannot be placed at the preferred binocular distance for mice (approximately 10 cm [148]). Smaller adjustments in the piece that was 3-D printed for accurate positioning of the OLED in front of the eye throughout experiments can also be done in order to provide more stability to it and a better fixing to the animal bed.

The use of the OLED display instead of multiple fibre-coupled LED sources revealed to be a much lower cost and versatile solution, given the small budget that was required to buy all components of the setup (Figure 2.9) and the capability to provide a vast variety of stimuli that would not be possible with a limited number of fibre-coupled LEDs. The electronic components that were connected to the screen are at a sufficient distance to not be interfered by induced currents from the scanner, as it was verified when the setup was brought to the scanner room and some preliminary tests were done.

Given the orientation and direction selectivity as well as the speed tuning capability that have been observed in V1, LGN and SC of the mouse through innumerable electrophysiological and calcium and intrinsic signal imaging studies [5][8][9][84][90][91], the setup was programmed to deliver bars moving at different speeds along the vertical and horizontal directions in order to provide comparative fMRI data to complement the existing literature (Figure 2.10). Even though the setup has not been tested with an *in vivo* experiment in order to check if mice are responding to the designed stimuli and if the eye patch that was also 3-D printed avoids the leakage of light into the contralateral eye of the animal, modifications can be readily incorporated into the stimulator given the flexible software control that is available and the easiness to print small 3-D pieces in a matter of minutes.

5

Conclusions and Future Work

This chapter provides a summary of all work carried out under the scope this thesis, as well as some important guidelines for future work.

This thesis focused on the development and application of a setup capable of delivering complex visual stimuli to mice, thereby enabling investigation of the brainwide visual pathway responses using fMRI. We developed and demonstrated the suitability of a new free-breathing anaesthesia protocol based on subcutaneous injection of etomidate for fMRI studies in mice. The mouse visual pathway was mapped using high-resolution BOLD fMRI following binocular stimulation with flashing lights at 9.4T. Highly significant BOLD responses were observed in the SC, LGN and V1 of the mouse brain at both subject and group levels, and for all stimulus conditions. Light intensity and frequency tuning were studied and agreed with previous electrophysiological and fMRI findings in mice subjected to other anaesthetic regimes. Mice remained physiologically stable and motionless for the entire scanning session, on the contrary to mice anaesthetized with the state-of-the-art fMRI anaesthesia (medetomidine). Together, these observations validate the use of subcutaneously administered etomidate for visual fMRI in mouse models. However, an increased mortality rate likely reflects that the dosages used here were too high; however, we have shown that mice receiving 1/3 of the previous dosage also remain stable and motionless for a long period of time (>3 h). Future studies will repeat some of the fMRI experiments here to find the optimal dosage where mouse stay stable for >3 h, retain the BOLD responses, and recover well from the experiments. Supplementation of diet with vitamin C should also be attempted, given its capability to inhibit adrenal suppression caused by etomidate. In addition, we will perform additional orthogonal physiological stability measurements, such as partial pressure of carbon dioxide ($p\text{CO}_2$) and partial pressure of oxygen ($p\text{O}_2$), as well as blood pressure, to show that the protocol provides very stable physiological conditions over time.

We have also developed the OLED screen and showed that it is compatible with the magnet environment. To our knowledge, this is the first attempt at building a system for small rodent preclinical fMRI capable of delivering complex 2-D stimuli, which will allow to study, among others, motion, orientation, direction or even shape dependence in the entire pathway. The use of OLEDs eliminates most of the problems encountered with visual stimulation delivery in the confined space of a small animal scanner, while keeping the whole setup at a low cost. The capabilities of the system can be extended in the future, given the flexibility and ease of programming a wide variety of stimuli, to incorporate more screens into the setup and to print any 3-D pieces that would help fixing the screen(s) at the desired positions. Comprehensive fMRI experiments to investigate the global brain activity arising from complex pattern presentation in the mouse will be done in the near future to fully validate this new visual stimulation system. In turn, this will pave the way not only for studying complex stimuli, but also for optogenetic or other types of manipulations that are highly feasible in mice.

Finally, it is worth noting that the existing dataset can benefit from further analyses, such as mapping of coherence, that would enable detecting phase differences between BOLD signals of the different visual centres, thereby avoiding the need to assume an HRF model. These, as well as other more stringent statistical tests comparing between anaesthesia conditions, will be performed in the near future.

References

- [1] L. M. Chalupa and J. S. Werner, *The visual neurosciences*. MIT Press, 2004.
- [2] G. T. Prusky and R. M. Douglas, "Characterization of mouse cortical spatial vision," *Vision Res.*, vol. 44, no. 28, pp. 3411–3418, Dec. 2004.
- [3] N. J. Priebe and A. W. McGee, "Mouse vision as a gateway for understanding how experience shapes neural circuits," *Front. Neural Circuits*, vol. 8, p. 123, Oct. 2014.
- [4] L. Luo, E. M. Callaway, and K. Svoboda, "Genetic dissection of neural circuits.," *Neuron*, vol. 57, no. 5, pp. 634–60, Mar. 2008.
- [5] M. S. Grubb and I. D. Thompson, "Quantitative Characterization of Visual Response Properties in the Mouse Dorsal Lateral Geniculate Nucleus," *J. Neurophysiol.*, vol. 90, no. 6, pp. 3594–3607, Aug. 2003.
- [6] C. M. Niell and M. P. Stryker, "Highly Selective Receptive Fields in Mouse Visual Cortex," *J. Neurosci.*, vol. 28, no. 30, pp. 7520–7536, Jul. 2008.
- [7] L. Wang, R. Sarnaik, K. Rangarajan, X. Liu, and J. Cang, "Visual receptive field properties of neurons in the superficial superior colliculus of the mouse.," *J. Neurosci.*, vol. 30, no. 49, pp. 16573–84, Dec. 2010.
- [8] M. L. Andermann, A. M. Kerlin, D. K. Roumis, L. L. Glickfeld, and R. C. Reid, "Functional Specialization of Mouse Higher Visual Cortical Areas," *Neuron*, vol. 72, no. 6, pp. 1025–1039, Dec. 2011.
- [9] J. H. Marshel, M. E. Garrett, I. Nauhaus, and E. M. Callaway, "Functional specialization of seven mouse visual cortical areas.," *Neuron*, vol. 72, no. 6, pp. 1040–54, Dec. 2011.
- [10] S. Ogawa, T. M. Lee, A. R. Kay, and D. W. Tank, "Brain magnetic resonance imaging with contrast dependent on blood oxygenation.," *Proc. Natl. Acad. Sci. U. S. A.*, vol. 87, no. 24, pp. 9868–72, Dec. 1990.
- [11] L. Stefanacci *et al.*, "fMRI of monkey visual cortex.," *Neuron*, vol. 20, no. 6, pp. 1051–7, Jun. 1998.
- [12] W. Chen, X. H. Zhu, T. Kato, P. Andersen, and K. Ugurbil, "Spatial and temporal differentiation of fMRI BOLD response in primary visual cortex of human brain during sustained visual simulation.," *Magn. Reson. Med.*, vol. 39, no. 4, pp. 520–7, Apr. 1998.
- [13] N. K. Logothetis, H. Guggenberger, S. Peled, and J. Pauls, "Functional imaging of the monkey brain," *Nat. Neurosci.*, vol. 2, no. 6, pp. 555–562, Jun. 1999.

- [14] A. Hougaard, B. H. Jensen, F. M. Amin, E. Rostrup, M. B. Hoffmann, and M. Ashina, "Cerebral Asymmetry of fMRI-BOLD Responses to Visual Stimulation," *PLoS One*, vol. 10, no. 5, p. e0126477, May 2015.
- [15] A. Bayram, E. Karahan, B. Bilgiç, A. Ademoglu, and T. Demiralp, "Achromatic temporal-frequency responses of human lateral geniculate nucleus and primary visual cortex," *Vision Res.*, vol. 127, pp. 177–185, Oct. 2016.
- [16] C. J. Bailey, B. G. Sanganahalli, P. Herman, H. Blumenfeld, A. Gjedde, and F. Hyder, "Analysis of Time and Space Invariance of BOLD Responses in the Rat Visual System," *Cereb. Cortex*, vol. 23, no. 1, pp. 210–222, Jan. 2013.
- [17] A. Niranjana, I. N. Christie, S. G. Solomon, J. A. Wells, and M. F. Lythgoe, "fMRI mapping of the visual system in the mouse brain with interleaved snapshot GE-EPI," *Neuroimage*, vol. 139, pp. 337–345, Oct. 2016.
- [18] C. Martin, "Contributions and complexities from the use of in vivo animal models to improve understanding of human neuroimaging signals," *Front. Neurosci.*, vol. 8, p. 211, Aug. 2014.
- [19] A. M. Packer, L. E. Russell, H. W. P. Dagleish, and M. Häusser, "Simultaneous all-optical manipulation and recording of neural circuit activity with cellular resolution in vivo," *Nat. Methods*, vol. 12, no. 2, pp. 140–146, Dec. 2014.
- [20] M. M. Petrinovic *et al.*, "A novel anesthesia regime enables neurofunctional studies and imaging genetics across mouse strains," *Sci. Rep.*, vol. 6, no. 1, p. 24523, Jul. 2016.
- [21] P. V Turner, T. Brabb, C. Pekow, and M. A. Vasbinder, "Administration of substances to laboratory animals: routes of administration and factors to consider.," *J. Am. Assoc. Lab. Anim. Sci.*, vol. 50, no. 5, pp. 600–13, Sep. 2011.
- [22] R. Klee *et al.*, "Etomidate anaesthesia for fMRI in mice revisited: Subcutaneous administration facilitates experimental procedures.," in *Proceedings of the 25th Annual Meeting of ISMRM*, 2017, p. 5316.
- [23] A. G. Webb, *Introduction to biomedical imaging*. Wiley-Interscience, 2003.
- [24] S. A. Huettel, A. W. Song, and G. McCarthy, *Functional magnetic resonance imaging*, 2nd ed. Sinauer Associates, 2008.
- [25] M. Demi, "Immagini di Risonanza Magnetica [Magnetic Resonance Imaging]," 2016. [Online]. Available: <http://slideplayer.it/slide/10911583/>. [Accessed: 24-Oct-2017].
- [26] P. C. Lauterbur, "Image Formation by Induced Local Interactions: Examples Employing Nuclear Magnetic Resonance," *Nature*, vol. 242, no. 5394, pp. 190–191, Mar. 1973.
- [27] L. Pauling and C. D. Coryell, "The Magnetic Properties and Structure of Hemoglobin, Oxyhemoglobin and Carbonmonoxyhemoglobin.," *Proc. Natl. Acad. Sci. U. S. A.*, vol. 22, no. 4,

pp. 210–6, Apr. 1936.

- [28] K. R. Thulborn, J. C. Waterton, P. M. Matthews, and G. K. Radda, “Oxygenation dependence of the transverse relaxation time of water protons in whole blood at high field.,” *Biochim. Biophys. Acta*, vol. 714, no. 2, pp. 265–70, Feb. 1982.
- [29] S. Ogawa and T. M. Lee, “Magnetic resonance imaging of blood vessels at high fields: in vivo and in vitro measurements and image simulation.,” *Magn. Reson. Med.*, vol. 16, no. 1, pp. 9–18, Oct. 1990.
- [30] K. Uğurbil, X. Hu, W. Chen, X. H. Zhu, S. G. Kim, and A. Georgopoulos, “Functional mapping in the human brain using high magnetic fields.,” *Philos. Trans. R. Soc. Lond. B. Biol. Sci.*, vol. 354, no. 1387, pp. 1195–213, Jul. 1999.
- [31] N. K. Logothetis, J. Pauls, M. Augath, T. Trinath, and A. Oeltermann, “Neurophysiological investigation of the basis of the fMRI signal,” *Nature*, vol. 412, no. 6843, pp. 150–157, Jul. 2001.
- [32] OpenStax, “Neurons and Glial Cells,” *OpenStax Biology*, 2012. [Online]. Available: https://cnx.org/contents/GFy_h8cu@9.87:c9j4p0aj@3/Neurons-and-Glial-Cells. [Accessed: 25-Oct-2017].
- [33] D. Attwell and S. B. Laughlin, “An Energy Budget for Signaling in the Grey Matter of the Brain,” *J. Cereb. Blood Flow Metab.*, vol. 21, no. 10, pp. 1133–1145, Oct. 2001.
- [34] X.-H. Zhu *et al.*, “Quantitative imaging of energy expenditure in human brain,” *Neuroimage*, vol. 60, no. 4, pp. 2107–2117, May 2012.
- [35] D. Shier, J. Butler, and R. Lewis, *Hole’s essentials of human anatomy & physiology*, 12th ed. McGraw-Hill Education, 2015.
- [36] L. Gagnon, A. F. Smith, D. A. Boas, A. Devor, T. W. Secomb, and S. Sakadžić, “Modeling of Cerebral Oxygen Transport Based on In vivo Microscopic Imaging of Microvascular Network Structure, Blood Flow, and Oxygenation,” *Front. Comput. Neurosci.*, vol. 10, p. 82, Aug. 2016.
- [37] N. K. Logothetis, “The underpinnings of the BOLD functional magnetic resonance imaging signal.,” *J. Neurosci.*, vol. 23, no. 10, pp. 3963–71, May 2003.
- [38] F. G. Ashby, *Statistical analysis of fMRI data*. MIT Press, 2011.
- [39] A. D. Elster, “BOLD and Brain Activity,” *MRIquestions.com*. [Online]. Available: <http://mriquestions.com/does-boldbrain-activity.html>. [Accessed: 25-Oct-2017].
- [40] R. B. Buxton, E. C. Wong, and L. R. Frank, “Dynamics of blood flow and oxygenation changes during brain activation: The balloon model,” *Magn. Reson. Med.*, vol. 39, no. 6, pp. 855–864, Jun. 1998.
- [41] H. Lu, X. Golay, J. J. Pekar, and P. C. M. van Zijl, “Sustained Poststimulus Elevation in

- Cerebral Oxygen Utilization after Vascular Recovery," *J. Cereb. Blood Flow Metab.*, vol. 24, no. 7, pp. 764–770, Jul. 2004.
- [42] A. M. Dale and R. L. Buckner, "Selective averaging of rapidly presented individual trials using fMRI," *Hum. Brain Mapp.*, vol. 5, no. 5, pp. 329–340, 1997.
- [43] P. Mansfield, "Multi-planar image formation using NMR spin echoes," *J. Phys. C Solid State Phys*, vol. 10, 1977.
- [44] J. M. Adamczak, T. D. Farr, J. U. Seehafer, D. Kalthoff, and M. Hoehn, "High field BOLD response to forepaw stimulation in the mouse," *Neuroimage*, vol. 51, no. 2, pp. 704–712, Jun. 2010.
- [45] N. K. Logothetis, "What we can do and what we cannot do with fMRI," *Nature*, vol. 453, no. 7197, pp. 869–878, Jun. 2008.
- [46] K. Uludağ, B. Müller-Bierl, and K. Uğurbil, "An integrative model for neuronal activity-induced signal changes for gradient and spin echo functional imaging," *Neuroimage*, vol. 48, no. 1, pp. 150–165, Oct. 2009.
- [47] K. J. Friston, P. Fletcher, O. Josephs, A. Holmes, M. D. Rugg, and R. Turner, "Event-Related fMRI: Characterizing Differential Responses," *Neuroimage*, vol. 7, no. 1, pp. 30–40, Jan. 1998.
- [48] R. Sladky, K. J. Friston, J. Tröstl, R. Cunnington, E. Moser, and C. Windischberger, "Slice-timing effects and their correction in functional MRI," *Neuroimage*, vol. 58, no. 2, pp. 588–594, Sep. 2011.
- [49] D. Parker, X. Liu, and Q. R. Razlighi, "Optimal slice timing correction and its interaction with fMRI parameters and artifacts," *Med. Image Anal.*, vol. 35, pp. 434–445, Jan. 2017.
- [50] T. Johnstone *et al.*, "Motion correction and the use of motion covariates in multiple-subject fMRI analysis," *Hum. Brain Mapp.*, vol. 27, no. 10, pp. 779–788, Oct. 2006.
- [51] G. M. Boynton, S. A. Engel, G. H. Glover, and D. J. Heeger, "Linear systems analysis of functional magnetic resonance imaging in human V1.," *J. Neurosci.*, vol. 16, no. 13, pp. 4207–21, Jul. 1996.
- [52] G. H. Glover, "Deconvolution of impulse response in event-related BOLD fMRI.," *Neuroimage*, vol. 9, no. 4, pp. 416–29, Apr. 1999.
- [53] R. L. Buckner, W. Koutstaal, D. L. Schacter, A. D. Wagner, and B. R. Rosen, "Functional–Anatomic Study of Episodic Retrieval Using fMRI," *Neuroimage*, vol. 7, no. 3, pp. 151–162, Apr. 1998.
- [54] G. K. Aguirre, E. Zarahn, and M. D'Esposito, "The Variability of Human, BOLD Hemodynamic Responses," *Neuroimage*, vol. 8, no. 4, pp. 360–369, Nov. 1998.
- [55] M. T. Colonnese, M. A. Phillips, M. Constantine-Paton, K. Kaila, and A. Jasanoff, "Development

- of hemodynamic responses and functional connectivity in rat somatosensory cortex,” *Nat. Neurosci.*, vol. 11, no. 1, pp. 72–79, Jan. 2008.
- [56] F. Schlegel, A. Schroeter, and M. Rudin, “The hemodynamic response to somatosensory stimulation in mice depends on the anesthetic used: Implications on analysis of mouse fMRI data,” *Neuroimage*, vol. 116, pp. 40–49, Aug. 2015.
- [57] G. Qing, S. Zhang, B. Wang, and N. Wang, “Functional MRI Signal Changes in Primary Visual Cortex Corresponding to the Central Normal Visual Field of Patients with Primary Open-Angle Glaucoma,” *Investig. Ophthalmology Vis. Sci.*, vol. 51, no. 9, p. 4627, Sep. 2010.
- [58] W. Platzer and W. (Werner). Kahle, *Color Atlas of Human Anatomy, Vol. 3: Nervous System and Sensory Organs*, 5th ed. Thieme, 2003.
- [59] L. Erskine and E. Herrera, “Connecting the retina to the brain.,” *ASN Neuro*, vol. 6, no. 6, 2014.
- [60] G. J. Tortora and B. Derrickson, *Introduction to the Human Body: The Essentials of Anatomy and Physiology*, 9th ed. John Wiley & Sons, 2012.
- [61] S. Veleri, C. H. Lazar, B. Chang, P. A. Sieving, E. Banin, and A. Swaroop, “Biology and therapy of inherited retinal degenerative disease: insights from mouse models,” *Dis. Model. Mech.*, vol. 8, no. 2, pp. 109–129, Feb. 2015.
- [62] C. J. Jeon, E. Strettoi, and R. H. Masland, “The major cell populations of the mouse retina.,” *J. Neurosci.*, vol. 18, no. 21, pp. 8936–46, Nov. 1998.
- [63] J. B. Calderone and G. H. Jacobs, “Regional variations in the relative sensitivity to UV light in the mouse retina.,” *Vis. Neurosci.*, vol. 12, no. 3, pp. 463–8, 1995.
- [64] G. H. Jacobs, G. A. Williams, and J. A. Fenwick, “Influence of cone pigment coexpression on spectral sensitivity and color vision in the mouse,” *Vision Res.*, vol. 44, no. 14, pp. 1615–1622, Jun. 2004.
- [65] Y. V. Wang, M. Weick, and J. B. Demb, “Spectral and Temporal Sensitivity of Cone-Mediated Responses in Mouse Retinal Ganglion Cells,” *J. Neurosci.*, vol. 31, no. 21, pp. 7670–7681, May 2011.
- [66] J. Neitz and G. H. Jacobs, “Reexamination of spectral mechanisms in the rat (*Rattus norvegicus*).,” *J. Comp. Psychol.*, vol. 100, no. 1, pp. 21–9, Mar. 1986.
- [67] C. Ling, G. E. Schneider, and S. Jhaveri, “Target-specific morphology of retinal axon arbors in the adult hamster.,” *Vis. Neurosci.*, vol. 15, no. 3, pp. 559–79, 1998.
- [68] B. Völgyi, S. Chheda, and S. A. Bloomfield, “Tracer coupling patterns of the ganglion cell subtypes in the mouse retina,” *J. Comp. Neurol.*, vol. 512, no. 5, pp. 664–687, Feb. 2009.
- [69] J. N. Kay *et al.*, “Retinal Ganglion Cells with Distinct Directional Preferences Differ in Molecular Identity, Structure, and Central Projections,” *J. Neurosci.*, vol. 31, no. 21, pp. 7753–7762, May

2011.

- [70] J. Coombs, D. van der List, G.-Y. Wang, and L. M. Chalupa, "Morphological properties of mouse retinal ganglion cells," *Neuroscience*, vol. 140, no. 1, pp. 123–136, Jan. 2006.
- [71] T. Mueller, "What is the Thalamus in Zebrafish?," *Front. Neurosci.*, vol. 6, p. 64, 2012.
- [72] J. A. Gordon and M. P. Stryker, "Experience-dependent plasticity of binocular responses in the primary visual cortex of the mouse.," *J. Neurosci.*, vol. 16, no. 10, pp. 3274–86, May 1996.
- [73] C. P. Heesy, "On the relationship between orbit orientation and binocular visual field overlap in mammals," *Anat. Rec.*, vol. 281A, no. 1, pp. 1104–1110, Nov. 2004.
- [74] J. G. McHaffie and B. E. Stein, "Eye movements evoked by electrical stimulation in the superior colliculus of rats and hamsters.," *Brain Res.*, vol. 247, no. 2, pp. 243–53, Sep. 1982.
- [75] R. H. Wurtz and E. R. Kandel, "Central Visual Pathways," in *Principles of neural science*, 3rd ed., E. R. Kandel, J. H. Schwartz, and T. M. Jessell, Eds. New York: Elsevier, 1991, pp. 420 – 439.
- [76] S. M. King, "Escape-related behaviours in an unstable, elevated and exposed environment. II. Long-term sensitization after repetitive electrical stimulation of the rodent midbrain defence system.," *Behav. Brain Res.*, vol. 98, no. 1, pp. 127–42, Jan. 1999.
- [77] N. J. Gandhi and H. A. Katnani, "Motor Functions of the Superior Colliculus," *Annu. Rev. Neurosci.*, vol. 34, no. 1, pp. 205–231, Jul. 2011.
- [78] B. G. Cooper, D. Y. Miya, and S. J. Mizumori, "Superior colliculus and active navigation: role of visual and non-visual cues in controlling cellular representations of space.," *Hippocampus*, vol. 8, no. 4, pp. 340–72, 1998.
- [79] T. R. Vidyasagar, "Possible plasticity in the rat superior colliculus.," *Nature*, vol. 275, no. 5676, pp. 140–1, Sep. 1978.
- [80] J. D. Radel, L. Galli-Resta, and R. D. Lund, "Plasticity in innervation of the rat superior colliculus by transplanted retinae as a result of eye removal at maturity.," *Exp. Neurol.*, vol. 112, no. 3, pp. 252–63, Jun. 1991.
- [81] S. Schuett, T. Bonhoeffer, and M. Hübener, "Mapping retinotopic structure in mouse visual cortex with optical imaging.," *J. Neurosci.*, vol. 22, no. 15, pp. 6549–59, Aug. 2002.
- [82] A. Antonini, M. Fagiolini, and M. P. Stryker, "Anatomical correlates of functional plasticity in mouse visual cortex.," *J. Neurosci.*, vol. 19, no. 11, pp. 4388–406, Jun. 1999.
- [83] K. Ohki, S. Chung, Y. H. Ch'ng, P. Kara, and R. C. Reid, "Functional imaging with cellular resolution reveals precise micro-architecture in visual cortex," *Nature*, vol. 433, no. 7026, pp. 597–603, Feb. 2005.

- [84] U. C. Dräger, "Receptive fields of single cells and topography in mouse visual cortex," *J. Comp. Neurol.*, vol. 160, no. 3, pp. 269–289, Apr. 1975.
- [85] U. C. Dräger and D. H. Hubel, "Responses to visual stimulation and relationship between visual, auditory, and somatosensory inputs in mouse superior colliculus.," *J. Neurophysiol.*, vol. 38, no. 3, pp. 690–713, May 1975.
- [86] C. Métin, P. Godement, and M. Imbert, "The primary visual cortex in the mouse: receptive field properties and functional organization.," *Exp. brain Res.*, vol. 69, no. 3, pp. 594–612, 1988.
- [87] L. L. Glickfeld, M. L. Andermann, V. Bonin, and R. C. Reid, "Cortico-cortical projections in mouse visual cortex are functionally target specific," *Nat. Neurosci.*, vol. 16, no. 2, pp. 219–226, Jan. 2013.
- [88] M. E. Garrett, I. Nauhaus, J. H. Marshel, and E. M. Callaway, "Topography and Areal Organization of Mouse Visual Cortex," *J. Neurosci.*, vol. 34, no. 37, pp. 12587–12600, Sep. 2014.
- [89] X. Zhao, M. Liu, and J. Cang, "Visual Cortex Modulates the Magnitude but Not the Selectivity of Looming-Evoked Responses in the Superior Colliculus of Awake Mice," *Neuron*, vol. 84, no. 1, pp. 202–213, Oct. 2014.
- [90] E. H. Feinberg and M. Meister, "Orientation columns in the mouse superior colliculus," *Nature*, vol. 519, no. 7542, pp. 229–232, Dec. 2014.
- [91] S. Inayat, J. Barchini, H. Chen, L. Feng, X. Liu, and J. Cang, "Neurons in the Most Superficial Lamina of the Mouse Superior Colliculus Are Highly Selective for Stimulus Direction," *J. Neurosci.*, vol. 35, no. 20, pp. 7992–8003, May 2015.
- [92] K. Sicard *et al.*, "Regional Cerebral Blood Flow and BOLD Responses in Conscious and Anesthetized Rats under Basal and Hypercapnic Conditions: Implications for Functional MRI Studies," *J. Cereb. Blood Flow Metab.*, vol. 23, no. 4, pp. 472–481, Apr. 2003.
- [93] C. Martin, J. Martindale, J. Berwick, and J. Mayhew, "Investigating neural–hemodynamic coupling and the hemodynamic response function in the awake rat," *Neuroimage*, vol. 32, no. 1, pp. 33–48, Aug. 2006.
- [94] D. F. Kohn, S. K. Wixson, W. J. White, and G. J. Benson, *Anesthesia and Analgesia in Laboratory Animals*, 1st ed. Academic Press, 1997.
- [95] A. C. Huk, D. Ress, and D. J. Heeger, "Neuronal basis of the motion aftereffect reconsidered.," *Neuron*, vol. 32, no. 1, pp. 161–72, Oct. 2001.
- [96] P. A. Flecknell, "Anaesthesia of animals for biomedical research.," *Br. J. Anaesth.*, vol. 71, no. 6, pp. 885–94, Dec. 1993.
- [97] L. Ferrari *et al.*, "A robust experimental protocol for pharmacological fMRI in rats and mice," *J.*

Neurosci. Methods, vol. 204, no. 1, pp. 9–18, Feb. 2012.

- [98] Y. Sato, N. Seo, and E. Kobayashi, “Genetic background differences between FVB and C57BL/6 mice affect hypnotic susceptibility to pentobarbital, ketamine and nitrous oxide, but not isoflurane,” *Acta Anaesthesiol. Scand.*, vol. 50, no. 5, pp. 553–556, May 2006.
- [99] T. Fleischmann, P. Jirkof, J. Henke, M. Arras, and N. Cesarovic, “Injection anaesthesia with fentanyl–midazolam–medetomidine in adult female mice: importance of antagonization and perioperative care,” *Lab. Anim.*, vol. 50, no. 4, pp. 264–274, Aug. 2016.
- [100] J. L. Tremoleda, A. Kerton, and W. Gsell, “Anaesthesia and physiological monitoring during in vivo imaging of laboratory rodents: considerations on experimental outcomes and animal welfare,” *EJNMMI Res.*, vol. 2, no. 1, p. 44, Aug. 2012.
- [101] T. Kim, K. Masamoto, M. Fukuda, A. Vazquez, and S.-G. Kim, “Frequency-dependent neural activity, CBF, and BOLD fMRI to somatosensory stimuli in isoflurane-anesthetized rats,” *Neuroimage*, vol. 52, no. 1, pp. 224–233, Aug. 2010.
- [102] M. Larsen and I. A. Langmoen, “The effect of volatile anaesthetics on synaptic release and uptake of glutamate,” *Toxicol. Lett.*, vol. 100–101, pp. 59–64, Nov. 1998.
- [103] K. Masamoto, M. Fukuda, A. Vazquez, and S.-G. Kim, “Dose-dependent effect of isoflurane on neurovascular coupling in rat cerebral cortex,” *Eur. J. Neurosci.*, vol. 30, no. 2, pp. 242–250, Jul. 2009.
- [104] M. D. Sinclair, “A review of the physiological effects of alpha2-agonists related to the clinical use of medetomidine in small animal practice,” *Can. Vet. J. = La Rev. Vet. Can.*, vol. 44, no. 11, pp. 885–97, Nov. 2003.
- [105] M. Fukuda, A. L. Vazquez, X. Zong, and S.-G. Kim, “Effects of the α_2 -adrenergic receptor agonist dexmedetomidine on neural, vascular and BOLD fMRI responses in the somatosensory cortex,” *Eur. J. Neurosci.*, vol. 37, no. 1, pp. 80–95, Jan. 2013.
- [106] R. Weber, P. Ramos-Cabrer, D. Wiedermann, N. van Camp, and M. Hoehn, “A fully noninvasive and robust experimental protocol for longitudinal fMRI studies in the rat,” *Neuroimage*, vol. 29, no. 4, pp. 1303–1310, Feb. 2006.
- [107] R. Weber *et al.*, “Early Prediction of Functional Recovery after Experimental Stroke: Functional Magnetic Resonance Imaging, Electrophysiology, and Behavioral Testing in Rats,” *J. Neurosci.*, vol. 28, no. 5, pp. 1022–1029, Jan. 2008.
- [108] F. Zhao, T. Zhao, L. Zhou, Q. Wu, and X. Hu, “BOLD study of stimulation-induced neural activity and resting-state connectivity in medetomidine-sedated rat,” *Neuroimage*, vol. 39, no. 1, pp. 248–260, Jan. 2008.
- [109] W. Huang, I. Plyka, H. Li, E. M. Eisenstein, N. D. Volkow, and C. S. Springer, “Magnetic resonance imaging (MRI) detection of the murine brain response to light: temporal

- differentiation and negative functional MRI changes.,” *Proc. Natl. Acad. Sci. U. S. A.*, vol. 93, no. 12, pp. 6037–42, Jun. 1996.
- [110] K. C. Chan, K. Kai Xing, M. M. Cheung, I. Y. Zhou, and E. X. Wu, “Functional MRI of postnatal visual development in normal rat superior colliculi,” in *31st Annual International Conference of the IEEE Engineering in Medicine and Biology Society*, 2009, pp. 4436–4439.
- [111] K. C. Chan, K. K. Xing, M. M. Cheung, I. Y. Zhou, and E. X. Wu, “Functional MRI of postnatal visual development in normal and hypoxic–ischemic-injured superior colliculi,” *Neuroimage*, vol. 49, no. 3, pp. 2013–2020, Feb. 2010.
- [112] J. W. Zhang *et al.*, “BOLD Response Dependence on the Stimulation Light Intensity in the Rat Superior Colliculus,” in *Proceedings of the 19th Annual Meeting of ISMRM*, 2011, p. 3677.
- [113] C. Lau, I. Y. Zhou, M. M. Cheung, K. C. Chan, and E. X. Wu, “BOLD Temporal Dynamics of Rat Superior Colliculus and Lateral Geniculate Nucleus following Short Duration Visual Stimulation,” *PLoS One*, vol. 6, no. 4, p. e18914, Apr. 2011.
- [114] C. Lau *et al.*, “BOLD responses in the superior colliculus and lateral geniculate nucleus of the rat viewing an apparent motion stimulus,” *Neuroimage*, vol. 58, no. 3, pp. 878–884, Oct. 2011.
- [115] N. Van Camp, M. Verhoye, C. I. De Zeeuw, and A. Van der Linden, “Light Stimulus Frequency Dependence of Activity in the Rat Visual System as Studied With High-Resolution BOLD fMRI,” *J. Neurophysiol.*, vol. 95, no. 5, pp. 3164–3170, Jan. 2006.
- [116] C. P. Pawela *et al.*, “Modeling of region-specific fMRI BOLD neurovascular response functions in rat brain reveals residual differences that correlate with the differences in regional evoked potentials,” *Neuroimage*, vol. 41, no. 2, pp. 525–534, Jun. 2008.
- [117] C. Gelegen *et al.*, “Staying awake - a genetic region that hinders α_2 adrenergic receptor agonist-induced sleep,” *Eur. J. Neurosci.*, vol. 40, no. 1, pp. 2311–2319, Jul. 2014.
- [118] G.-D. Li, D. C. Chiara, J. B. Cohen, and R. W. Olsen, “Neurosteroids allosterically modulate binding of the anesthetic etomidate to gamma-aminobutyric acid type A receptors.,” *J. Biol. Chem.*, vol. 284, no. 18, pp. 11771–5, May 2009.
- [119] C. Leithner *et al.*, “A flow sensitive alternating inversion recovery (FAIR)-MRI protocol to measure hemispheric cerebral blood flow in a mouse stroke model,” *Exp. Neurol.*, vol. 210, no. 1, pp. 118–127, Mar. 2008.
- [120] A. G. Hudetz, F. Luo, Prieto T, Wood, and Li, “Visual System Activation in the Rat as Studied with BOLD fMRI,” in *Proceedings of the 11th Annual Meeting of ISMRM*, 2003, p. 1851.
- [121] C. Lau, K. Xing, K. C. Chan, and E. X. Wu, “BOLD Temporal Dynamics of Superior Colliculus and Lateral Geniculate Nucleus during Monocular Visual Stimulation,” in *Proceedings of the 18th Annual Meeting of ISMRM*, 2010.

- [122] B. H. De La Garza, E. R. Muir, G. Li, Y.-Y. I. Shih, and T. Q. Duong, "Blood oxygenation level-dependent (BOLD) functional MRI of visual stimulation in the rat retina at 11.7 T.," *NMR Biomed.*, vol. 24, no. 2, pp. 188–93, Feb. 2011.
- [123] Y.-Y. I. Shih *et al.*, "Lamina-specific functional MRI of retinal and choroidal responses to visual stimuli.," *Invest. Ophthalmol. Vis. Sci.*, vol. 52, no. 8, pp. 5303–10, Jul. 2011.
- [124] B. Rogers, Y.-Y. I. Shih, B. D. La Garza, J. M. Harrison, J. Roby, and T. Q. Duong, "A low cost color visual stimulator for fMRI," *J. Neurosci. Methods*, vol. 204, no. 2, pp. 379–382, Mar. 2012.
- [125] A. Niranjana, B. Siow, M. Lythgoe, and J. Wells, "High temporal resolution BOLD responses to visual stimuli measured in the mouse superior colliculus," *Matters*, vol. 3, no. 2, Feb. 2017.
- [126] Doric, "Catalog: Photonics Hardware Products for Optogenetics," *Doric Lenses*, 2011. [Online]. Available: [http://neurodatasharing.bme.gatech.edu/cloud/Newman et al/Figure 1/Supplement 1/2011_Light-Stimulation-Devices/parts/led/Product_catalog_RELEASE_v5.4-web_110228_doric197_test_Sh4r7.pdf](http://neurodatasharing.bme.gatech.edu/cloud/Newman_et_al/Figure_1/Supplement_1/2011_Light-Stimulation-Devices/parts/led/Product_catalog_RELEASE_v5.4-web_110228_doric197_test_Sh4r7.pdf). [Accessed: 30-Oct-2017].
- [127] Thorlabs, "T-Cube LED Driver LEDD1B Operation Manual," *Thorlabs*, 2016. [Online]. Available: <https://www.thorlabs.com/drawings/ae27a0a7068e9d5a-63FF8419-93F0-3535-285665D0DA0328D7/LEDD1B-Manual.pdf>. [Accessed: 13-Oct-2017].
- [128] C. A. Schneider, W. S. Rasband, and K. W. Eliceiri, "NIH Image to ImageJ: 25 years of image analysis," *Nat. Methods*, vol. 9, no. 7, pp. 671–675, Jun. 2012.
- [129] E. S. Lein *et al.*, "Genome-wide atlas of gene expression in the adult mouse brain," *Nature*, vol. 445, no. 7124, pp. 168–176, Jan. 2007.
- [130] K. B. J. Franklin and G. Paxinos, *Paxinos and Franklin's the Mouse Brain in Stereotaxic Coordinates*, 4th ed. Elsevier, 2013.
- [131] B. S. Oommen and J. S. Stahl, "Eye orientation during static tilts and its relationship to spontaneous head pitch in the laboratory mouse," *Brain Res.*, vol. 1193, pp. 57–66, Feb. 2008.
- [132] B. van Alphen, B. H. J. Winkelman, and M. A. Frens, "Age- and Sex-Related Differences in Contrast Sensitivity in C57Bl/6 Mice," *Invest. Ophthalmol. Vis. Sci.*, vol. 50, no. 5, pp. 2451–2458, May 2009.
- [133] F. Hyder, D. L. Rothman, and R. G. Shulman, "Total neuroenergetics support localized brain activity: Implications for the interpretation of fMRI," *Proc. Natl. Acad. Sci.*, vol. 99, no. 16, pp. 10771–10776, Aug. 2002.
- [134] A. Schroeter, F. Schlegel, A. Seuwen, J. Grandjean, and M. Rudin, "Specificity of stimulus-evoked fMRI responses in the mouse: The influence of systemic physiological changes associated with innocuous stimulation under four different anesthetics," *Neuroimage*, vol. 94, pp. 372–384, Jul. 2014.

- [135] J. Grandjean, A. Schroeter, I. Batata, and M. Rudin, "Optimization of anesthesia protocol for resting-state fMRI in mice based on differential effects of anesthetics on functional connectivity patterns," *Neuroimage*, vol. 102, pp. 838–847, Nov. 2014.
- [136] M. B. Wall, R. Walker, and A. T. Smith, "Functional imaging of the human superior colliculus: An optimised approach," *Neuroimage*, vol. 47, no. 4, pp. 1620–1627, Oct. 2009.
- [137] M. A. Pisauro, N. T. Dhruv, M. Carandini, and A. Benucci, "Fast hemodynamic responses in the visual cortex of the awake mouse.," *J. Neurosci.*, vol. 33, no. 46, pp. 18343–51, Nov. 2013.
- [138] A. Eklund, M. Andersson, C. Josephson, M. Johannesson, and H. Knutsson, "Does parametric fMRI analysis with SPM yield valid results?—An empirical study of 1484 rest datasets," *Neuroimage*, vol. 61, no. 3, pp. 565–578, Jul. 2012.
- [139] M. van Wyk, H. Wässle, and W. R. Taylor, "Receptive field properties of ON- and OFF-ganglion cells in the mouse retina.," *Vis. Neurosci.*, vol. 26, no. 3, pp. 297–308, 2009.
- [140] G. Malerba *et al.*, "Risk factors of relative adrenocortical deficiency in intensive care patients needing mechanical ventilation," *Intensive Care Med.*, vol. 31, no. 3, pp. 388–392, Mar. 2005.
- [141] A. Absalom, D. Pledger, and A. Kong, "Adrenocortical function in critically ill patients 24 h after a single dose of etomidate.," *Anaesthesia*, vol. 54, no. 9, pp. 861–7, Sep. 1999.
- [142] F. de Jong, C. Mallios, C. Jansen, P. Scheck, and S. Lamberts, "Etomidate suppresses adrenocortical function by inhibition of 11 beta-hydroxylation.," *J. Clin. Endocrinol. Metab.*, vol. 59, no. 6, pp. 1143–1147, Dec. 1984.
- [143] M. P. Boidin, W. E. Erdmann, and N. S. Faithfull, "The role of ascorbic acid in etomidate toxicity.," *Eur. J. Anaesthesiol.*, vol. 3, no. 5, pp. 417–22, Sep. 1986.
- [144] D. Das, C. Sen, and A. Goswami, "Effect of Vitamin C on adrenal suppression by etomidate induction in patients undergoing cardiac surgery: A randomized controlled trial," *Ann. Card. Anaesth.*, vol. 19, no. 3, p. 410, 2016.
- [145] Y. Sun, S. Feng, L. Li, and K. Huang, "Effects of ascorbic acid on etomidate-induced inhibition of adrenocortical function in rabbits," *Int J Clin Exp Med*, vol. 10, no. 8, pp. 12553–12558, 2017.
- [146] J. S. Jenkins, "The effect of ascorbic acid on adrenal steroid synthesis in vitro.," *Endocrinology*, vol. 70, no. 2, pp. 267–271, Feb. 1962.
- [147] A. Weyers, L. I. Ugnia, H. G. Ovando, and N. B. Gorla, "Antioxidant capacity of vitamin C in mouse liver and kidney tissues.," *Biocell*, vol. 32, no. 1, pp. 27–31, Apr. 2008.
- [148] B. Scholl, J. Burge, and N. J. Priebe, "Binocular integration and disparity selectivity in mouse primary visual cortex," *J. Neurophysiol.*, vol. 109, no. 12, pp. 3013–3024, Jun. 2013.

Annex A

Table A.1 – Parameters of the 9 double-gamma functions that were tested and the time instants in which they and their convolution with the paradigm peaked.

Hemodynamic response function	Parameters					Peak (s)	Peak after convolution with the paradigm (s)
	a	n_1	λ_1	n_2	λ_2		
1	0.160	2	0.90	13	0.600	0.90	5.29
2	0.187	2	1.15	13	0.615	1.15	5.90
3	0.214	2	1.40	13	0.648	1.40	6.51
4	0.239	2	1.65	13	0.690	1.65	7.12
5	0.261	2	1.90	13	0.737	1.90	7.73
6	0.280	2	2.15	13	0.788	2.15	8.34
7	0.297	2	2.40	13	0.840	2.40	8.95
8	0.311	2	2.65	13	0.894	2.65	9.56
9	0.324	2	2.90	13	0.950	2.90	10.17

Annex B

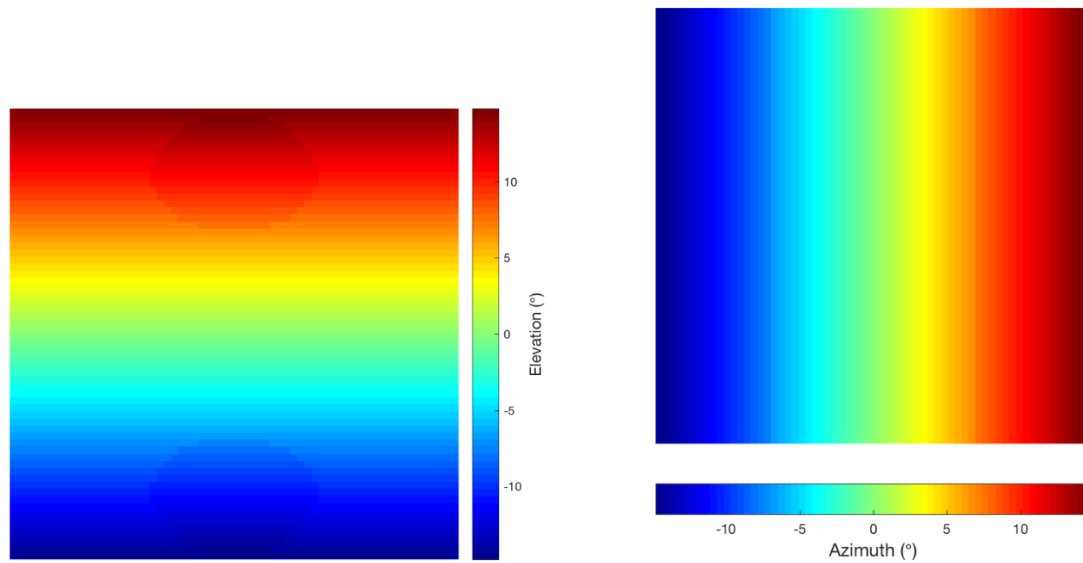


Figure B.1 – Spherical coordinates of the FOV of the flat screen. (*Left*) Elevation coordinates of the FOV of the screen that was used, with colours representing isoaltitude lines. (*Right*) Azimuth coordinates of the FOV of the screen that was used, with colours representing isoazimuth lines. The 0° elevation and 0° azimuth point of the FOV corresponds to the origin of the line perpendicular to the screen that intersected the centre of the mouse's eye.